UNIVERSITY OF
BIRMINGHAM

STRUCTURE CHARACTERISATION OF CATALYSTS USING X-RAY MICRO-COMPUTED TOMOGRAPHY

By

MARIE LUNEL

A thesis submitted to
The University of Birmingham
for the degree of
DOCTOR OF PHILOSOPHY

School of Chemical Engineering
The University of Birmingham
September 2013

ABSTRACT

Knowledge of internal porous structure is essential in improving the development of a catalytic system and consequently leading to an optimized performance. X-ray micro-Computed Tomography (XRCT) is a non-invasive and non-destructive technique that can be used to obtain 3-D images of scanned samples and to visualise the internal structure of the material. The XRCT technique could be utilised to perform routine check-ups.

XRCT has been used to study density variation and to characterise the internal structure of various types of catalysts support. It has been demonstrated that the method can be used to show differences in density and pore distribution and that differences can be related to the process route by which the specimen was prepared.

Alumina samples with defects prepared using different conditions have been investigated in order to acquire information on the introduction and development of cracks. Results indicated that cracks became larger when the water content, the ram speed of the extruder and the drying temperature were higher. The width of the cracks ranges between 20-150 μm and the lengths varied from a few micrometres to millimetres in length. The calcination process increased the number and the 3-D size of the cracks.

Both concentration of the bulk solution and impregnation time appeared to have a significant impact on the metal distribution profile during the impregnation process. Egg-shell profile was visualised and the thickness was proportional to the concentration of impregnation solution. Drying had a strong impact on the metal profile, as a redistribution of copper was noticed. The redistribution was observed exclusively in the case of weak adsorption of copper with alumina support.

Experiments on the newly established I13 beamline synchrotron in Diamond was carried out in order to gain an understanding of the cracks induction/propagation and of the diffusion of metallic solution inside the catalyst support. Although the radiographic experiments showed the shrinkage of the paste during drying, the visualisation of internal structure was not achievable due to an issue of the reconstruction program.

Specially dedicated to my grand-parents,

Marie et Frantz

Acknowledgments

I would like to thank my academic supervisors Prof. Serafim Bakalis and Dr.Taghi Miri, as well as my industrial supervisors from Johnson Matthey Liz Holt, Dr Dan Cairns, Dr Phil Hughes and Dr Gareth Hatton for their guidance, understanding and support on this project. Thanks for placing your trust in me and giving me the opportunity to grow intellectually. The financial support from EPSRC and Johnson Matthey is also acknowledged.

For the Dental school, I would like to thank Dr Paul Cooper and Michele Holder for giving us the possibility to use the X-Ray Computed Tomography. Particular thanks to Nick Corps for his kind help and guidance through this work.

My thanks also go to all my friends from the University for their supports. I am also particularly grateful to Ourania Gouseti, Angel Fernandez, Isaac Viczaino, Rafael Orozco, Emilia Nowak, Suwijak Hansriwijit, Luke Dandy, Emmanuelle Costard, Alvaro Gil, Marcin Khzouz for their unconditional support and friendship.

Ιδιαίτερες ευχαριστίες στην πολύτιμη και καλύτερη φίλη μου, Flora Challou, που ήταν πάντα εκεί για μένα. Σ'ευχαριστώ για τη βοήθεια, την υποστήριξh, την ευγένεια και το χαμόγελο που πάντα απλοχερα μου πρόσφερες. Σ'ευχαριστώ που υπάρξεις στη ζωή μου.

A mes deux meilleurs amis d'enfance, Emilie et Benoit, je vous remercie de votre soutien durant cette période, ainsi que d'être là en toutes circonstances. Vous êtes dans mon cœur.

Finally, I would like to thank my beloved family, my beloved grand-mother Marie Bureau, my parents Michel and Patricia, my sister Anne and my aunt Marie-France, for their never-ending support, encouragement and strength, without which I would not be here.

TABLE OF CONTENTS

ABREVIATION

CT	Computed Tomography
CS	Cross sectional
EM	Electron Microscopy
GV	Grey Value
HRTEM	High Resolution Transmission Electron Microscopy
ROI	Region of Interest
SDV	Standard Deviation
SEM	Scanning Electron Microscopy
SMI	Structure Model Index
STEM	Scanning Transmission Electron Microscopy
TEM	Transmission Electron Microscopy
VOI	Volume of Interest
XRCT	X- Ray Computed-Tomography
3-D	Three Dimensional

NOMENCLATURE

A	Effective atomic weight
c	Concentration (mol/m^3)
D	Diffusion coefficient or diffusivity in (m^2/s)
I	Intensity of transmitted radiation (mA)
I_0	Intensity of incident radiation (mA)
J	Diffusion flux of material per unit area (mol/m^{2}s)
N_{AV}	Avogadro's number
P	Pressure (Pa)
R	Gas constant
r_p	Pore radius (m)
S	Surface area (m^2)
T	Absolute temperature (K)
V_L	Molar volume of the liquid
V_p	Pore volume (m^3)
X	Thickness (m)
Z	Effective atomic number

Greek letters

γ	Surface tension
θ	Contact angle
μ	Attenuation coefficient
ρ	Material density (kg/m^3)

LIST OF FIGURES

CHAPTER 2: LITERATURE REVIEW

CHAPTER 3: MATERIALS AND METHODS

CHAPTER 4: EFFECT OF PROCESSING ROUTE AND FORMULATION ON DENSITY DISTRIBUTION

CHAPTER 5: EFFECT OF THE PROCESSING CONDITIONS ON THE DEVELOPMENT OF CRACKS.

CHAPTER 6: DISTRIBUTION OF COPPER NITRATE TRIHYDRATE SOLUTION IN THE CATALYST SUPPORT.

CHAPTER 7: INVESTIGATION OF THE MICROSTRUCTURE OF CATALYST SUPPORT USING SYNCHROTRON.

LIST OF TABLES

CHAPTER 2: LITERATURE REVIEW

CHAPTER 3: MATERIALS AND METHODS

CHAPTER 4: EFFECT OF PROCESSING ROUTE AND FORMULATION ON DENSITY DISTRIBUTION

CHAPTER 5: EFFECT OF THE PROCESSING CONDITIONS ON THE DEVELOPMENT OF CRACKS.

CHAPTER 7: INVESTIGATION OF THE MICROSTRUCTURE OF CATALYST SUPPORT USING SYNCHROTRON.

CHAPTER 1 – INTRODUCTION

1.1 Catalyst overview

Catalysts are commonly used not only in the chemical process industries but also in everyday life. For instance, they are used in cars for emission control in the exhaust system. In industry, heterogeneous catalysts are used in several reactions, such as hydrogenations, catalytic cracking, or reforming. They could be also employed in the synthesis of ammonia and for the oxidation of ethylene (Heinemann, 1997).

A catalyst is a substance that increases the rate at which a chemical reaction approaches equilibrium without becoming permanently involved in the reaction (Richardson, 1989; Campanati et al., 2003). The ideal catalyst would combine properties such as activity, selectivity, lifetime and ease of regeneration (Acres, 1980; Campanati et al., 2003). Heterogeneous catalysts often consist of porous material, which support the active components. Porosity is very important in determining physical properties such as durability, mechanical strength, adsorption properties and mass transfer. Moreover, in reaction processes, benefits could be obtained by understanding the density and porosity distributions. As chemical reactions take place in the internal porous network, the knowledge of the overall

porosity, pore size distribution and surface area, are crucial in order to maximise the catalyst's performance.

It is very important that a catalyst support has a suitable pore network that provides a high surface area for the catalytic reactions to occur, and at the same time is capable of withstanding extreme conditions within the reactor (e.g. high temperature and pressure conditions). Thus, the understanding of pore structure is crucial and the characterisation of the spatial pore size distribution of porous media is a key area of interest in many industrial processes, including catalytic reaction engineering, oil recovery and absorbance of contaminants (Rigby et al., 2001; Rigby et al., 2004a).

Catalyst supports are selected according to certain characteristics, such as desirable mechanical properties (attrition resistance and strength), stability, high surface area and porosity (Satterfield, 1970). These characteristics depend on the preparation of the catalyst supports, which is divided into several steps ranging from formulation to finishing. Control of physical and chemical parameters is necessary, as the internal structure of the catalyst support changes after each stage of the processing route. Catalyst preparation has a strong impact on density distribution and porosity. The knowledge of internal porous structure is essential in improving the development of catalyst and consequently leading to the best performance possible. Characterisation techniques are widely used for studying catalyst structures.

1.2 Structure characterisation

In the past fifty years, several techniques have been developed to characterise the catalyst structure, attributed to the emergence of modern technologies, advanced computational power and the ability to collect physical property data on the nanometre scale (Leofanti et al., 1997).

Characterisation of catalyst structures at different length scales is crucial to understand its physical properties and finally, to improve its performance. Porous structures are characterised by different parameters, such as void fraction also called porosity, pore size distribution, specific surface area, pore network and connectivity (Rigby and Daut, 2002). The techniques used to characterise catalyst structure, range from the traditional nitrogen gas adsorption method and mercury porosimetry to the imaging techniques (Scanning Electron Microscopy, Transmission Electron Microscopy, X-Ray micro-Computed Tomography, and Synchrotron to name a few). Nitrogen gas absorption and mercury porosimetry provide information on pores' volume and size distribution at nano-scale (Rigby et al., 2003a). However, they do not provide any information on the spatial distribution and interconnectivity of pores.

In catalyst research, Scanning Electron Microscopy (SEM) is used to characterise external structures at nanoscale (Datye, 2003), while the Transmission Electron Tomography (TEM) is widely used to characterise internal structure. Despite the fact that the above imaging methods exhibit many advantages, such as the visualisation of the structure at a smaller scale, they cannot provide a full 3-D distribution of pores. Only tomography techniques would yield information about the 3-D distribution of the element of interest within the sample. Tomography techniques were used in an attempt to quantify the pore structure and the pore network of heterogeneous catalyst with lengths ranging from hundreds of micrometres to

nanometres (e.g. the dual focused ion beam tomography DB-FIB = 10 nm – 1 μm) (Tariq et al., 2011a; Tariq et al., 2011b). However, some of the techniques require a sample preparation before analysis, which is a time consuming task. X-ray micro-Computed Tomography and Synchrotron Tomography are examples of imaging techniques that are advantageous in using the catalyst sample in a natural state, without involving any preparation step (Mousavi et al., 2005).

X-ray Computed Tomography (XRCT) is an imaging technique mostly used in the medical field. It is a non-invasive and non-destructive technique that can be used to obtain 3-D images of scanned samples and to visualise the internal structure of materials (Phillips and Lannutti, 1997; Burch, 2002). The sample size can range from several centimetres to less than one millimetre and the resolution of the equipment is in the order of micrometre and nanometre. The resolution is dependent on the size of the sample. In catalyst research XRCT has been mostly used in combination with mercury porosimetry to investigate pore size distributions and pore connectivity in catalytic supports, such as in solid-gel silica (Rigby et al., 2006; Rigby et al. 2008) and platinum-alumina (Rigby et al., 2011). It has also been used as a complementary method in providing the spatial distribution of pore networks within its resolution. However, no dynamic behaviour can be seen by XRCT. Drying and impregnations of catalysts, for example, which are very important in the catalyst research, cannot be fully characterised using XRCT. Moreover, its detectability level is at best limited to 2 microns, which can affect the visibility of the pores and cracks, when lower than 2 microns. The synchrotron method is used as an alternative to the XRCT, as it is more accurate and can make samples visible in a nano-scale.

1.3 Objectives

The current project was sponsored by Johnson Matthey, a leading catalyst manufacturer. In their research laboratory, a variety of characterisation techniques, including the XRCT is used in order to optimise their products. Johnson Matthey was interested in investigating the potential for using XRCT for characterisation of porous catalysts.

The following objectives are to be achieved in the current project:

- The evaluation of the X-Ray micro-Tomography in characterising catalyst structures
- The characterisation of formed particles and comparison of density/porosity distributions in catalyst supports
- The investigation of the metal distribution in impregnated catalysts to improve support selection and to understand deposition techniques.
- The comparison of the X-Ray micro-Computed Tomography and the Synchrotron X-Ray Tomography

1.4 Thesis layout

The thesis consists of 8 chapters.

Chapter 2: Literature review.

This chapter gives an overview of the preparation of heterogeneous catalysts and introduces the importance of processing parameters on their mechanical properties and porosity. The techniques used in the characterisation of catalysts' structures are provided prior to the

description of two non-destructive techniques, X-Ray micro-Computed Tomography and synchrotron tomography. An introduction to the physics behind the techniques are given in order to assist in the understanding of the image processing and the interpretation of results.

Chapter 3: Materials and methods.

This chapter describes the materials, and experimental procedures used to characterise the structure of the heterogeneous catalyst supports.

Chapter 4: Effect of processing route and formulation on density variation.

This chapter covers the capability of the X-Ray imaging technique to correlate density variation with processing route and formulation, as the internal structure depends on how catalysts have been made. The visualisation of the different types of catalyst support, the effect of the processing parameters and the formulation are also been covered in the chapter.

Chapter 5: Effect of processing conditions on the development of cracks.

This chapter is divided into two parts: (i) the development of a methodology in detecting and characterising cracks within the catalyst, using the XRCT; and (ii) the application of the method in investigating the effect of the water content, the ram extrusion speed, the drying temperature and the calcination process on the crack initiation and propagation.

Chapter 6: Distribution of copper nitrate trihydrate solution in the support by wet impregnation.

The visualisation and the investigation of the metal profile distribution within the catalyst support using the XRCT will be described in this chapter. Results helped in understanding the deposition technique of copper species in order to improve the their performance. Three

different parameters will be investigated; the concentration of the bulk solution, the impregnation time and drying conditions.

Chapter 7: Investigation of the microstructure of the catalyst support using synchrotron tomography.

The main objective of the experiments presented in this chapter is to assess the capability of the I13 synchrotron beamline for characterising: (a) the dynamic behaviour of the catalyst support under the drying process and the development of cracks; (b) the visualisation of the impregnation of the metallic solution and its distribution inside the support. Radiography and the tomography were used for the investigation of two study cases. In addition, a comparison between the X-Ray micro-Computed Tomography and the tomographic synchrotron was made.

Chapter 8: Conclusions

A summary of the results is presented.

1.5 Publications and conferences

The results from this work have been presented at different conferences as described below.

Conferences

- Johnson Matthey Academic Conference 2010 (JMAC 2010), Loughborough, UK, 14-15th April 2010. Structure characterisation of catalyst using X-Ray Computed

Tomography. Marie Lunel, Taghi Miri, Daniel Cairns, Liz Holt, Philip Hughes, Serafim Bakalis.

- Skyscan Usermeeting 2010, Mechelen, Belgium, 20-23rd April 2010. Structure characterisation of catalyst (Poster presentation). Marie Lunel, Taghi Miri, Serafim Bakalis.
- Johnson Matthey Academic Conference 2011 (JMAC 2011), Loughborough, UK, 6-7th April 2011. Structure characterisation of catalyst using X-Ray Computed Tomography. Marie Lunel, Taghi Miri, Daniel Cairns, Liz Holt, Philip Hughes, Serafim Bakalis.
- Skyscan Usermeeting 2011, Leuven, Belgium, 12-15th April 2011. Structure characterisation of catalyst (Poster presentation). Marie Lunel, Taghi Miri, Serafim Bakalis.
- Johnson Matthey Academic Conference 2012 (JMAC 2012), Loughborough, UK. Structure characterisation of catalyst using X-Ray Computed Tomography. Marie Lunel, Daniel Cairns, Gareth Hatton, Liz Holt, Philip Hughes, Serafim Bakalis

Publications

- M. Lunel, T.Miri, D.Cairns, P.Hughes, L. Holt, S. Bakalis. Studies of cracks on extruded alumina catalyst using the X-Ray micro-Computed Tomography (in preparation).
- M. Lunel, C. Rau, K. Wanelik, G. Hatton, L. Holt, S. Bakalis. Investigation of the microstructure of catalyst support using the new I13 synchrotron beam (in preparation).

CHAPTER 2 – LITERATURE REVIEW

2.1 Introduction

As mentioned in Chapter 1, structure characterisation at different length scales is important in order to understand and then to improve catalyst performance. This chapter describes the literature related to heterogeneous catalysts and its principal characterisation techniques. Firstly, an overview of the preparation of heterogeneous catalysts is presented. Focus is mostly given to the relationship between processing parameters and the effect of the process on the mechanical properties. In addition, an understanding on how porosity plays an important role is introduced. Secondly, different methods widely used for the structure characterisation in catalyst area, and their applications are given. Finally, a description of a non-destructive technique, the X-Ray micro-Computed Tomography technique, is given. The X-Ray micro-Computed Tomography section will provide an overview of the advantages and disadvantages to using the technique. Moreover, an introduction of the physics behind the technique is given in order to aid in the understanding of the image processing and the interpretation of results.

2.2 Heterogeneous catalyst

2.2.1 Definition

A catalyst is defined as a substance that increases the rate at which a chemical reaction approaches equilibrium without itself becoming permanently involved in the reaction (Richardson, 1989; Campanati et al., 2003). Properties of catalysts could change with time, depending on the use. The optimum catalyst is one that has a combination of properties such as activity, selectivity, lifetime and ease of regeneration (Acres et al., 1980; Campanati et al., 2003).

Heterogeneous catalysts are in the form of porous material, in which metal or metal oxides are bonded to the support (Richardson, 1989). Essentially, reactants are diffused across the pore network of the catalyst support and are adsorbed onto metal oxides, which are the active components. After reaction, final products are desorbed from the support and diffuse away. A scheme of a heterogeneous catalyst at different scales is shown in Figure 2.1.

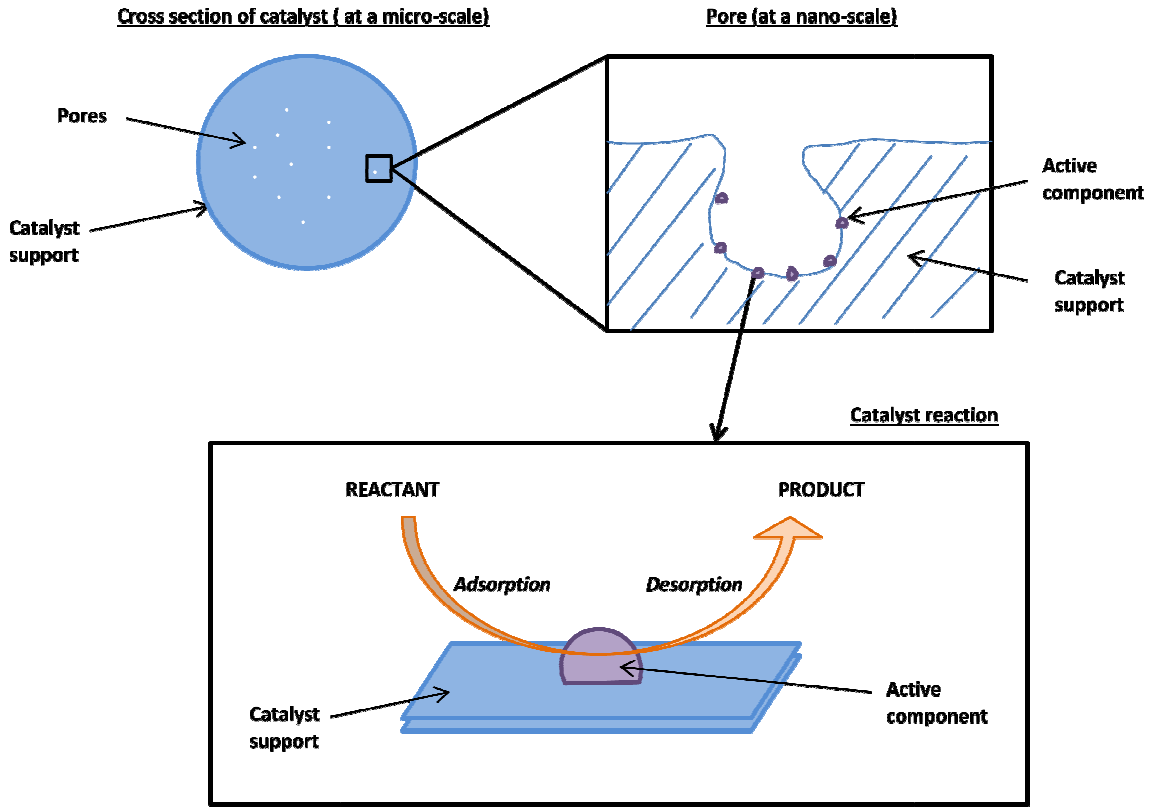

Figure 2.1: Scheme of heterogeneous catalyst.

2.2.2 Catalytic reaction

Reactions catalysed by solid catalysts could be divided into seven steps (Klaewka et al., 2011). Those steps are shown in Figure 2.2.

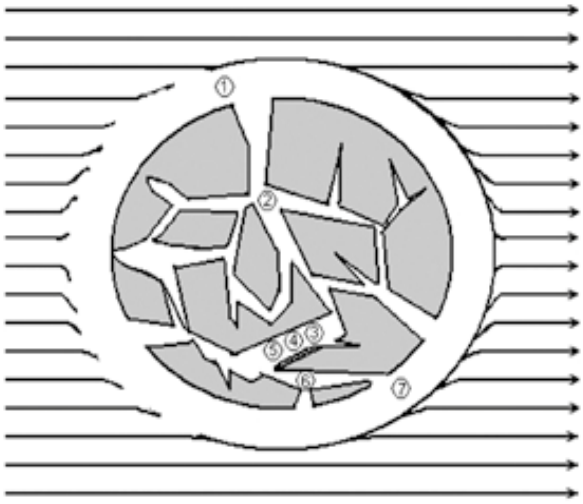

Figure 2.2: Steps in catalytic reaction (Richardson, 1989).

Digits from Figure 2.2 are as follows: (1) Diffusion of reactants from the fluid to the surface of the catalyst; (2) Diffusion of reactants through the pore network towards the internal catalytic surface; (3) Adsorption of reactant onto the catalytic surface; (4) Reaction on the surface of the catalyst; (5) Desorption of the products; (6) Diffusion of products towards the external surface; (7) Mass transfer of products from the surface to the bulk fluid.

2.2.3 Catalyst properties

As stated in Chapter 2.2.1, heterogeneous catalysts consist of a complex porous solid. Relationship between transport phenomenon occurring inside pores and structure of catalyst are important, as the internal porous networks influence transport processes in multiple ways (Rigby and Daut, 2002). Supported catalysts are characterised by different parameters, such as the amount of different components (e.g. active species and supports), shape, size, pore volume, pore size distribution and surface area (Rigby and Daut, 2002; Campanati et al.,

2003). Many works have been undertaken on pore size determination, pore structure and transport properties within catalyst.

Porous materials contain a certain empty voids space and the sum of all those empty space is called porosity (Sing et al., 1985). Porosity determines physical properties such as durability, mechanical strength, adsorption properties and mass transfer. Void spaces inside the material could be characterised in the form of cavities, pores and cracks. Those forms could have different shapes and sizes (Kaneko, 1994). Kaneko (1994) studied the classification of pores according to their structures and their states.

Classification of pores: Pores are classified according to the width (ϕ): (a) micropores $\phi <$ 2nm; (b) mesopores $2 < \phi < 50$ nm; (c) macropores $\phi >$50 nm (Sing et al., 1985; Leofanti et al., 1997). Also, four different geometries of pores are identified: cylinder, cone-shape, slit-shape and ink bottle (Kaneko, 1994). Those 3-D pore geometries are described in Figure 2.3.

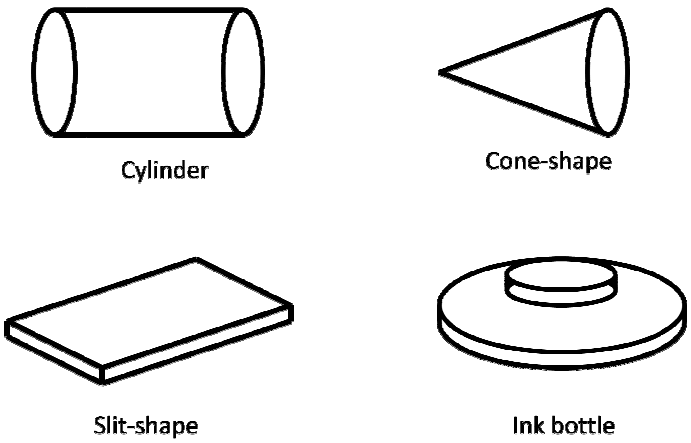

Figure 2.3: Different pores geometries (Kaneko, 1994).

Two types of pores could be visualised: open and closed pores (Kaneko, 1994). Closed pores mostly influences the mechanical properties of solid materials. External liquids or gases cannot go into closed pores. Open pores are connected to the external surface and are accessible to fluids. However, the accessibility is dependent with the pore geometry and size, as well as the nature of fluid (Kaneko, 1994).

Pore size distribution: The pore size distribution is related to the processing route (Miguélez-Morán et al., 2009). Drying and calcination steps could be crucial for the final product structure. For instance, an increase of the calcination temperature from 773 K to 973 K results in an increase in the volume of pores with a radius up to 100 nm and a decrease in their surface area (Walendziewski and Trawczyhski, 1994).

Surface area: Higher surface areas are obtained by increasing the pore volume. However, an increase of the pore volume could negatively affect the mechanical properties of catalyst supports (Perego et Villa, 1997). The total surface area might be increasing by decreasing the average of pore size, as described in Equation 2.1.

$$S = 2\frac{V_p}{r_p} \qquad \textbf{(Equation 2.1)}$$

where S is the surface area, V_p is the pore volume and r_p is the pore radius. Equation 2.1 is based on cylindrical-like shaped pores.

2.2.4 Catalyst preparation

As mentioned in Chapter 2.2.1, well-designed catalysts should have different qualities in terms of activity, stability, selectivity and regenerability. Controlling physical and chemical parameters is necessary to improve the catalyst performance. Therefore, methods used for the preparation of catalysts need to be carefully controlled. Preparation of catalyst follows a certain protocol. Drying and calcination processes are two unit operations occurring before or after the catalyst shaping, also called forming (Perego et Villa, 1997).

2.2.4.1 Shape of catalyst

Different textures and structures of catalyst can be found depending on the end use. Their shape and their size are determined by the end use (Richardson, 1989). Common types of catalysts used by industries are listed in Table 2.1.

Table 2.1: Common catalyst particles (*Richardson, 1989; **Doesburg et al., 1993 ; **Campanati et al., 2003)

Types	Characteristics *	Size **
Pellets	Made in high pressure press Shape cylindrical, very uniform, rings Use: Packed, tubular reactors	*D* = 3- 15 mm *H* = 3- 15 mm
Extrudates	Squeezed through holes Shape: irregular lengths, circular, star or lobe cross section Use: packed, tubular reactors, ebulating beds	*D* = 1- 50 mm *L* = 1- 30 mm
Spheres	Made by aging liquid drops Use: packed tubular reactors, moving beds	*D* = 1-10 mm
Granules	Fusing and crushing particles granulation Use: packed tubular reactors	*D* = 1-20 mm

D= Diameter; *H*= Height; *L*= Length

2.2.4.1.1 Extrudates

Extrusion is commonly used to manufacture catalyst supports (Perego et Villa, 1997; Campanati et al., 2003). A wet paste is forced through a die in order to obtain a cylindrical shape. Different geometries could be given to the catalyst support according to the shape of dies, such as trilobes or honeycombs for instance. A scheme for ram extrusion is shown in Figure 2.4.

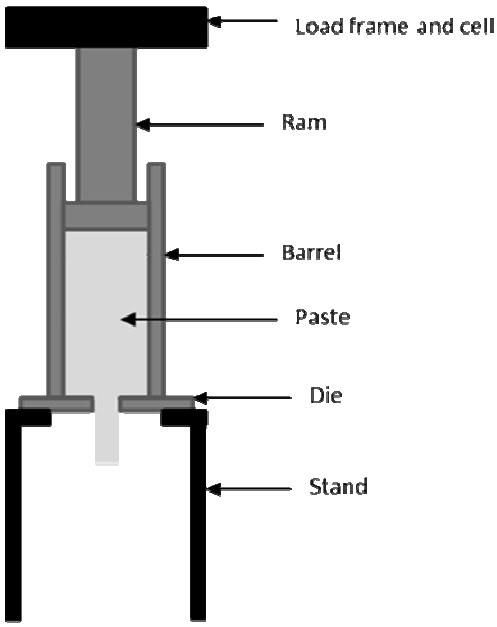

Figure 2.4: Scheme of the ram extrusion apparatus.

Different additives could be found in the formulation, such as compounds improving rheological behaviour (e.g. starch), or peptising agent for deagglomerating particles (e.g. nitric acid) (Campanati et al., 2003). The quality of extrudates depend on many variables which include mixing time, water content, extrusion temperature, drying and calcination processes (Perego and Villa, 1997).

2.2.4.1.2 Granules

The 'snowball effect' could be the best method to describe granulation process. The equipment used for that process is a round dish rotating on an axis, described in Figure 2.5 (Doesburg et al., 1993).

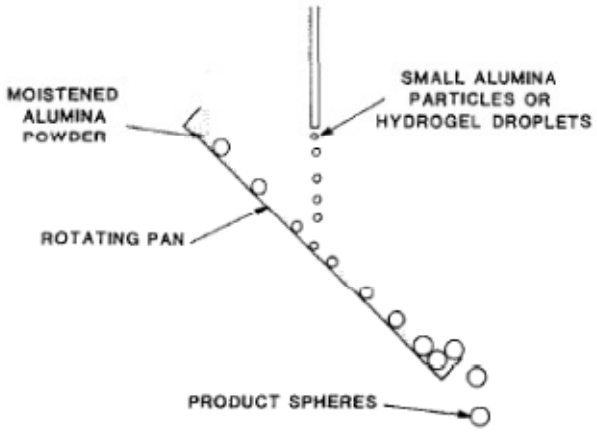

Figure 2.5: Production of granules using round dish method (Doesburg et al., 1993).

Small particles are under constant movement due to the rotation of the recipient, while solvent (e.g. water) is sprayed on it. The surface of particles become wet and the rotation leads to an agglomeration of the particles (Perego et Villa, 1997; Campanati et al., 2003). Therefore, it is a moisture dependent process, as size and shape of granules are related to the liquid input (Doesburg et al., 1993). Granules have spherical geometry.

2.2.4.1.3 Pellets

Pellets are obtained by tableting. Dry powder is poured in a die and is compacted between 2 punches (Perego et Villa, 1997; Campanati et al., 2003). The mechanism is shown in Figure 2.6.

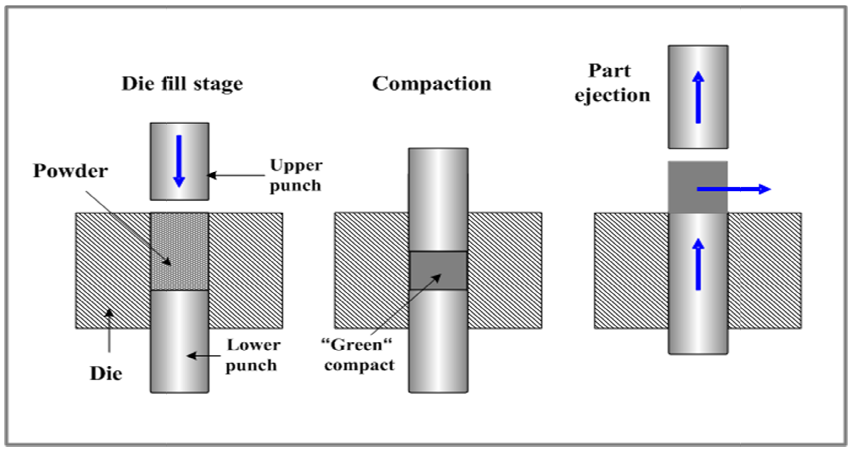

Figure 2.6: Compaction process (www.substech.com).

The powder could be a mix of different main ingredients with the addition of lubricants. That addition into the formulation could increase the quality of the final product (Perego et Villa, 1997). Lubricants, such as graphite, are used to decrease friction between the surface of the tablets and the die wall, and therefore, the ejection force is reduced. The density of the tablets could also increase depending on the amount of lubricants added (Huang et al., 2002). The pressure applied to tablets could heavily affect density and porosity of the final product (Perego et al., 1997).

2.2.4.2 Drying

The drying process is an evaporation of solvent with an application of heat (Bashaiwoldu et al., 2004). The drying process could be divided into three steps: preheating, constant rate and falling rate periods (Lekhal et al., 2001). Different drying techniques could be found in the literature, such as atmosphere (Johansson et al., 1995), conventional oven (Ahange et al., 1990) and fluidised bed dryer (Pinto et al., 1993). By removing the fluid (usually water) from

pores of the catalyst structure, the structure could collapse leading to a decrease of pore volume as well as surface area (Richardson, 1989; Perego et al., 1997). Drying has an impact on the properties of the catalyst support, and therefore, the quality. Studies were carried out to understand the effect of different drying techniques on morphological and mechanical properties, such as strength (Bataille et al., 1993) and porosity of tablets (Bataille et al., 1993; Kleinebudde, 1994).

2.2.4.3 Calcination

Drying is followed by a calcination process, which is a treatment under high temperature. Several modifications happen during calcination, such the loss of bonded water, and the modification of the structure which leads to a stabilisation of mechanical properties (Perego et al., 1997). In terms of structural properties, micro-pores on γ- alumina collapse by increasing the calcination temperature (Richardson, 1989). The main consequence is an increase of the average pore size (as shown in Figure 2.7) and therefore, a change of the pore size distribution. The calcination temperature could only be used for controlling the pore size distribution in the range of pore below 50 nm and it does not influence the size of the macropores.

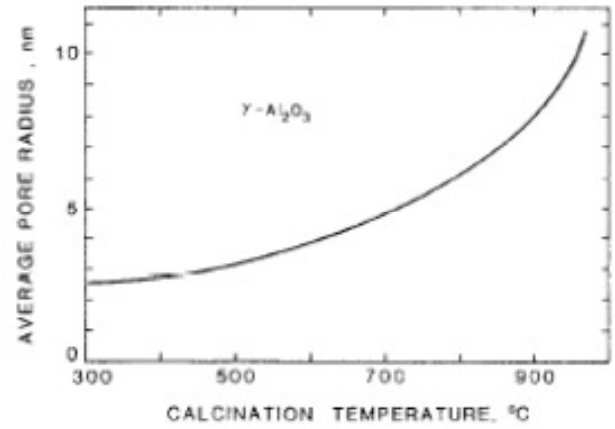

Figure 2.7: Effect of the calcination temperature on the pore size of γ- alumina (Richardson, 1989).

2.2.5 Supported catalyst

2.2.5.1 Support selection

The catalyst support is selected according to certain characteristics, such as desirable mechanical properties (attrition resistance and strength), stability under reaction, high surface area, porosity (smaller pores implies high surface area) (Satterfield, 1970).

2.2.5.2 Impregnation

Impregnation is defined as a procedure where a volume of active component is absorbed by the pores of the support (Bond and Tahir, 1991). Catalysts are prepared either by wet impregnation or incipient wetness impregnation. Those two impregnation methods are shown in Figure 2.8.

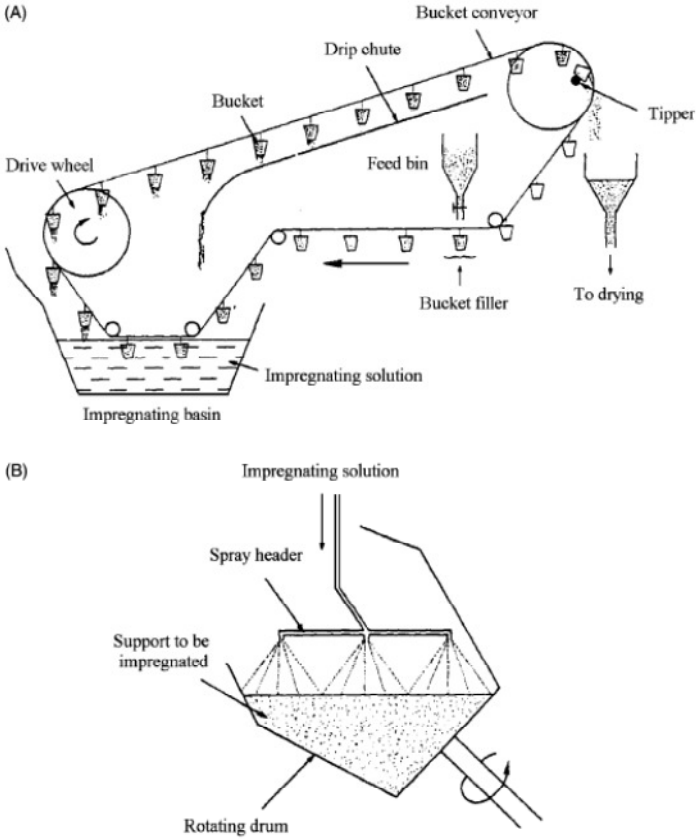

Figure 2.8: Two different impregnation methods. A) Wet impregnation; B) Incipient wetness impregnation (Satterfield, 1970).

Wet impregnation: The sample is immersed into an excess metallic salted solution for the time necessary for the impregnation. Then, the sample is removed and dried. (Satterfield, 1970)

Incipient wetness impregnation: Incipient wetness impregnation method is also called capillary or dry impregnation. The catalyst support, having a known pore volume, is in contact with a specific concentration of solution. The volume of the impregnating solution corresponds to the volume of pores characterised previously (Satterfield, 1970; Acres, 1980).

Impregnation involves two main phenomena (Goula et al., 1992): (i) diffusion of the solute into pores and (ii) adsorption of the solute onto the support. The distribution of the active component depends on the equilibrium between diffusion and adsorption.

2.2.5.3 Transport phenomena involved in wet impregnation

Figure 2.9 shows transport phenomena involved in wet impregnation at low concentration.

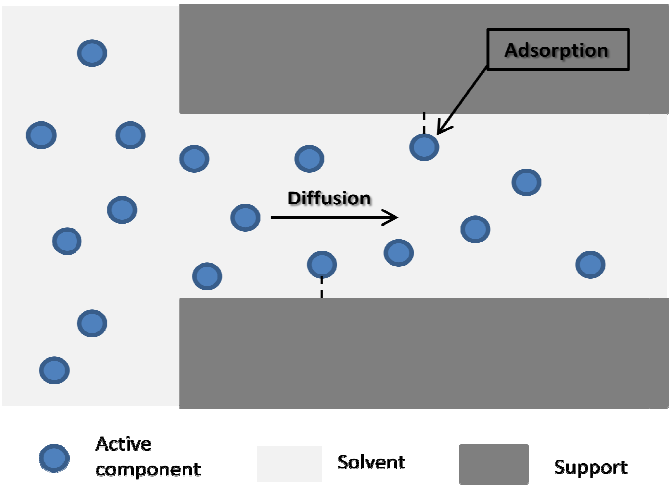

Figure 2.9: Transport phenomena involved in wet impregnation at low concentration.

In wet impregnation, two types of phenomena occur: Diffusion of the impregnation solution inside porous network and adsorption of active species on pores surface.

2.2.5.3.1 Diffusion

Diffusion is a process in which ions, molecules or small particle migrate from a region of high concentration to a region of lower concentration. The rate of migration of material by diffusion is described mathematically by Fick's first law, as shown by Equation 2.2., which relates the diffusion flux *J* to the gradient of the change in concentration (*dc/dx*).

$$J = -D\,\frac{\partial c}{\partial x} \qquad \textbf{(Equation 2.2)}$$

where *J* is the diffusion flux of material per unit area (mol/m^{2}s); measures the amount of substance that will flow through a small area during a small time interval, *D* is the diffusion coefficient or diffusivity in (m^2/s), *c* (for ideal mixtures) is the concentration (mol/m^3) and *x* is the position (m). The negative sign indicates that flow is down the concentration gradient (from high to low concentration).

Internal diffusion of active components is related to the pore dimension (Perego and Villa, 1997). The diffusion becomes limited and restricted below a certain pore size, as shown in Figure 2.10.

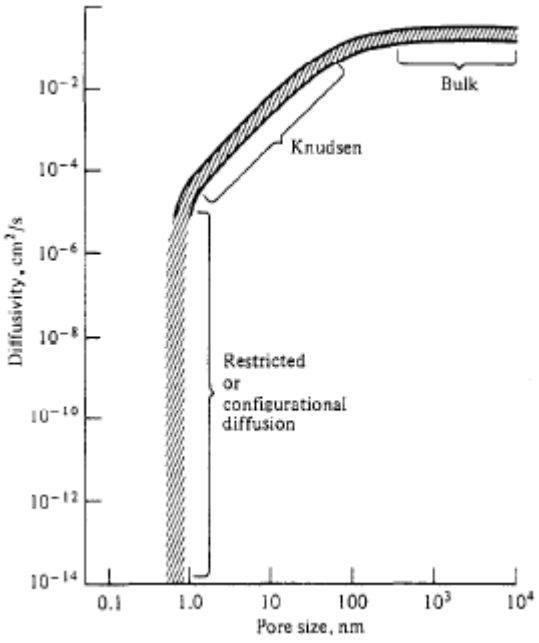

Figure 2.10: Effect of pore dimension on the diffusivity (Perego and Villa, 1997).

2.2.5.3.2 Adsorption

Adsorption is dominated either by kinetics or thermodynamics. The deposition of active components onto the catalyst support is described by the Langmuir isotherm. The adsorption is very important, as it defines the final metal distribution (Lekhal et al., 2001). Many factors could have an impact on the metal adsorption, such as the presence of acids and salts in the impregnation solution (Spieker and Regalbulto, 2001). The effect of pH and ionic strength on the metal distribution was studied by Lekhal et al., (2004). They found that a strong adsorption occurred at low pH value, and the ionic strength decreases the effect of the pH.

2.2.5.4 Metal profile

After impregnation, different metal profiles could be obtained depending on the parameters of the processing conditions, such as impregnation time and drying process (Lekhal and al., 2001). The four main types of metal profile are: uniform, egg-shell, egg-white and egg-yolk. Figure 2.11 shows those four metal distributions.

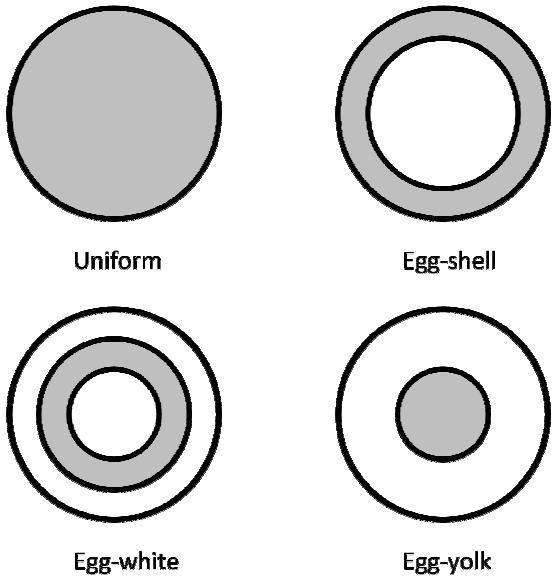

Figure 2.11: Types of metal distribution after the impregnation process (Lekhal and al., 2001).

In terms of catalytic activity, each metal profile has its own characteristics:

Uniform: The active components cover all the catalyst support. That distribution is mostly used for small catalytic activity. Diffusion is dominant as a transport mechanism.

Egg-shell: The active components are located on the surface of the support. That metal profile is used when fast reaction is required.

Egg-white: The active components are located in a small area between the surface and the centre of the support.

Egg-yolk: The active components are in the centre of the support.

During impregnation, the metal distribution is controlled by several parameters: such as nature of the support, processing parameters, initial concentration of the solution, impregnation time and temperature during impregnation. For impregnation of Ni in alumina support, the initial concentration of Ni strongly affects the metal profile (Kominaya et al., 1980). Moreover, the impregnation time and the initial concentration of metallic ions have a strong effect on the metal distribution (Assaf et al., 2003).

However, the metal profile obtained after the impregnation step could change after drying, depending on the strength of the adsorption (Lehkal et al., 2001; Lehkal et al., 2004).

2.2.5.5 Drying after impregnation

The drying step also affects the distribution of the active phase. Lee and Aris (1985) investigated catalysts redistribution during drying using a simplified model of a capillary tube where evaporation takes place at the open end. In their model, solute precipitation and film flow were neglected. The authors considered that initial solutes distribution was altered during drying, as a result of the interaction between adsorption, convective and diffusive transport. Models on drying were developed. Those models accounted for heat transfer from the hot air to the wet support, solvent evaporation in the support, convective flow towards the support external surface due to the capillary force, and metal diffusion and metal deposition due to adsorption and crystallisation (Regalbuto, 2006). The outcome of those showed that the

convective flow is the main driving force to transport the metal component and the solvent towards the support external surface, while the back-diffusion causes metal to transport towards the support centre. The film drying mechanism was also neglected in those studies. Drying mechanisms after impregnation are explained in details by Regalbuto (2006).

In drying, the solution in the pores will become oversaturated and precipitation takes place. In principle, rapid evaporation is favourable because it causes rapid saturation associated with a high dispersion. However, if fast drying occurs by rapid heating of the wet support catalyst, boiling phenomena might result in an inhomogeneous distribution. Slow drying in combination with precursor salts will yield an egg-shell distribution. That is the result of the crystals formed initially at the pore mouths of the support, initiating migration of the impregnation liquid towards the outer surface of the support by capillary forces (Mul and Moulijn, 2005).

The liquid solution migrates by capillary flow and diffusion (Neimark et al., 1981; Lee and Aris, 1985; Lehkal et al., 2001). At the same time, a redistribution of active components might happen by adsorption and desorption phenomena (Neimark et al., 1981; Lee and Aris, 1985). During preheating and constant-rate period, water is going towards the surface of the support by capillary flow (Kowalski, 2000), whereas active components are transported by 2 transport mechanisms: by liquid convection and by diffusion (Lehkal et al., 2001). Therefore, the surface is kept saturated by the moisture content, and drying rate is dependent on the water evaporation.

Several authors demonstrated that drying process affects significantly the metal profile getting after impregnation (Maatman and Prater, 1957; Neimark et al., 1981; Lee and Aris, 1985). Active components move towards the centre of catalyst by capillary flow, as suggested by

Maatman and Prater (1957). Drying of copper in γ-alumina (Van Der Berg and Rijnten, 1979), nickel in γ-alumina (Uemura et al., 1987; Li et al., 1994), and copper in α-alumina (Kotter and Riekert, 1994) were studied. The tendency of egg-shell profile is observed under fast drying conditions, whereas the uniform profile is realised under lower drying condition. However, others authors showed that egg-shell profile could be obtained after drying at low temperature. By increasing the drying rate, the uniform profile is visualised (Komiyama et al., 1980). Lee and Aris (1985) demonstrated that active components are adsorbed at the surface of the support at the beginning of drying process. Metal distribution would depend on the strength of chemical bonds between ions and surfaces. If a strong adsorption occurs, egg-shell profile would be obtained. In the case of weak adsorption, active components would tend to go towards the middle of catalyst support by a transport mechanism called back-diffusion (Lekhal et al., 2010). Thus, uniform or egg-yolk profile could be observed.

Overall, active components concentration profile could be controlled by the condition of impregnation and drying process.

2.3 Characterisation techniques of catalyst

As mentioned previously, heterogeneous catalysts consist of very tiny metal particles, in the order of Angstrom scale supported on a high specific area material (Richardson, 1989). Performance of catalysts depends on catalytic activities and surface area available for reactions, which is linked to the porous network (Trimm et al., 1986; Page, 1987). Therefore, the knowledge of the porous structure is crucial in order to control the processing parameters during catalyst preparation. Heterogeneous catalysts have a hierarchical porous structure

going from micrometre to nanometre (Page, 1987). Porous structures can be characterised by different parameters, such as void fraction also called porosity, pore size distribution, specific surface area, pore network and connectivity (Rigby and Daut, 2002).

In the last fifty years, several techniques have been used in order to characterise catalyst structure from the traditional techniques (such as nitrogen gas adsorption method and mercury porosimetry) to the imaging techniques (such as Scanning Electron Microscopy, Transmission Electron Microscopy, X-Ray micro-Computed Tomography, and Synchrotron).

2.3.1 Traditional methods

Nitrogen adsorption and mercury porosimetry are two methods commonly used to characterise pore structures of catalysts (Farber et al., 2003; Rigby et al., 2004b; Rigby et al., 2008). Both provide information on pore volume and pore size distribution (Rigby et al., 2003a). Moreover, the determination of pores connectivity within the material is possible (Portsmouth and Gladden, 1991).

2.3.1.1 Mercury porosimetry

2.3.1.1.1 Principle

Mercury porosimetry is based on the principle that mercury is a non-wetting fluid for most materials, and an imposed pressure is required to push into the pores of a porous solid. Imposed pressure is inversely related to pore size and so mercury will firstly enter the large

pores of the porous network followed by the smaller ones as the pressure is increased. The following relationship links imposed pressure to pore size (Washburn, 1921):

$$p = -\frac{2\gamma\cos\theta}{r} \qquad \textbf{(Equation 2.3)}$$

where p is the imposed pressure, γ is the surface tension, θ is the contact angle and r is the radius of the pore. γ and θ are typically taken as 480 dynes.cm^{-1} and 130^{o} respectively for alumina (Rigby and Fletcher, 2004).

2.3.1.1.2 Advantages and drawbacks

Mercury porosimetry is commonly used to characterise pore structure of catalysts and is capable of probing pore sizes between 500 µm and 2 nm (Rigby et al., 2003a). The main drawback is that only pores reaching the surface of the catalyst sample can be determined. Prior to the experimental work, a preparation is necessary, as the sample must be dry. Without the drying process step, mercury cannot intrude into the sample because voids are filled up with another liquid (Ek et al. 1995). Note that samples with a tiny pore shape and size are difficult to degas (Allen 1997). Mercury porosimetry tends to overestimate the volume of the smallest pores (Auvinet and Bouvard, 1989). The specific shape of pores, i.e. ink-bottle like-shaped (Dees and Polderman 1981), as well as interconnected pores (Allen 1997) tends to shift the volume pore size distribution towards smaller pores. Moreover, the method is very rarely used in measurement of quality control, because the time consume for a single analysis is approximately 30 – 45 minutes (Webb and Orr, 1997).

2.3.1.2 Nitrogen gas adsorption method

2.3.1.2.1 Principle

Total pore volume, pore size distribution and specific surface area can be determined from the adsorption or the desorption phase. The volume pore size distribution is determined according to the BJH model (Barrett et al. 1951). The Kelvin equation is used to calculate the relative pressure of nitrogen in equilibrium with a porous solid, and applied to the pores size where capillary condensation takes place. The relationship is stated in Equation 2.4 (Thomson, 1871).

$$ln\frac{p}{p_0} = \frac{2\gamma V_L}{rRT}cos\theta \qquad \textbf{(Equation 2.4)}$$

where p is the equilibrium vapour pressure of a liquid in a pore of radius r, p_0 is the equilibrium pressure of the same liquid on a plane surface, γ is the surface tension of the liquid, V_L is the molar volume of the liquid, θ is the contact angle between liquid and pore walls, r is the pore radius, R is the gas constant and T is the absolute temperature.

2.3.1.2.2 Advantages and disadvantages

Nitrogen gas adsorption is capable of determining the pore diameter range from 0.3 to 300 nm. That size range is not completely covered by mercury porosimetry. Only opened pores are determined, and only the cylindrical pore model is used in pore size distribution measurements (Allen, 1997).

The main disadvantage of the nitrogen gas adsorption is the time required for one analysis, which may be a period of several hours. In addition, samples come into contact with liquid nitrogen having a temperature of -196°C. The abrupt difference in temperature might destroy the sample and therefore, the analysis may not be possible.

2.3.1.3 Porosimetry technique

By comparing the time required for the analysis of the pore structure, mercury porosimetry is faster than nitrogen adsorption. Both methods are based on surface tension, capillary forces and pressure. Parameters, such as total pore volume, volume pore size distribution and specific surface area/total pore surface area, could be determined.

In terms of morphology, spatial distribution of pores and interconnectivity, those techniques do not provide any information. In addition, porosimetry techniques are based on the assumption that pores are cylindrical. Therefore, pore shapes are not considered, which shows highlights the limitation of the intrusion techniques.

2.3.2 Imaging techniques

Structure characterisation of catalyst using imaging techniques at different scale is crucial to understand its physical properties and then to improve its performance. Different imaging techniques have been used for the characterisation of the structure of catalysts in order to determine the pore structure and the pore network, such as the electron microscopy (Yao et

al., 1993; Gai, 2001) and the tomography techniques including electron and x-ray tomography (Tariq et al., 2011a; Tariq et al., 2011b).

2.3.2.1 Electron microscopy

Electron microscopy (EM) is a very useful 2-Dimensional imaging technique tool to investigate the internal structure and the chemistry of heterogeneous catalyst, from the macroscopic to the atomic scale (Gai, 2001; Datye, 2003). Those methods include the Scanning Electron Microscopy (SEM) and the Transmission Electron Microscopy (TEM), in which different techniques could be found, such as the High Resolution Transmission Electron Microscopy (HRTEM) for instance.

2.3.2.1.1 Scanning Electron Microscopy

The principle of Scanning Electron Microscope (SEM) is similar to the conventional light microscope, where light is replaced by electrons. The SEM produces a focused electron beam across a sample surface, providing high-resolution images of the sample surface, revealing details down to 5 nm in size. The resolution depends on the equipment. Resolution, magnification and the depth of field are based on the same properties. The SEM technique and the physics behind it are explained by Goodhew and Humphreys (2001).

In the field of heterogeneous catalysts, SEM images and data could be combined with results coming from of several different techniques, such as spectroscopic, diffraction, adsorption and other microscopic methods. The combination contributes to the understanding of structure

formation of the catalyst support, from the creation of different phases to the causes of catalyst aging (Lomic et al, 2004). The choice of catalyst material, the influence of catalyst preparation on catalyst properties, structure/texture and catalyst morphology during the catalyst processing could be analysed. SEM provides information on the surface of catalyst support.

Direct observation with the SEM was used to study of the effects of various thermal treatments on the modification of the morphology like pore geometry, topography and to both particle size and shape (Reimschussel and Fredericks, 1969).

2.3.2.1.2 Transmission Electron Microscopy

Transmission Electron Microscopy (TEM) is an important imaging technique used in the characterisation of catalysts (Datye, 2003), in order to obtain structural information of nano-particles (Wallenberg, 1985; Li, 2008). Two high-resolution imaging modes exists in the transmission electron microscopes: high-resolution transmission electron microscopy (HRTEM) and scanning transmission electron microscopy (STEM). TEM and STEM are related techniques that use an electron beam to image an ultra-thin layer of sample. TEM and STEM have a better spatial resolution, as the details could be seen in a range of 0.3-2 nm. Both techniques require a preparation of samples (Datye, 2003).

As mentioned previously, electron microscopy provides information on the external structure at the nanoscale (Datye, 2002). Sample preparation is necessary before visualising the object through the microscope (Datye, 2003). Even though these analytic methods bring a lot of advantages, these techniques would not yield information about the 3-D distribution of the

element of interest within the sample, and the drawback for a routine analysis is the time consuming nature of both preparation and analysis.

2.3.2.2 Electron Tomography

Electron microscopy can be extended from a 2-D to a 3-D analysis by electron tomography using bright-field TEM and HAADF STEM (Weyland, 2002). Electron tomography can be used as a tool for 3-D structural characterisation. In order to visualise the structure on the order of nanometres, the material can be 100 nm in size. In one of their studies, Tariq et al. (2011a) compared the potential of different techniques in terms of resolution and the volume interrogation capabilities. They used several tomographic techniques in an attempt to characterise and quantify pore structures in different resolutions. Figure 2.12 shows a representation of 4 tomographic techniques with their resolution and their volume analysis capacities. Those methods are the 3-D atom probe, Electron Tomography (ET), Dual beam focused ion beam tomography (DB-FIB) and synchrotron X-ray tomography (XRT).

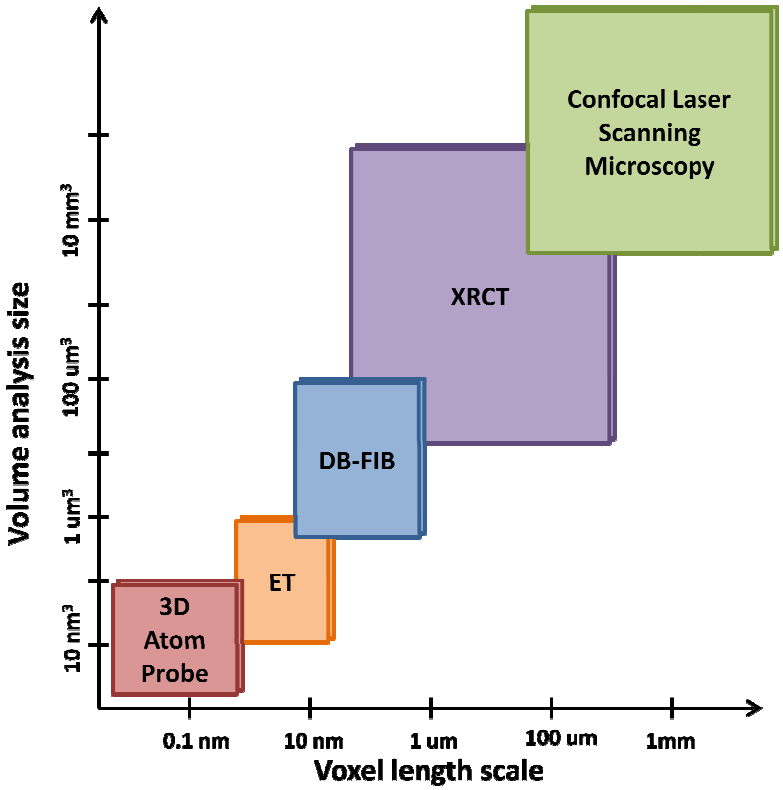

Figure 2.12: Representation of different electron tomographic techniques with the resolution and the volume analysis capabilities. From left to right: 3-D atom probe, Electron Tomography (ET), Dual beam focused ion beam tomography (DB-FIB), X-Ray Computed-Tomography (XRCT) (Tariq et al., 2011a).

The hierarchical pore structures going from micrometres to nanometres, demonstrated by Page (1987), could be visualised by using several tomographic techniques with different resolutions (Tariq et al., 2011b), as shown in Figure 2.13.

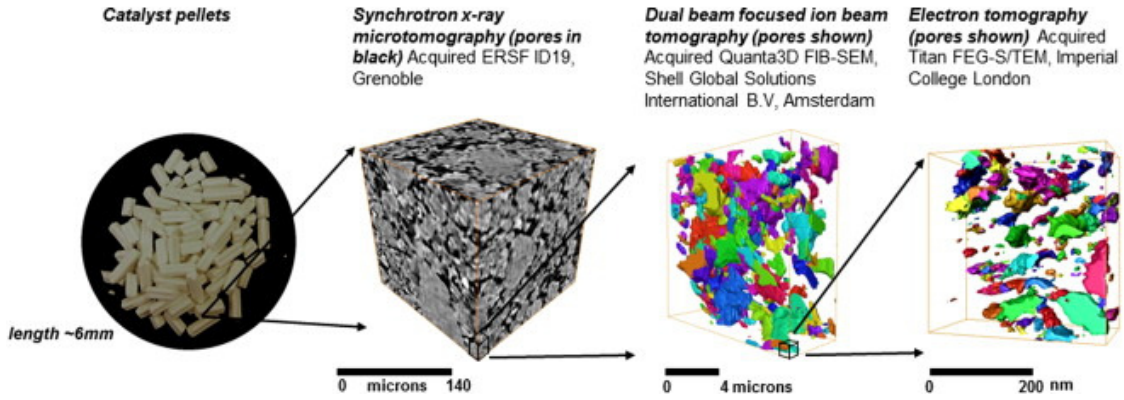

Figure 2.13: Visualisation of pores distribution inside the catalyst pellets at different length scale by using adequate imaging techniques (Tariq et al., 2011b).

In addition, Zečević et al. (2013) highlighted recent advances in electron tomography for the characterisation of solid catalyst in their review. From those imaging techniques, quantitative information on pore connectivity, particle size distribution and 3-D mapping of nanoparticles in porous catalyst supports could be collected.

The knowledge of catalyst structure at a different scale needs to be understood in order to modify the method preparation and then, to get the desired internal structure. Morphological parameters (such as pore size, pore volume and surface area) change during the catalyst preparation (Leofanti et al., 1997). Among those imaging techniques, XRCT provides the most advantages for the routine analysis basis.

2.4 X-Ray micro-Computed Tomography

Originally developed for medical science, the X-ray micro-Computed Tomography is widely used in diverse disciplines, as mentioned in Chapter 1. XRCT is a non-invasive and non-destructive technique that can be used to obtain a 3D image of a scanned sample and to visualise the internal structure of material (Burch et al., 2002).

2.4.1 Brief history of the XRCT

The X-ray was discovered in 1895, providing the major development in the medical field. The Computed Tomography (CT) was developed in early 1970's by Godfrey Hounsfield and Allen Cormack. That technique provides cross sectional image, which can show smaller contrast differences than the conventional X-Ray images. In 1979, G. Hounsfield and A. Cormack were awarded the Nobel Prize in medicine for that invention. At the early stage of the technique development of the first scanner, nine days were necessary to acquire data and to reconstruct the first image (Hsieh et al., 2003).

2.4.2 Physics of computed tomography

2.4.2.1 Projection imaging

XRCT uses a combination of X-ray microscopy and tomographic algorithms. Those algorithms are based on the contrast in X-ray images generated by the differences in X-ray attenuation. X-Ray attenuation is linked with density differences within the specimen material

(Mousavi et al., 2005). The X-rays are passed through an object, which is itself rotated. An array of detectors measure the attenuation of X-rays penetrating the sample (Sinka et al., 2004). Then, 2-D projected images are obtained and those are stacked to reconstruct the 3-D image of the material. A diagram of the XRCT principle is shown in Figure 2.14.

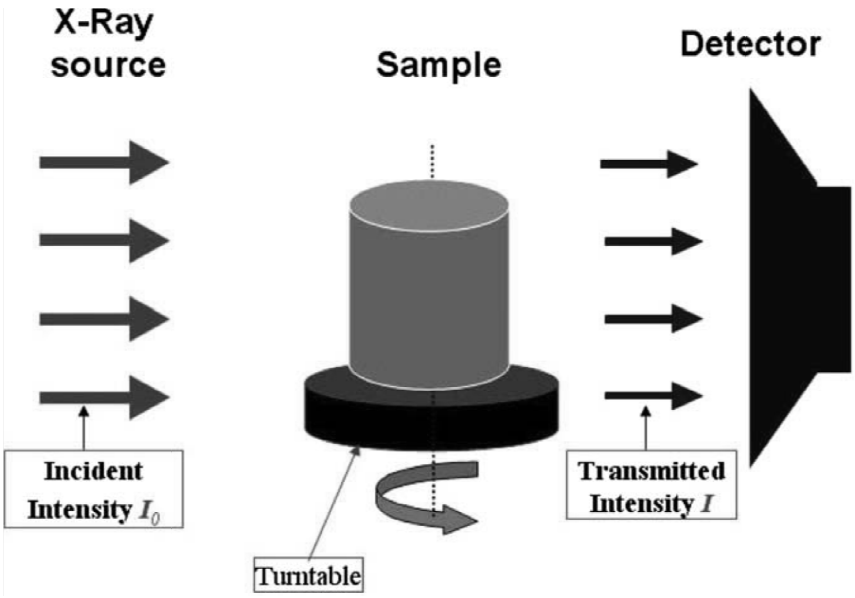

Figure 2.14: Principle of XRCT (Miguélez-Morán et al., 2009).

The attenuation of X-ray beam is dependent on the thickness and the attenuation coefficient of the material. The transmitted beam intensity is given by the Lambert-Beer's law, as shown in Equation 2.5.

$$I = I_0 \, e^{-\mu x} \qquad \textbf{(Equation 2.5)}$$

where I is the intensity of transmitted radiation, I_0 is the intensity of incident radiation, μ is the attenuation coefficient of the material and x is the thickness of the material (Taud et al., 2005).

A direct link exists between the actual material densities and the measured attenuation coefficients (μ) from XRCT. The attenuation coefficient is being directly linked to the grey value (GV) which is between 0 and 255 in 8-bit greyscale images (Sinka et al., 2004).

2.4.2.2 CT numbers

The signal received in each point in the reconstructed images is called the CT number or pixel (Taud et al., 2005). CT number is expressed in Hounsfield's units. The definition is demonstrated by the following equation.

$$CT = 1000\frac{\mu-\mu_w}{\mu_w} \qquad \textbf{(Equation 2.6)}$$

Where μ_w is the attenuation coefficient of pure water and μ is the attenuation coefficient of the material. Based on calibration measurement, water has CT value equal to 0, whereas air CT value is equal to -1000. High density materials have higher CT number (Taud et al., 2005). Basically, a CT image is a matrix of CT numbers. CT value could be transformed to grey scale value.

2.4.2.3 Density measurement

Pixel value is a function of the average density and the composition of the material (Maire et al., 2003). The degree of X-ray attenuation depends on the atomic number and the mass density of the sample (Van Geet et al., 2000; Salvo et al., 2003).

$$\mu = \rho \cdot \frac{Z}{A} \cdot N_{AV} \cdot \left(a + b \cdot \frac{Z^{3.8}}{E^{3.2}}\right) \quad \textbf{(Equation 2.7)}$$

where ρ is material density, Z is effective atomic number, A is effective atomic weight, N_{AV} is Avogadro's number, a and b are material constants and E is the X-ray energy.

2.4.3 Computed Tomography imaging process

An overview of the XRCT with different major components is shown in Figure 2.15.

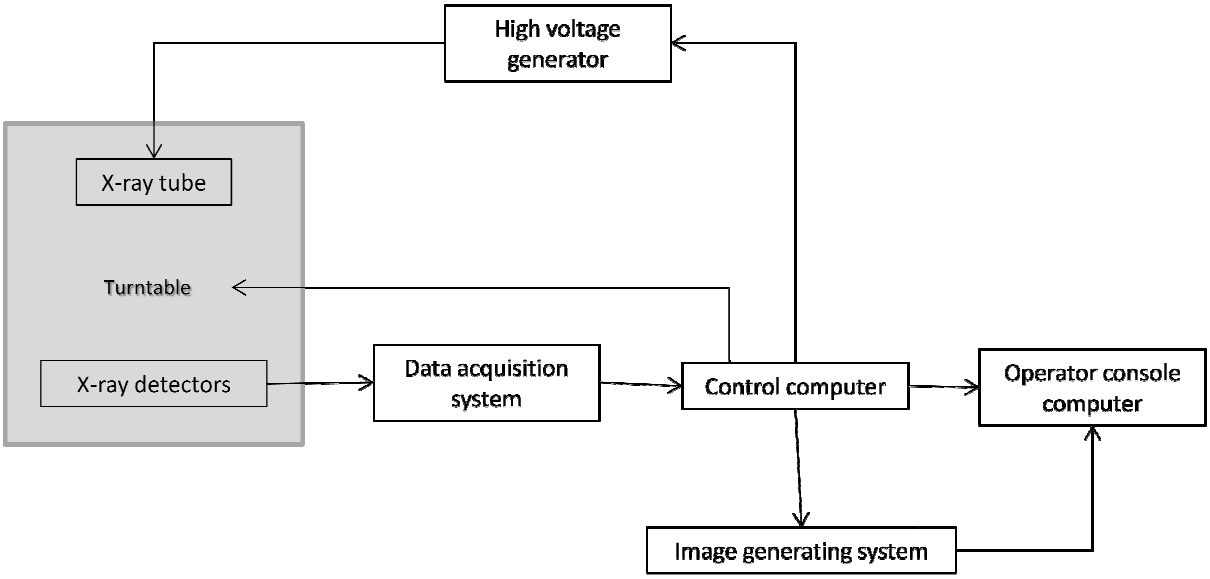

Figure 2.15: Overview of X-Ray Computed Tomography system.

Essentially, X-Ray Tomography system has mainly three parts, which are the X-ray source, the X-ray detector and the turntable (Mees et al., 2003). In our scanning system, the X-ray source and the detector are fixed, whereas the sample is under rotation on the turntable. Scans consist of two steps: data collection and image reconstruction.

2.4.3.1 Data collection

In order to collect data, the sample is photographed at different angles while being exposed to X-rays. The sample is placed between the X-ray tube and the detector (Burch, 2002). X-Ray tube generates X-rays. X-rays are a form of electromagnetic radiation and the wavelength is between 0.3 pm and 3.0 nm. Looking at the whole X-ray spectrum, the beam is polychromatic, as demonstrated in Figure 2.16.

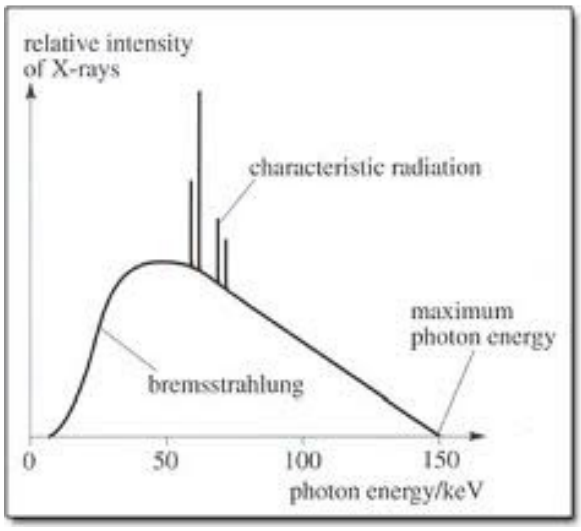

Figure 2.16: An X-ray spectrum (P. Allisy-Roberts and J. Williams, 2008)

X-rays of high energy can penetrate objects, allowing physical characterisation (Clausnitzer and Hopmans, 2000). X-rays have 3 ways of interacting with the sample, either by absorption, by scattering or by transmission. Figure 2.17 shows the interaction of the X-Ray beam with matter.

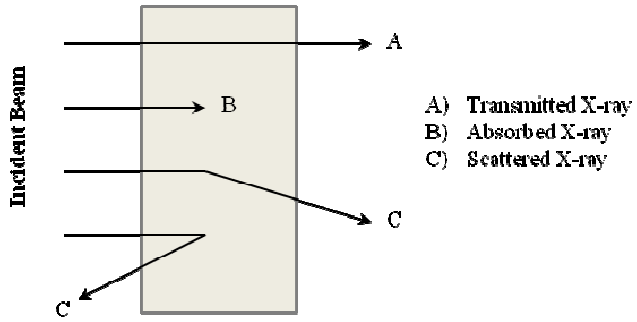

Figure 2.17: Interaction of X-rays with matter (P. Allisy-Roberts and J. Williams, 2008).

The detector array measures the intensities transmitted through the sample (Sinka et al., 2004). Therefore, the X-ray image is formed by the transmitted photons (P. Allisy-Roberts and J. Williams, 2008). More details about the physic parts of X-ray tube and X-ray detector are given in the literature by different authors (Flannery et al., 1987; Clausnitzer and Hopmans, 2000; Salvo et al., 2003; Allisy-Roberts and Williams, 2008). At the end of the data collection process, two dimensional projected images are acquired.

To maximise the quality of the image, different parameters could be controlled: (i) the position of the sample, (ii) intensity and (iii) voltage of the X-ray tube. The configuration also depends in the desired resolution and the sample size (Flannery et al., 1987).

2.4.3.2 Image reconstruction

To reconstruct images from the transmitted intensity measured, a mathematical algorithm is used (Burch, 2002). In the case of the cone beam projection, many mathematical algorithms

could be used (Feldkamp et al., 1984). However, the Feldkamp algorithm is typically used, as it provides the best reconstructed image quality in comparison to the other algorithms. That algorithm is based on the combination of two methods: convolution and filter back-projection (Feldkamp et al., 1984). The backprojection method is based on inverting the set shadow images (Radon, 1917). The superposition of all backprojected images reconstructs the object (Conesa-Boj et al., 2010). A scheme of the reconstruction approach is shown Figure 2.18.

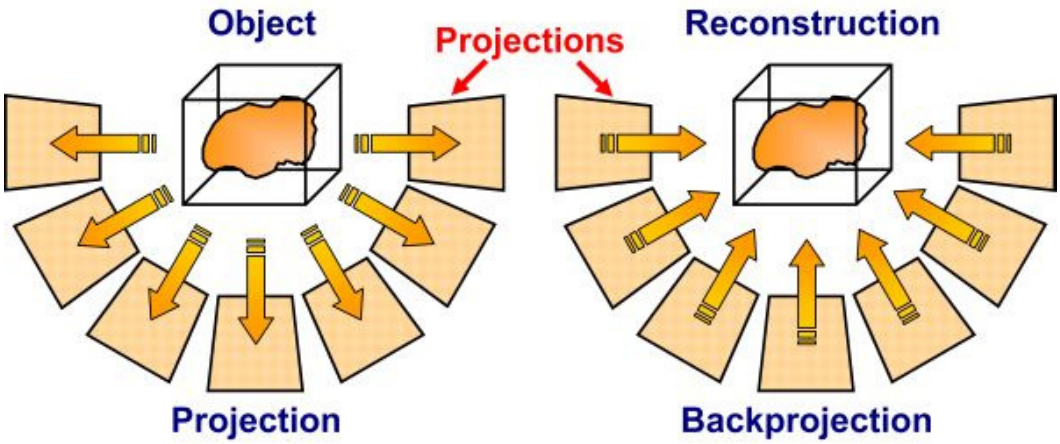

Figure 2.18: Scheme of the reconstruction approach (Conesa-Boj et al., 2010).

After the reconstruction process, a 3-D tomographic image is obtained. Details of convolution and the filter back-projection are explained by many authors (Feldkamp et al., 1984; Shih et al., 2000; Allisy-Roberts and Williams, 2008).

2.4.4 Artefacts

X-rays are produced by radioactive decay; they are always polychromatic with a wide range in energy. This complicates quantitative analysis and creates artefacts in the CT images, due to the stronger attenuation of X-rays with lower energies. Monochromatisation by diffraction eliminates these problems, but involves a great decrease in intensity. Therefore, monochromatisation is feasible exclusively for systems with high initial intensities, such as linear electron accelerators and synchrotron installations (Mees et al., 2014).

An artefact is a reconstruction defect visible on the image (Cunningham et al., 2000). Their presence in the tomographic image may create complications with respect to data analysis during image processing. Many authors have studied the causes of the computed tomographic artefact and have subsequently described techniques to reduce them (Tarplee and Corps, 2011; Boas and Fleischmann, 2012). Figure 2.19 shows different artefacts found in the computed tomography, such as the beam hardening, the ring, the metal, and the motion.

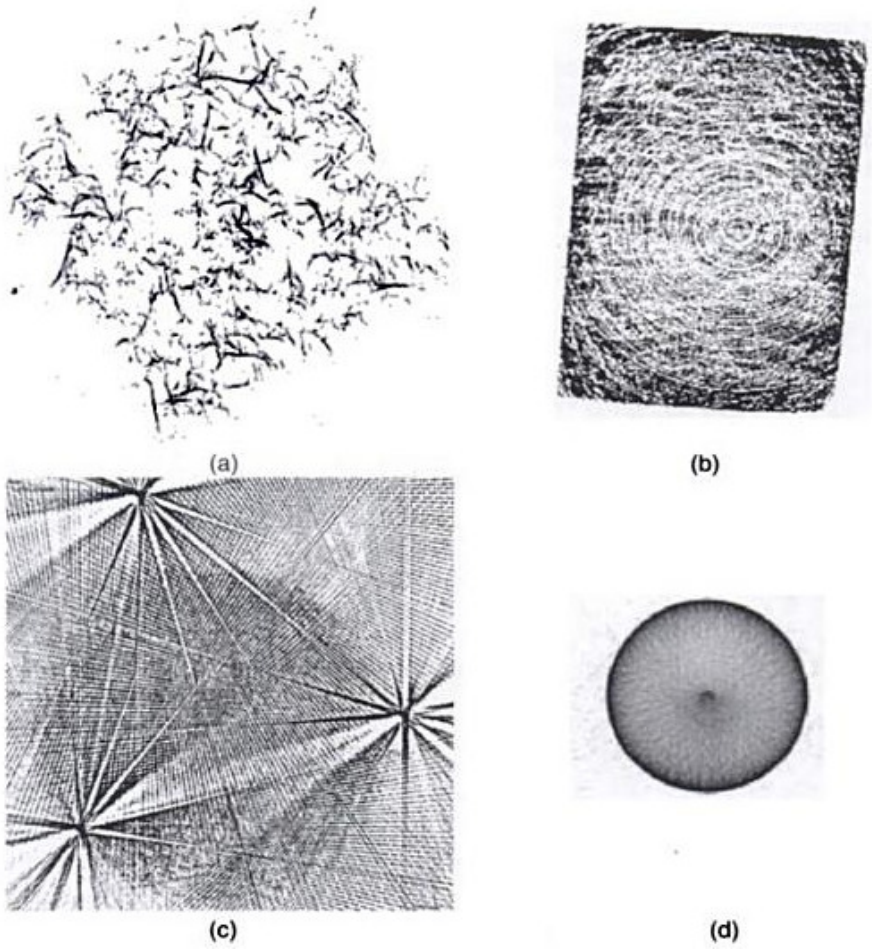

Figure 2.19: Common artefact present in the Computed Tomography images; a) Motion of the sample during the acquisition time; b) Ring artefacts; c) Metal artefact; d) Beam hardening artefact (Clarke and Eberhardt, 2000).

Motion artefact: Perturbations and small lateral displacements give rise to the motion artefact, as demonstrated in Figure 2.19, e.g. the drying (Allisy-Roberts and Williams, 2008).

Ring artefact: The ring artefact is caused by a miscalibrated detector element. The effect may be manifest by several concentric around the axis of rotation (Allisy-Roberts and Williams, 2008).

Beam hardening artefact: The beam hardening artefact results from the polychromatic nature of the X-Ray beam. As the beam passes through the material, it becomes harder. Its mean energy increases because the lower energy photons are absorbed more rapidly than the higher energy photon (Cunningham et al., 2000; Allisy-Roberts and Williams, 2008).

Metal artefact: The presence of a metal object can cause streaking artefact. De Man et al. (1999) investigated which of these causes are relevant to metal streak artefacts with modern CT-scanners. It was determined that beam hardening, scatter, noise and exponential edge-gradient effect are identified as important factors of metal streak artefacts.

In addition, noise is also an artefact, as it limits to the quality of CT image. Contrast between material and air is reduced. Noise increases with increasing spatial resolution (Allisy-Roberts and Williams, 2008).

2.4.5 Advantage and limitations of the technique

XRCT has advantages and limitations, as listed in Table 2.2.

Table 2.2: Strength and limitations of the XRCT technique.

Strengths	Limitations
• Non-destructive. • Samples can be observed in the natural state, which means no sample preparation. • Spatial resolution of 0.8 µm • Provides 2-D images in a form that can be reconstructed to create realistic 3-D images. • Non-invasive 2-D and 3-D calculation of internal microstructural parameters.	• High resolution requires small objects. • Finite resolution causes some blurring of material boundaries. • Polychromatic X-rays. • Image artefacts can complicate data acquisition and interpretation. • This technique is based on the density difference. Therefore, it cannot differentiate based on chemical structure.

The ideal CT system should waste no information related to absorption, scattering, diffraction, energy, time of flight, prior information, and so on (Wang et al., 2008). Reduction of image artefacts has been a central topic in the CT field (Barret and Keat, 2004). Image quality can essentially be summarized by four main performance characteristics. First, high-contrast image resolution (spatial resolution) is the ability to distinguish high-contrast features. Second, low-contrast image resolution (contrast resolution) measures the ability to differentiate a low-contrast feature from its background. Image noise imposes a grainy appearance due to fluctuations of the X-ray photon flux. Third, temporal resolution determines the ability to capture structures in motion. Fourth, quantitative accuracy is desired to relate the image pixel values to physically meaningful quantities in the absolute sense, which is particularly important in dual/multi-energy Computed Tomography. Image artefacts are structured interferences of any type and clearly need to be minimized at all times,

however, quantification is difficult. Thus, XRCT research and development is required to improve image quality (Wang et al., 2008).

2.4.6 Applications of the X-Ray micro-Computed Tomography

FIB-SEM serial-section imaging remains a popular 3-D technique for catalyst characterisation, partially due to its greater accessibility (Datye, 2002). Comparable imaging volumes, spatial resolution, and elemental sensitivity are typically obtained using FIB-SEM and XRCT methods, but the XRCT has been employed in this work due to its non-destructive nature as well its developing in-situ imaging capabilities. Recently, X-ray micro-Computed Tomography has emerged as being an effective technique for visualising internal structure of materials. X-ray micro-Computed Tomography may be used without limitation with respect to visualising the complexities of internal and external surfaces. This non-destructive method allows ex-situ sample treatment as well as future analysis with complimentary techniques, as it will be demonstrated in the study of cracks development before and after calcination.

X-ray micro-Computed Tomography has been successfully used in previous studies to characterise pore structure in a range of different materials including bioactive glass foams for tissue engineering scaffolds (Atwood et al., 2004), biodegradable polymers (Müller et al., 2002), and paper (Antoine et al., 2002). XRCT was also used to examine the properties of powder compacts such as the density distribution (Sinka et al., 2004; Phillips and Lannutti, 1997; Burch, 2002), the internal porosity distribution of granules (Farber et al., 2003), and crack and fracture patterns inside the tablets (Wu et al., 2005; Wu et al., 2008).

2.4.6.1 Study of density variation

To investigate density distributions, the use of XRCT within materials has potential importance in a number of industries, such as pharmaceuticals and catalysis. Density distributions within roller compacted granules were investigated in order to help the optimisation of manufacturing efficiency and the quality of products (Miguélez-Morán et al., 2009). Pharmaceutical tablets were also investigated with the objective of optimising the die compaction process in order to improve physical and mechanical properties of the product (Sinka et al*.,* 2004). Local density change of alumina powder during compaction was studied (Kong and Lannutti, 2000). Density and mechanical properties have also been investigated for carbon-carbon composites (Douarche et al*.,* 2001) and metallic powder compacts (Burch, 2002). Studies of density for porous catalyst supports can lead to an understanding of processes such as sintering during production (Lu et al., 2000; Li et al., 2009). The variation of intensity allows the visualisation of the metal profile resulting from the impregnation process (Grunwaldt et al., 2009; Rigby et al., 2011).

2.4.6.2 Characterisation of pore network

X-ray computed tomography has been utilised in the visualisation of pore structures, 3-D reconstruction and the quantification of macro-pores using both X-ray and image analysis (Pierret et al., 2002). Applications have included the estimation of porosity of rocks (Taud et al., 2005), the study of the porosity and morphology of granules (Farber et al., 2003), the combination of this technique with the computer simulation for analysis of granular and porous material (Moreno et al., 2010), and study of the entrapment of non-wetting fluids within nano-porous media (Rigby et al., 2006). Over the last few years, the importance of

image processing analysis with X-ray computed tomography technique was shown, especially when the main limitation of pore characterisation is the resolution. For instance, the image processing could be used to see the interconnectivity of pores (Atwood et al., 2004).

In the field of catalysts, the XRCT was often used as a complementary technique to the mercury porosimetry and the scanning electron microscopy, providing information on the macroscale and showing regions with different porosities. These may be important in determining mass transport properties and mechanical strength. The XRCT was used in combination with mercury porosimetry to investigate pore size distributions and pore connectivity in catalytic supports, such as in solid-gel silica (Rigby et al., 2006; Rigby et al. 2008) and platinum-alumina (Rigby et al., 2011). XRCT is used in a complementary method to provide the spatial distribution of pore networks within its resolution. The density distribution of a porous solid is directly linked its pore size distribution (Phillips and Lannutti, 1997). The use of XRCT and mercury porosimetry has a great potential in density distribution studies of porous catalyst supports. Both techniques overcome the limitations of the other ones (Rigby et al., 2011).

2.5 Synchrotron tomography

Synchrotron X-ray tomography is a non-destructive technique which can visualise the 3-D interior structure of material and with a high spatial resolution (Donath, 2007). The microstructural analysis of different materials can be analysed with the tomographic system. The high intensity of the original source is important, and it provides images with a high signal to noise ratio in a short time. Consequently, it was possible to conduct radiography scans readily. The variation of radiation energy enables the investigation of objects with

different absorption coefficients. In addition, the high beam coherence for phase contrast imaging provides a better image contrast (Cloetens et al., 1997).

2.5.1 Principle of synchrotron

The process begins with an electron gun that emits a beam of electrons into a straight tube which accelerates the electrons before sending them into the circular booster synchrotron. In this circular chamber, the electrons are accelerated and subsequently acquire energy. Then, they enter into a larger circular chamber where they further accelerate to relativistic speeds, within close proximity to the speed of light. Straight tubes called beamlines extend outward from the accelerator's largest chamber. As the electrons move through the accelerator at high speed, some break off and travel down the beamlines. The light coming through the beamlines can then be used for a variety of purposes, including examining objects on the atomic level.

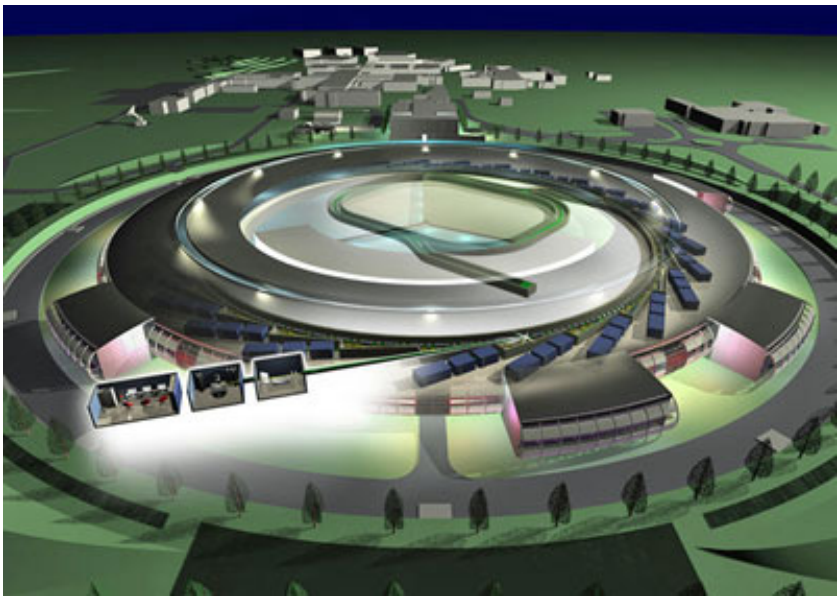

Figure 2.20: Scheme of the synchrotron facility.

2.5.2 Comparison between XRCT and synchrotron X-ray Tomography

As described in Chapter 2.4.4, quality of CT images are limited by artefacts and noise. Two of the main reasons are associated with the polychromatic nature of the X-ray source (Kastner et al., 2010). Those limits are particularly pronounced with metals or materials of high density. The significant advantages of the synchrotron radiation are the parallel X-ray beam and the monochromatic spectrum.

Kastner et al. (2010) were comparing different features collected from XRCT with the Synchrotron tomography, in terms of beam-hardening, detection of details, sharpness, contrast, signal-to-noise ratio and the grey value histogram. They demonstrate that the use of a synchrotron provides significant advantages by decreasing artefacts on the tomographic images and simultaneously improving contrast and resolution.

2.5.3 Applications

The synchrotron could provide an understanding on dynamic phenomena which is not achievable with conventional techniques (Baruchel et al., 2006).

The higher resolution of tomography synchrotron method is a crucial advantage in order to have the possibility to visualise and to follow the development of cracks (Toda et al., 2004; Buffiere et al., 2006; Zhang et al., 2009). Many works were done on the study of crack initiation and growth in different research fields, such as in cast magnesium alloy (King et al., 2011) and in metal (Buffiere et al., 2006). The dynamic of the structure drying front in a porous media was also studied (Shokri et al., 2012). Rufino et al. (2005) reported that the use of a combination of X-ray microtomography, in conjunction with mercury porosimetry and Low Melting Point Alloy (LMPA) intrusion potentially provides a more holistic approach to

more accurate alumina catalyst pore structure characterisation and modelling. The data collected from the study were used to develop and generate an improved pore network model basis, in which both heterogeneity and hierarchy are considered in obtaining an improved pore architecture and pore size distribution.

2.6 Image analysis

2.6. 1 Description of image

Images are represented in a computer by a horizontal grid, or array of very small regions known as picture elements. Elements are more commonly known as pixels. The position of each pixel in the image can be identified by its coordinates, where the row is denoted (x) and the column is denoted (y). It is conventional to have the reference point from the upper-left position of the bitmap, which is considered position (0, 0) that is (row 0, column 0).

As mentioned earlier, X-ray images are generated by the differences in X-ray attenuation, which in turn is linked to density variation (Mousavi et al., 2005). Density differences are displayed as bright or dark values. Therefore, an image is representing, by varying shades of grey assigned to each pixel, the variation of density within the sample

The pixel depth is the number of bits used to represent a pixel value in an image. Depending on the capability of the computed tomography, 1-32 bit greyscale range could be used. It is a commonplace to use an 8-bit greyscale range. In 8-bit greyscale images, a pixel with a value of zero is completely black and a pixel with a value of 255 is white.

2.6.2 Image processing

Tomographic images might require some type of enhancement. Therefore, the ability to extract and to interpret data from images would be possible. Noise and artefacts are frequent in those tomographic images, which introduces difficulties to distinguish objects, i.e. pores and cracks. In order to distinguish between empty space and material, a segmentation is undertaken (Le Trong et al., 2008). However, it was necessary to carryout image enhancement prior to the segmentation.

2.6.2.1 Image enhancement techniques

Image enhancement can be carried out using powerful colour and contrast filters, including Fast Fourier Transforms (FFT), morphology, field flattening, background subtraction and other spatial and geometric operations. Other features include the ability to calibrate the spatial scale to any unit of measure, tracing and counting objects manually or automatically, and measuring objects' attributes.

Those different enhancement techniques are split into three main groups, which are:

Intensity Index Modification: Intensity modification is mostly referring to the change of brightness and contrast.

Spatial Filter Application: Images often contain hard edges, which are regions in which abrupt changes in intensity occur. Soft edges or areas in which there are gradual changes also exist. Application of a spatial filter will detect and modify the intensity transitions at these edges by making a soft edge appear sharper, or making a hard edge smoother.

2.6.2.2 CT Segmentation

Segmentation of a tomographic image is a trivial process. Segmentation is defined as the process of partitioning grey-level voxels of the 3D image into distinct objects (Le Trong et al., 2008). In the context of catalyst support, it is to separate the void area from the solid structure of the support. Segmentation is complicated by the presence of noise and blur. Noise is characterised by the presence of voxels with the same grey value of the structure of the sample, while blur is characterised by a non-well defined border between 2 phases (Le Trong et al., 2008). 3-D images are not suitable to a manual analysis, because of the important number of images collected. Therefore, the use of image processing software allows for the automatic segmentation by several techniques. The three principle techniques are reported in the literature: Segmentation by thresholding grey levels histogram, segmentation by active contours and segmentation by watershed-based techniques.

Segmentation by thresholding grey level histogram: That segmentation could be carried out with (Kaestner et al., 2006) or without (Appoloni et al., 2007) a former filtering. The threshold might be done automatically (Sezgin and Sankur, 2004) or not (Appoloni et al., 2007). Sometimes, the thresholded images need to have a binary post treatment (Erdogan et al., 2006; Kaestner et al., 2006).

Active contours on the image (Ramlau and Ring, 2007). That segmentation technique is used in medical applications and requires the knowledge of the location of the interfaces.

Watershed-based techniques (Beucher and Lantuejoul, 1979; Vachier and Meyer, 2005; Videla et al., 2007). That technique allows the extraction of individually objects.

2.6.2.3 Image Histograms

Image histograms measures and illustrate the brightness and contrast characteristics of an image in terms of brightness and contrast (Le Trong et al., 2008). The x-axis represents intensity values (from 0 to 255 for 8-bit images) and the y-axis measures the number of pixels in the image having a specific intensity.

Segmentation could be carried out based on the grey value histogram with the aim of obtaining a binary image (Le Trong et al., 2008) prior to starting the analysis.

2.6.3 Analyses of morphometric parameters

After the segmentation, morphometric parameters are calculated either in 3-D based on a volume model, or in 2-D from cross-sectional images. The parameters obtained from image processing software are:

Total volume of the volume-of-interest (VOI): It is measured in both 2-D and 3-D.

Object volume: It represents the total volume of binarised objects within the VOI and could be measured in both 2-D and 3-D.

Percentage volume: It is the proportion of the VOI occupied by binarised solid objects.

Object surface: In 2-D, the binarised object surface includes the cross-sectional slice perimeter measurements and the vertical surfaces between solid and space

Structure thickness: The calculation of the structure thickness is mostly based on an estimation, as it requires an assumption about the nature of the structure. Three simple

structure models, the parallel plate, the cylinder rod and the sphere model, provide the range of values within which a hypothetical "true" thickness will be located (Parfitt et al. 1987).

Structure separation: Refers essentially to the thickness of the spaces as defined by binarisation within the VOI.

Porosity: Binarised objects are identified containing fully enclosed spaces, and porosity is the area of those spaces as a percent of the total area of binarised objects.

2.7 Conclusion

Chapter 2 has provided an overview of the preparation of heterogeneous catalysts, and introduced the impact of processing parameters and formulation on the control of porosity. Secondly, different methods widely used for the structure characterisation in catalyst area have been discussed. Finally, a description of a non-destructive technique, the X-Ray micro-Computed Tomography technique, has been presented. The X-Ray micro-Computed Tomography section provided an overview of the technique with its advantages and its disadvantages. Moreover, an introduction into the underlying physics associated with the XRCT is given in order to understand the image processing and the interpretation of results.

CHAPTER 3 – MATERIALS AND METHODS

3.1 Introduction

As discussed in Chapter 2, imaging techniques are widely used to characterise the catalyst structure. Porosity and surface area, as well as the detection of the mechanical defaults, are the most important physical parameter that determine the performance of catalysts. The porous structure is characterised by a variety of parameters, such as the void fraction called porosity, the pore size distribution, the specific surface area, the pore network and the connectivity (Rigby and Daut, 2002). The pore structure has been characterised by both traditional methods and visualising techniques (Tariq et al., 2011a).

X-Ray micro-Computed Tomography (XRCT) allows visualisation and characterisation of three-dimensional object structures without special sample preparation or chemical fixation (Mousavi et al., 2005). XRCT has the advantage of being a non-destructive and non-contact inspection technique, which is not limited by the complexity of internal and external surfaces of the tested material (Phillips and Lannutti, 1997; Burch, 2002).

XRCT has been successfully used in previous studies to characterise pore structure in a range of different materials including bioactive glass foams for tissue engineering scaffolds (Atwood et al., 2004), biodegradable polymers (Müller et al., 2002), charcoal (Bird et al.,

2008) and paper (Antoine et al., 2002). XRCT has also been successfully combined with mercury porosimetry for studying geological rock porosity and connectivity (Hellmuth et al., 1999) and sol-gel silica spheres (Rigby et al., 2006; Rigby et al., 2008).

The current chapter describes the materials used and the experimental procedures conducted to characterise the structure of the heterogeneous catalyst support.

3.2 Materials

Two different phenomena were investigated in this work:

- Development of cracks under different processing conditions;
- Spatial metal distribution after impregnation.

3.2.1 Samples preparation for XRCT

Paste preparation and Drying. Experiments were carried out by mixing a boehmite powder with nitric acid (1%), which causes the peptisation of the gel and then the gel is reformed in a more dispersed and suspended form resulting in a paste. Four pastes with various water contents were mixed in the Werner and Pfleiderer Z-Blader mixer for 2 hours. Soustruznik et al. (1968) reported that the moisture of an ideal paste should lie in the range of 50-53%. The objective of the current work is the examination of cracks, therefore their presence needs to be ensured. Thus, the range of moisture content chosen to be analysed was between 48-51% (0.92-1.04 kg water.kg solid^{-1}) that would possibly lead to cracks. After the time length of 2 hours, the paste was transferred into a plastic bag to prevent water from vaporisation, and when required was extruded using a ram speed of 10 mm.min^{-1} and 50 mm.min^{-1},

corresponding to the slowest and fastest setting permissible by the ram extrusion apparatus; the die used was of a 5 mm diameter. A scheme of the ram extrusion apparatus is illustrated in Figure 2.4. The extrudate was then collected and half of it was dried at room temperature (approx. 20°C) overnight, while the other half was dried in a fluidised bed dryer at 105°C for 20 min. The experimental plan is shown in Figure 3.1

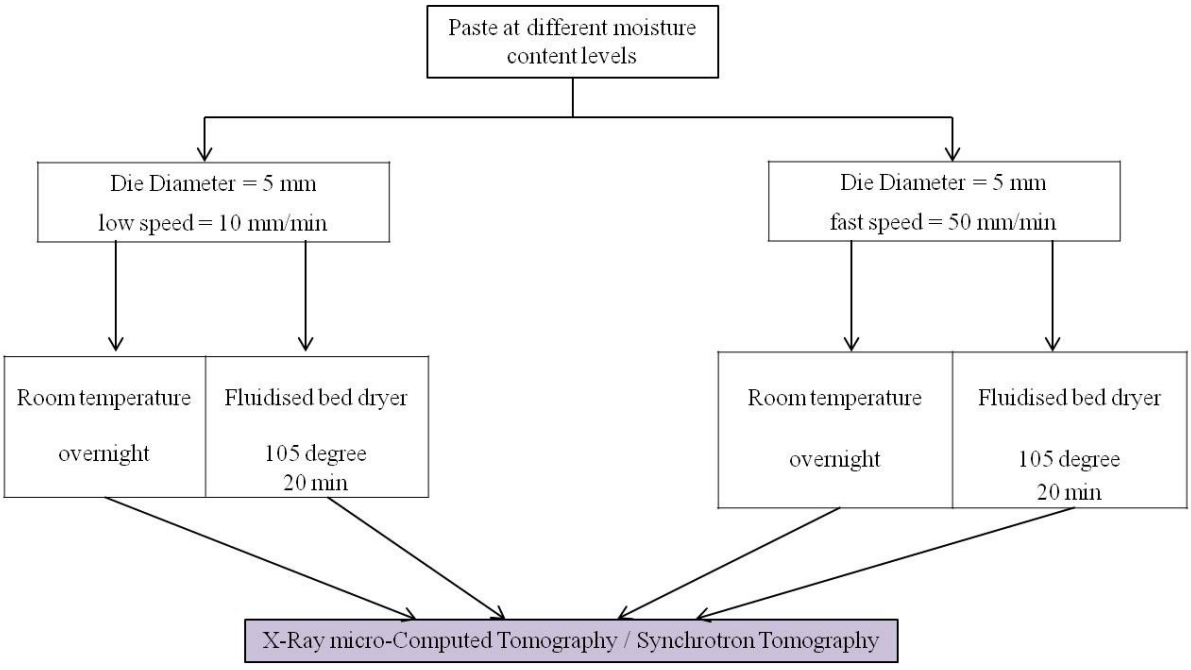

Figure 3.1: Experimental plan used for studying the development of cracks.

Calcination. A piece of the above dried paste sample was cut (10 mm length and 5 mm diameter) and calcined at 550°C in a furnace oven for 4 hours. The sample was then scanned and was compared to the initial dried samples.

Wet Impregnation. The calcined samples were dipped into copper nitrate trihydrate ($Cu(NO_3)_2$, $3H_2O$) saturated solutions of 5 % and 90 % (w/w), with a 0.3 $mol.l^{-1}$ and 5.1

$mol.l^{-1}$ concentration, respectively. The samples were then removed at different time intervals, excess of moisture was removed and further analysis was conducted.

3.2.2 Samples preparation for the synchrotron

The sample preparation is the same as in Chapter 3.2.1. The samples were stored in an air tight container for maintaining the moisture content constant, before they were analysed in the synchrotron.

As far as the impregnation step is concerned, the extrudates with the minimum number of cracks were selected, as the diffusion of the solution in the porous media (extrudate) is more evident.

3.3 Methods

3.3.1 X-Ray micro-computed Tomography

3.3.1.1 Devices

In this work, two different X-Ray micro-Computed Tomography (XRCT) devices were used: Skyscan 1072 and Skyscan 1172, having a resolution of 2 µm and 0.8 µm respectively. Figure 3.2 shows a photograph of Skyscan 1072 desktop micro-Computed Tomography system located in the department of Chemical Engineering in Birmingham (UK).

Figure 3.2: Photograph of the Skyscan 1072 desktop micro-Computed Tomography system.

Preliminary experiments were carried out on the Skyscan 1072 device. The change of the X-ray tomographic device during the project was due to an irrecoverable damage of the X-ray tube. All computed tomographic images presented in the results chapters were produced using the Skyscan 1172 desktop micro-Computed Tomography system, located at the Dental School in Birmingham (UK).

All experiments were conducted in the Skyscan 1172 system. The high resolution Skyscan 1172 desktop micro-CT system consists of a microfocus sealed X-ray tube with a spot size of 5 µm. The X-ray source operates between 20-100 kV. The X-ray detector consisted of a 1024x1024 pixel 12-bit digital cooled CCD camera connected to a computer. The maximum sample (object) size allowed to be used in the X-ray device is of approximately 27 mm diameter for a single scan and 50 mm diameter for an offset scan.

3.3.1.2 Scan to image

As mentioned in Chapter 2, scanning is consisted of two steps: data collection and image reconstruction. Figure 3.3 shows a flowchart of the scanning process highlighting the three most significant stages used to obtain a 3-D rendering from a scan.

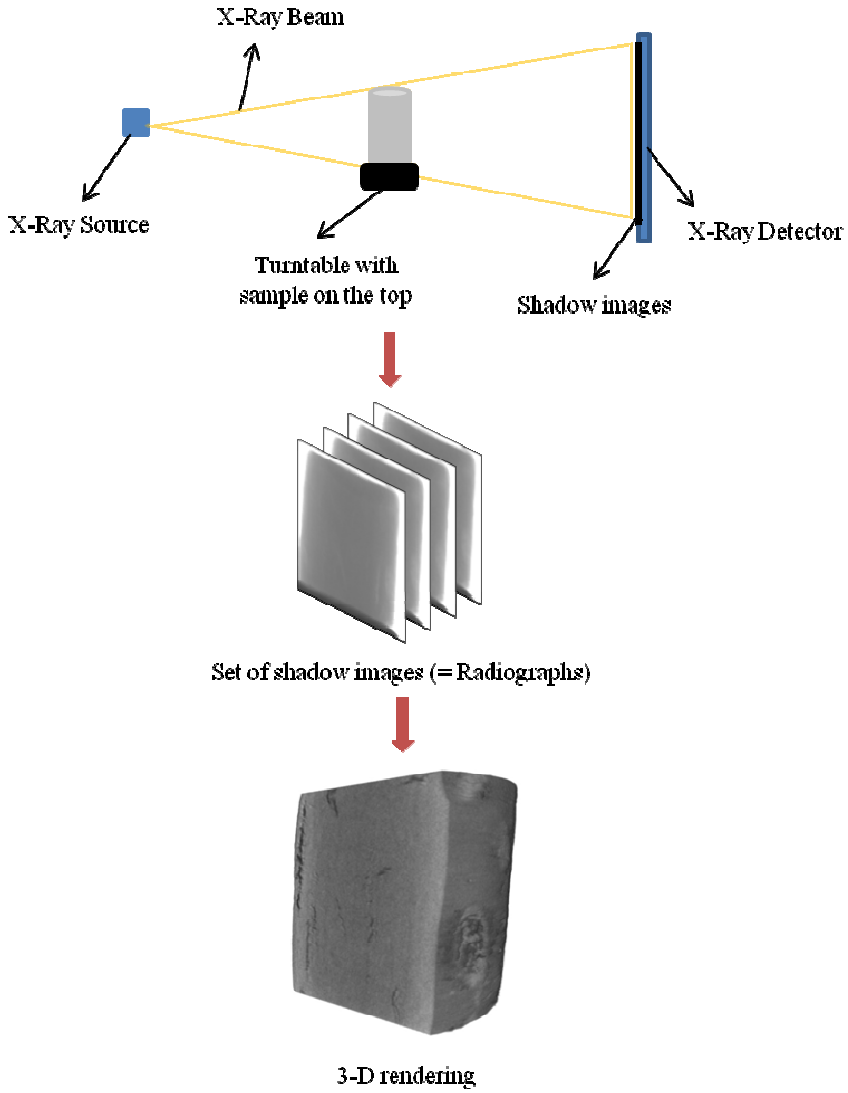

Figure 3.3: Flowchart of scanning process from the data collection to image reconstruction.

The three stages correspond to: (A) acquisition; (B) reconstruction and (C) 3-D rendering. In each stage, different software provided by Skyscan were used, such as Control software for Skyscan 1172 for the acquisition, N-Recon for the reconstruction, CT analyser for the image processing and data analysis, CT volume for the 3-D model and CT Vox for 3-D visualisation of the sample from cross sectional images.

3.3.1.3 Acquisition

The sample is installed on a turntable in the middle of the chamber. During the acquisition, X-rays are passed through the object which is rotated inside the X-ray chamber so it can be viewed at different angles. A computer records each of the projected images and measures the intensity of the X-ray beam as it passes through the object material.

The software 'Control software for Skyscan 1172' is used to set experimental parameters and to acquire projected images, making it possible to control device's parameters, such as the selection of filters, voltage, current, adjustment of the sample position inside the chamber, camera, pixel size, exposure time, rotation step, averaging of frames per rotation and random movement. Those steps are the most important ones for the setting of the machine. The list of parameters is presented in the order they are carried out. Each input parameter has specific function for the scanning process:

- The voltage and the current were set according to the density of the object analysed. A high voltage application (100 kV) is required for dense objects, such as stones, but not for the catalyst samples.

- The position of the sample and the pixel size is set in order to make the sample visible in the displayed screen.
- The averaging of frames allows the improvement of the image quality by averaging several images in every angular position.
- The random movement of the object, given in a number of lines on the camera, can reduce the ring artefacts in the reconstructed cross sections, but it increases the scanning time. Several scans with different values of random movement were carried out until the minimum number of ring artefacts was achieved.
- After the parameters were set the scan was started and a set of projected images (= shadow images) was collected, and used for image reconstruction.

3.3.1.4 Reconstruction

The reconstruction algorithm is based on a filtered back projection procedure for fan-beam geometry with specific noise reduction corrections (Skyscan, 2003b). The principle of the algorithm is briefly explained in Chapter 2.4.3.2.

A set of shadow images is collected and uploaded to the reconstruction software provided by Skyscan. Figure 3.4 shows the configuration of the software displayed on the monitor.

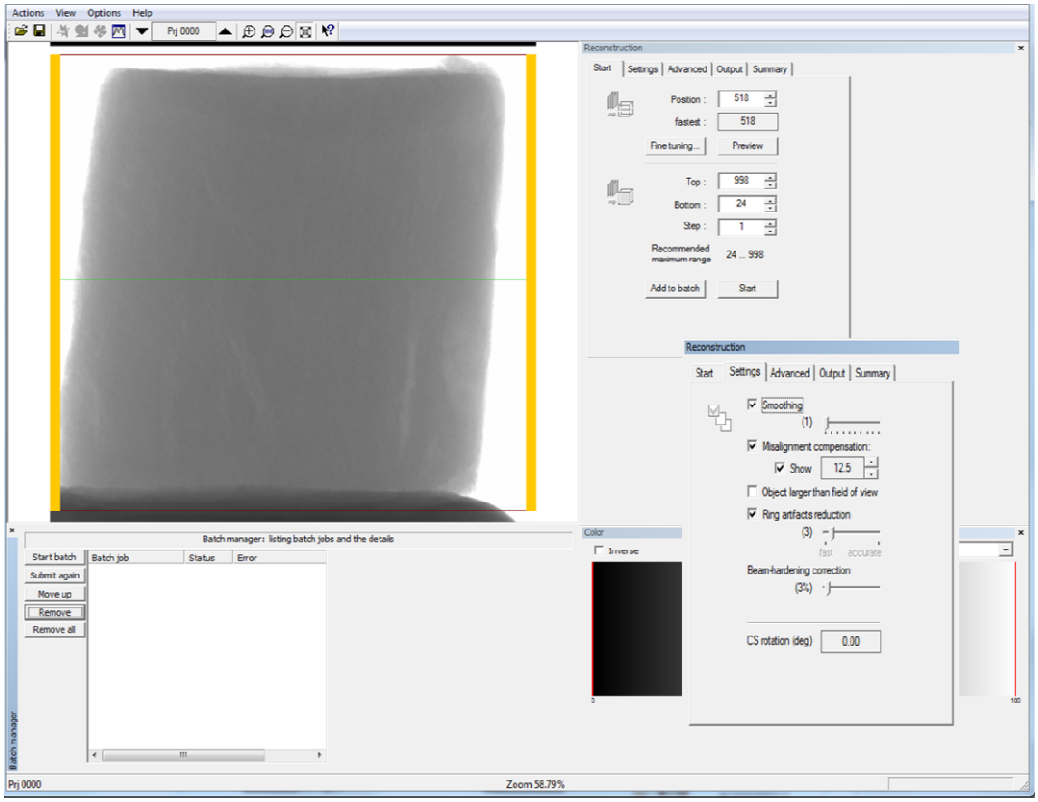

Figure 3.4: Configuration of the reconstruction software (N-Recon version 1.6.4.1) provided by Skyscan.

In Figure 3.4, projected images of an alumina extrudate are taken as an example. When uploading a dataset, the default value of different parameters is automatically displayed. Those parameters include smoothing, misalignment compensation, ring artefact reduction, beam hardening correction, cross sectional rotation (CS rotation).

- Smoothing: It is used to reduce the noise, but may also introduce blurring for thinner structure. The smoothing level lies between 1 and 10.
- Misalignment compensation: It is a key parameter in indicating image quality. Wrong alignment can introduce doubling or blurring in reconstructed images.

- Ring artefact reduction: It is applied to the shadow images before the processing steps of reconstruction and image analysis. A correction parameter with values between 1 and 20 is used in order to reduce the artefacts to minimum.
- Beam hardening correction: The compensation of the beam hardening effect is done by a linear transformation in the software. The value of correction factor, which lies between 1 and 100, is selected according to the material's density.
- CS rotation: This factor rotates the cross sectional image from a fixed angle.

Adjustments of the above parameters are subjective. A number of trials were conducted in order to ascertain the effect of each parameter on the image quality. The correction tools provided by the software are useful in the reduction of the artefacts but can also alter the original image, by introducing incorrect data. The images resulting from the acquisition and the reconstruction steps should be identical to the initial object.

3.3.2 Setting of the X-ray Computed Tomography

A number of setting have to be optimised to achieve the best overall scan quality. As mentioned in Chapter 2.4.4, the main disadvantage of tomographic images is the presence of artefacts and noise, which could significantly affect the image quality and the analysis. Another drawback of the technique is that the acquisition and reconstruction steps can be time consuming depending on the size of the sample and the parameters applied, which are the following:

- The sample diameter: lies between 3 and 5 cm.

- The pixel size: lies between 0.8 and 12 µm.
- The exposure time which is the dependent variable of the sample's absorption level, displayed on the software. After different trials, it appears that the percentage of that absorption should be above 60% to get a good contrast, which would clearly differentiate the sample from the air. Therefore, the exposure time was defined based on the percentage of the absorption of the sample.

Once the exposure time was set, a combination of steps was implicated in order to achieve reduction in acquisition time by maintaining high image quality. The different steps involved are described in the following paragraphs.

3.3.2.1 Effect of the filter

A filter is a flat piece of attenuating material used to filter out the energy component before it passes through the material. The Skyscan 1172 device has two different types of filter, an aluminium and an aluminium/copper one with a thickness of 0.5 mm and 1 mm, respectively. An alumina tablet was taken and scanned at a voltage of 50 kV and a current of 98 µA. The scan was done without a filter and with 0.5 mm aluminium filter. Cross sectional images resulting from the experiments are shown in Figure 3.5.

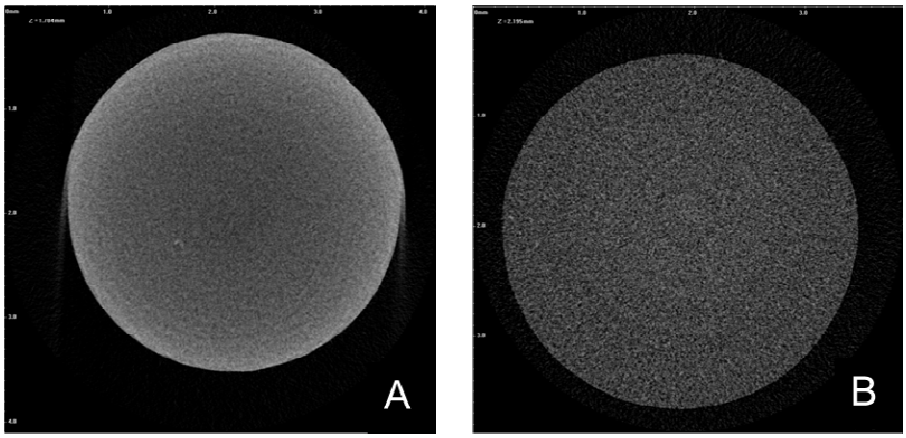

Figure 3.5: Reconstructed images of the alumina tablet. A: without applying filter; B: with 0.5 mm aluminium filter.

Figure 3.5 shows the effect of the aluminium filter on the density of the tablet, based on the difference of the intensity gradient. The high density layer appearing around the sample in Figure 3.5 A), is indicative of the beam hardening artefact. The latter disappears by applying the 0.5 mm aluminium filter which can be explained by the filtration of the lower energy photon component, generally absorbed on the surface of the support. In order to check if the filter has a real effect on the beam hardening artefact, additional analysis was performed by plotting the intensity variation against the four different angles. The catalyst appeared to show lower density at the centre as compared to its surface, as illustrated in Figure 3.6.

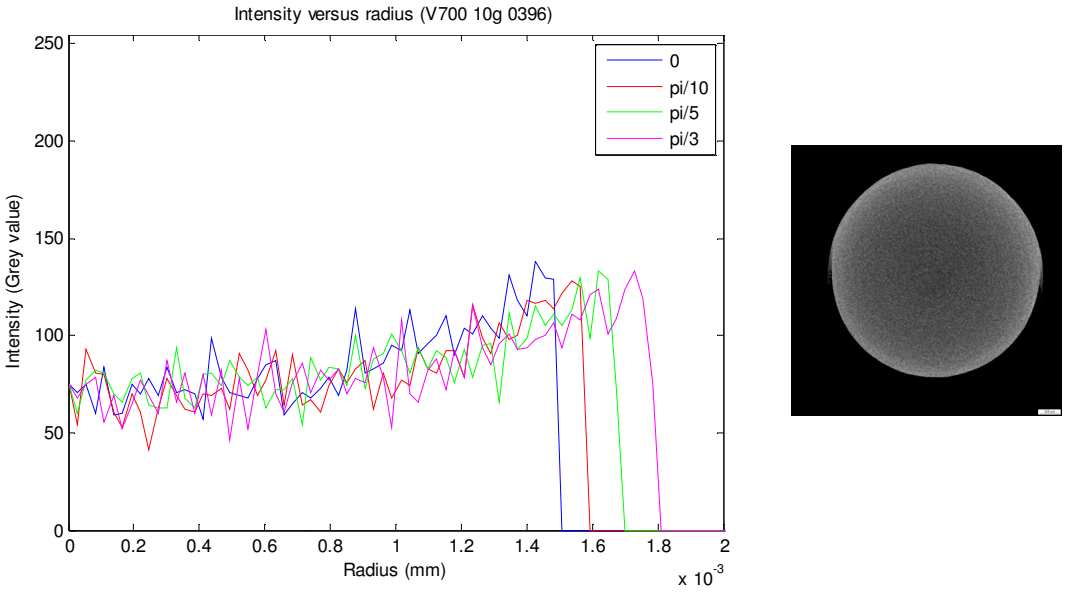

(A)

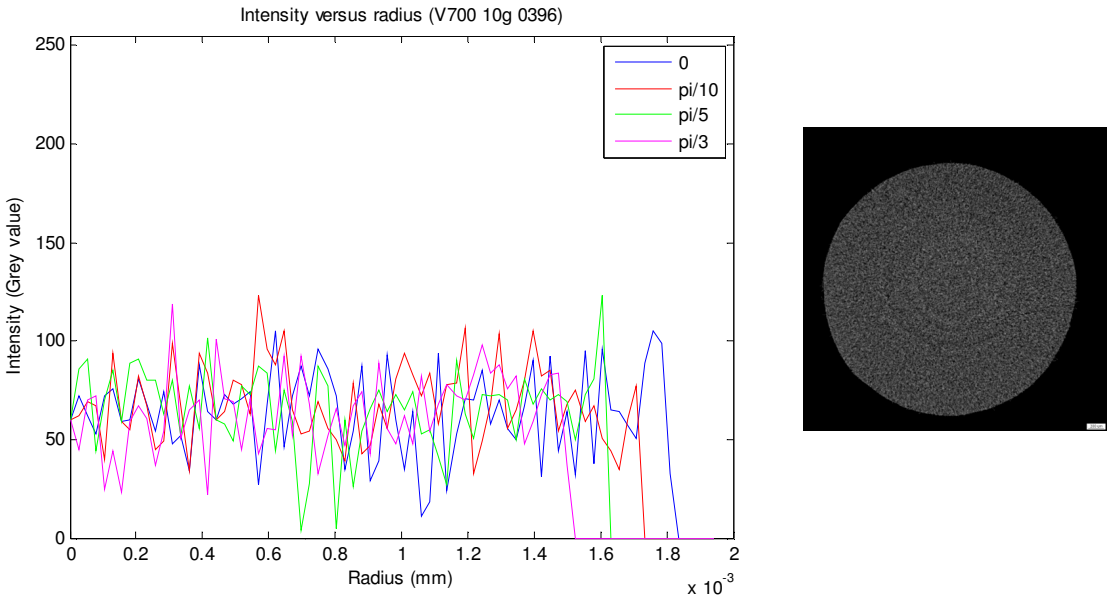

(B)

Figure 3.6: Effect of the filter on the density variation of alumina tablet; (A) Without filter; (B) With 0.5 mm aluminium filter.

The application of the filter reduces the beam hardening artefact by lowering the density of the outer core and by increasing the fluctuation of the density along the radius of the sample.

Another experiment was carried out for confirming the effect of the filter in the beam removal. The same alumina tablet was scanned twice. At first, the full sample was scanned and then it was cut into half prior to scanning, using the same input parameters. The reconstructed images are shown in Figure 3.7.

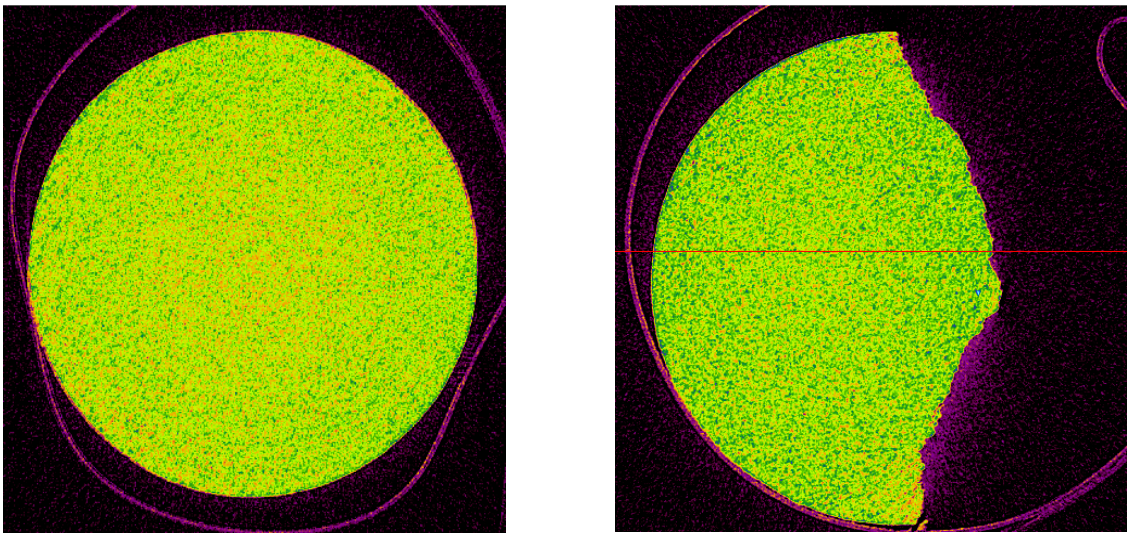

Figure 3.7: Reconstructed images of the alumina tablet by applying 0.5 mm aluminium filter. On the left: full sample; on the right: half-sample.

In both cases, the high density layer could not be visualised on the surface of the support, which represents the real impact of the filter in reducing the beam hardening artefact. Therefore, all further acquisitions were done by applying the 0.5 mm aluminium filter.

3.3.2.2 Effect of the rotation step

During the acquisition step, X-ray images were acquired at different angular positions. The sample was chosen to be rotated within a range of 0^o to 180^o. The acquisition time decreases by increasing the rotation step. However, it was of interest to see how the rotation angle can affect the image quality and so, where the best balance between image quality and acquisition time could be.

Three scans of the same catalyst support were done by changing the rotation step, which included three rotation radius, 0.45^o, 2^o, 5.4^o. The reconstructed cross sectional images of each rotation step are shown in Figure 3.8.

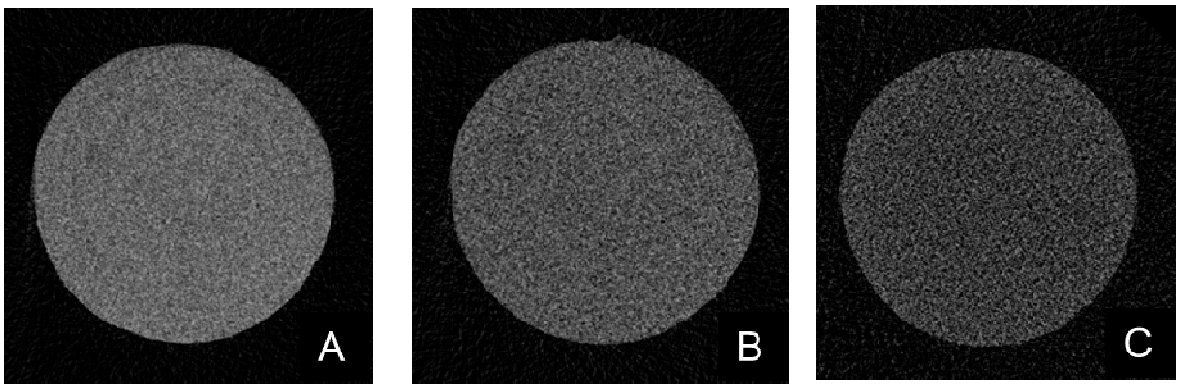

Figure 3.8: Reconstructed cross sectional images of an alumina extrudate support scanned at different rotation steps: A) 0.45 °; B) 2 °; C) 5.4 °.

The results derived, indicate that the standard deviation of the sample is increased with the rotation angle, while the mean grey value is decreased; increasing the angle from 0.45^o to 2^o results in an increase of the standard deviation from 18.87 to 22.64 and a decrease of the mean value from 97.31 to 78.14; increasing the angle from 0.45^o to 5.4^o results in an increase of the standard deviation from 18.87 to 26.6 and a decrease of the mean value from 97.31 to 54.07.

Details on the internal structure are lost with incrementing the rotation step. In addition, the background of the image seems to be noisier when the rotation step increase, which is confirmed by the standard deviation increase. Consequently, the best rotation angle would be the 0.45^{o}, which gives more information on the density variation and pore distribution within the sample. The acquisition time for rotating the sample with an angle of 0.45^{o} is about 35-40 minutes.

3.3.2.3 Effect of the reconstruction

Based on the previous experiment, the device was set at a rotation angle of 0.45^{o} and for each rotation angle one shadow image is taken. At the end of the scanning process, a set of approximately 400 shadow images were uploaded by the reconstruction software (N-Recon) provided by Skyscan. In the software, the selection of images used for the reconstruction was made by using an option called 'cross sectional (CS) rotation'. That option rotates the cross sectional image by a fixed angle (N-Recon manual, 2011). The CS rotation value should be greater than 0. Four trials with four CS values were chosen, 1, 2, 3 and 4. The value of 0 which corresponds to the rotation angle of 0.45^{o}, refers to the fixed, chosen CS and the values of 1, 2, 3 and 4 refer to the 'virtual' rotation angles of 0.9^{o}, 1.8^{o}, 2.7^{o} and 3.6^{o}, respectively. After setting the CS rotation, the reconstruction step starts, which lasts 1h30 under normal conditions (CS rotation = 0). If a CS value of 4 is used, the reconstruction time can be reduced to 15 minutes, as the time decrease with increasing the CS value. Cross sectional images obtained from the respective CS rotation values are shown in Figure 3.9.

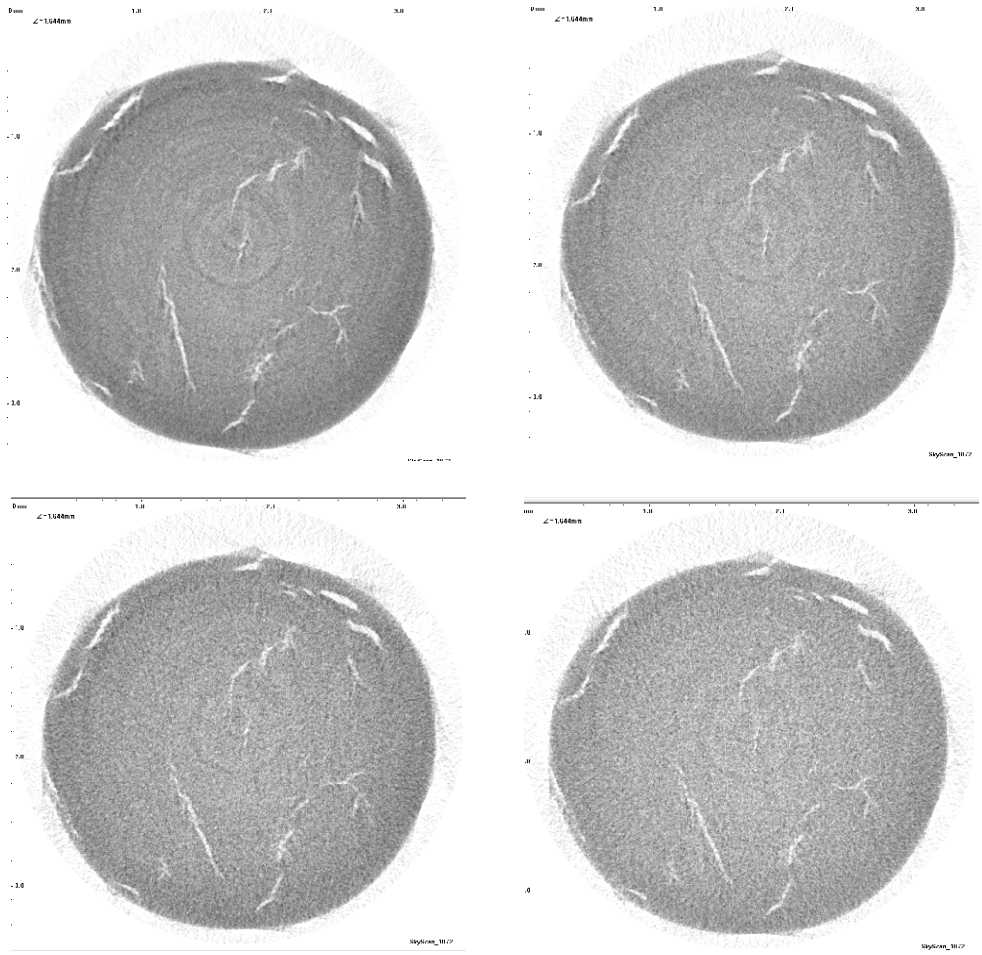

Figure 3.9: Reconstructed cross sectional images from an alumina extrudate support scanned at different CS reconstructed step: A) 1; B) 2; C) 3; D) 4.

As the CS rotation increases, the quality of the image tends to. The contrast between the empty space and the object material is also reduced making the selection of pores and cracks difficult.

Details on the internal structure of the extrudates are lost as the mean grey values decrease and the standard deviations increase when the CS rotation is increased. Figure 3.10 shows the effect of the CS rotation on the mean grey value of the alumina extrudate (A) and on the percentage of voids (B).

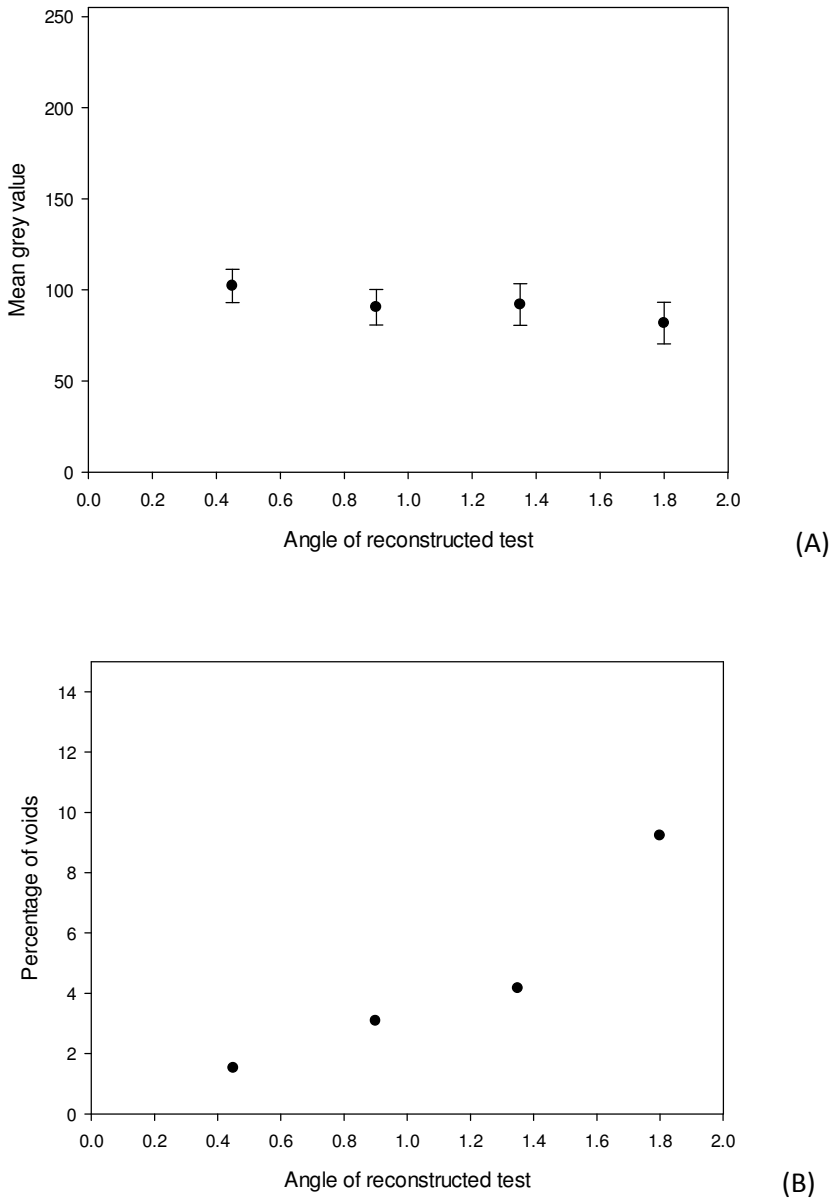

Figure 3.10: A) Effect of the CS rotation on the mean grey value of the alumina extrudate; B) Effect of the CS rotation on the percentage of voids.

There is a small effect of the rotation step on the mean grey value, as shown in Figure 3.10 A). The standard deviation becomes higher when the angle is above 0.9^{o}, which means that the change of angle has an impact on the density distribution. When the CS rotation is increased by a factor of 4, the variation intensity of the internal structure increases

significantly, as the percentage of voids increases by 80% (Figure 3.10 B). In order to analyse the density distribution and the porosity, the CS rotation was set to 0 for the rest of the experiments.

3.3.2.4 Summary

Conclusively, the previous experiments were carried out to adjust a number of parameters in order to find the optimal compromise between the image quality and acquisition/reconstruction time. The setting of the Skyscan 1172 micro-Computed Tomography device is shown in Table 3.1.

Table 3.1: Setting of the Skyscan 1172 micro-Computed Tomography.

Filter	**Voltage**	**Current**
0.5 mm aluminium filter	50 kV	100 µA
Pixel size*	**Exposure time****	**Rotation step**
5-8 µm	500-1500 ms	0.45°
Rotation	**Averaging (frames)**	**Random movement**
180°	3	10

* Depends on the size of the sample.

** Need to be fixed for each scan, as it is related to the power of the X-ray source.

At the end of the acquisition, a set of approximately 400 projected images are obtained. Then, the reconstruction stage could start. Table 3.2 shows the setting of the reconstruction software.

Table 3.2: Setting of the reconstruction software (N-Recon).

Smoothing	**Noise**	**Misalignment compensation**
1	2	Value given by the software
Ring artefact correction	**Beam hardening correction**	**CS rotation**
2-3	2-3	0

At the end of the reconstruction step, a set of ~ 1000 cross sectional images is obtained.

3.3.3 Image processing

Information such as density distribution and porosity, is revealed by using different image analysis software. The majority of the cross sectional images being image processed was carried out by using CT Analyser (CT-An) (ver. 1.13), allowing 2D and 3D analysis of images. CT volume (CT Vol) (ver. 2.0.0.4), which provides the 3D visualisation and Data Viewer (ver. 1.3.2.1) was used. The software are provided by Skyscan. The use of these programs is outlined in the results section of this study. In addition, other imaging software such as Matlab (2007a), ImageJ and Fiji, were used.

3.3.3.1 CT Analyser

3.3.3.1.1 Raw to binary images

A range of cross sections from the dataset were selected and then a region of interest (ROI) or a volume of interest (VOI) was drawn. In this research, the VOI is the whole sample. After drawing the VOI, a threshold of the reconstructed image is required. Figure 3.11 shows an example of a binarisation of one cross sectional image taken from the alumina extrudate.

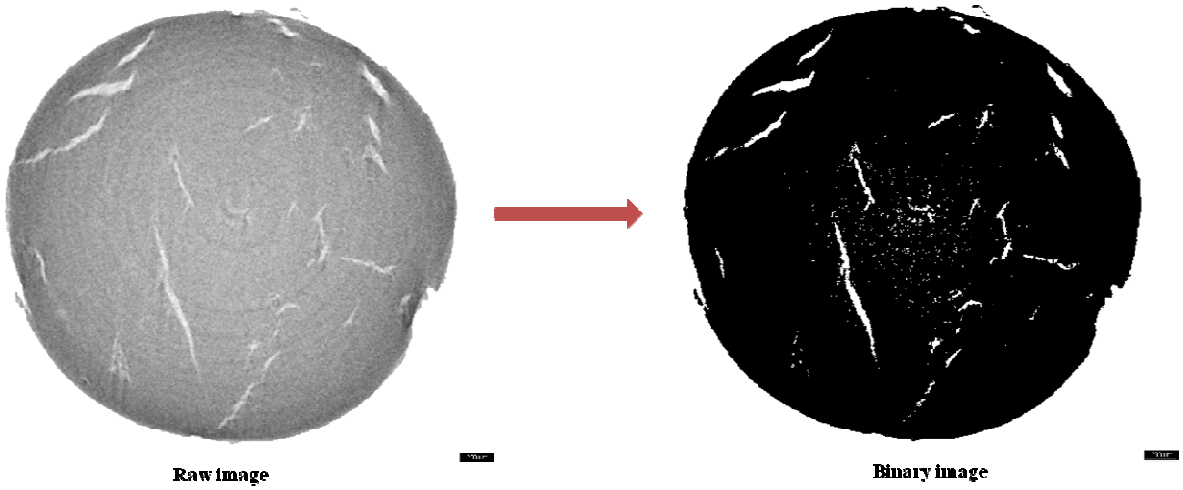

Figure 3.11: Binarisation of a cross sectional image (white = voids defined as being objects; black = structure of the catalyst sample).

The threshold is based on a grey value scale which refers to density and the segmentation of the image depends on the purpose of the analysis. For example, if porosity needs to be studied, only pores need to be selected, or if density needs to be analysed, the entire sample need to be selected. In the binary image, white and black areas represent the voids (pores and

cracks included) and the structure of the catalyst, respectively. Data analysis is usually done on the white region.

3.3.3.1.2 Data analysis

Structural parameters are estimated by using the Skyscan CT-analyser software. Those morphometric parameters were calculated, either in 2-D or in 3-D from raw images. The 3-D analysis is done either for the entire sample or for every individual object. The parameters obtained from the two different kinds of 3-D analysis are listed in Table 3.3.

Table 3.3: Structural parameters from the 3-D analysis and the 3-D individual object analysis.

3-D analysis	3-D individual object analysis
• Total volume • Object volume • Percent object volume • Structure thickness distribution • Structure separation distribution • Open porosity (%)	• Volume and surface area of objects • Volume and surface of pores • Porosity • Structure model index (SMI) • Centroid (x,y,z) of each object

A 3-D model of the catalyst sample is also built using the CT-analyser software and was then visualised with another software called CT-Vol. Parallel to the 2-D and 3-D analyses, density distribution could also be visualised and analysed based on grey value scale.

Additional analysis could have been undertaken using the CT analyser software, for analysing the density profile and for visualising the density distribution in a colour map.

3.3.3.1.3 Summary

Overall, image processing using the CT analyser software needs to follow specific steps, as shown Figure 3.12.

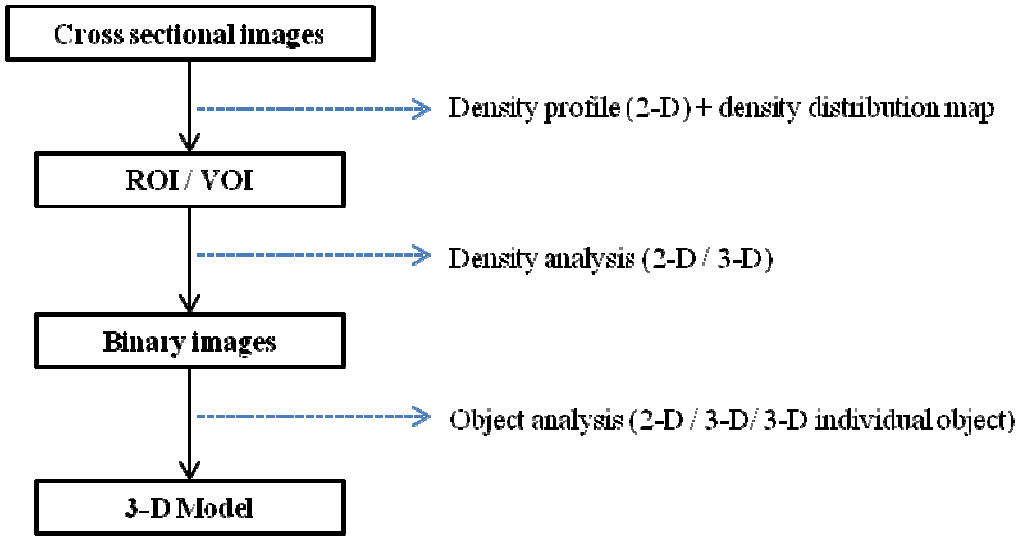

Figure 3.12: Image processing steps by using the CT analyser software.

3.3.3.2 Image J

ImageJ processing software is typically used to visualise the density distribution using a colour map. The lookup table chosen was that of 16 colour bars. Figure 3.13 shows an

example of a cross sectional image of an alumina extrudate and its respective density distribution map.

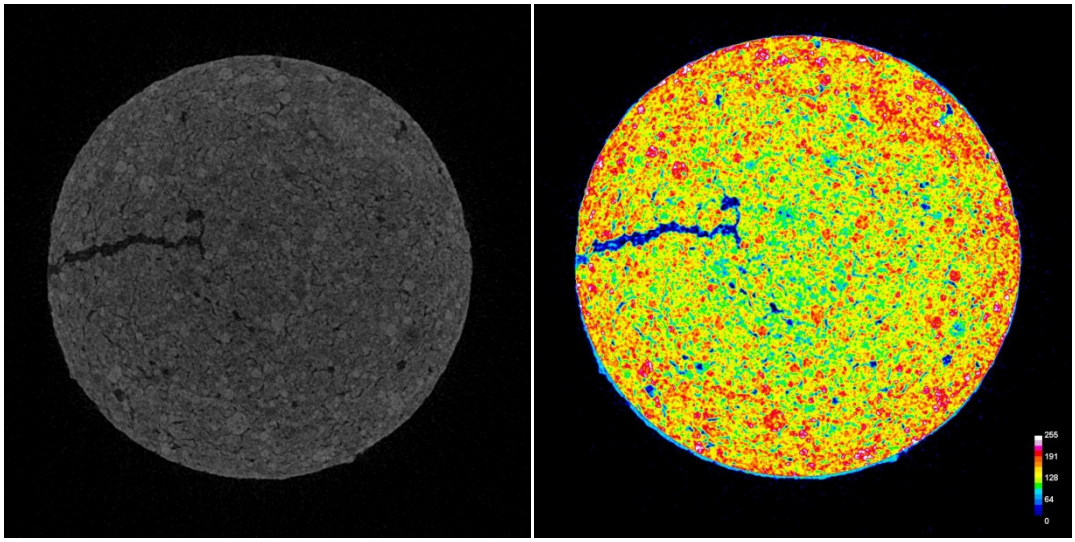

Figure 3.13: Cross sectional image of an alumina extrudate and its respective density distribution map.

3.3.3.3 MATLAB

Image processing toolbox provided by MATLAB is mostly used to further analyse the images, e.g. to understand the pixel intensity at different radii for different processing conditions.

The program reads the original image and a binarisation is applied. The structure of the sample is in white and the inner holes are in black; in order to get the whole sample as being an individual object, those holes are filled. The coordinate point of the centroid of the object can then be located. The intensity variation along a line at 4 different angles (0; $\pi/10$; $\pi/5$ and $\pi/3$) can be plotted. The codes are shown in the appendix A.

3.3.4 The I13 synchrotron beam (DIAMOND)

Micro-tomography is performed using dedicated beamlines at synchrotron facilities; with such techniques, micron-scale resolution is possible within objects at millimetre to sub-millimetre scale (Flannery et al., 1987).

Experiments were carried out at the Diamond Light Source, which is the UK national synchrotron facility, located at the Harwell Science and Innovation Campus in Oxfordshire. At the time of the work the beamline I13 which allowed for X-ray imaging was not fully commissioned. A picture of the system for the beamline I13 is shown in Figure 3.14.

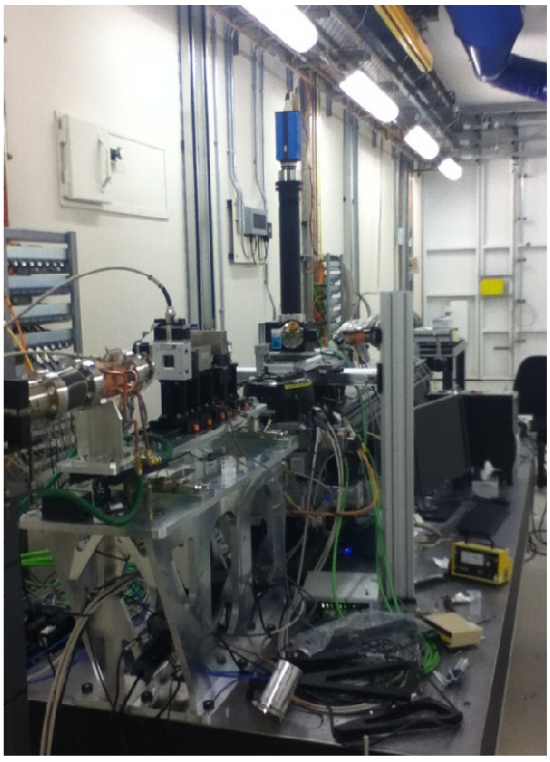

Figure 3.14: Picture of the system for the beamline I13 at Diamond (UK).

This beamline provides a non-destructive examination of internal features ranging from the micro to the nanoscale. This branch line performs in-line phase contrast imaging and tomography over a large field of view in the 6-30 keV energy range. The spatial resolution for this technique is in the micron range.

3.3.4.1 Experiments of the synchrotron

As mentioned previously, radiography and tomography were used for the investigation of two study cases: (i) the dynamic behaviour of the catalyst support under the drying process and the development of cracks; (ii) the visualisation of the impregnation of the metallic solution and its distribution inside the support.

Radiography is one of the oldest non-destructive imaging methods widely used. A small radiation energy penetrates to the solid object, assessing the variation in thickness or in density that represents cracks or other internal imperfections. Therefore, X-Ray images can be used to inspect different kind of materials for defects, to locate internal features and to measure the thickness of the object. The tomography is a non-destructive technique that measures density and porosity distribution within the material. The technique uses a set of 2-D shadow X-ray images of an object to reconstruct its 3-D structure.

The experiments carried out are shown in Table 3.4.

Table 3.4: Experiments performed at the beamline I13 at Diamond.

Study of drying process and development of cracks		**Study of the wet impregnation**	
Radiography	*Tomography*	*Radiography*	*Tomography*
Follow the state of the extrudate while drying at 90°C for 20 min	Visualise the internal structure and characterise cracks. Resolutions: 2.25 and 1.12 µm	Follow the impregnation while dipping the extrudate in for 20 min	Visualise the internal structure after impregnation. Resolution: 2.25 and 1.12 µm

3.3.4.2 Experimental setup

In each experiment, the synchrotron was set up at different scanning conditions, as described in Table 3.5.

Table 3.5: Scanning conditions applied for each case study.

	Drying	**Impregnation**
Radiography **(lens x2: Pixel size = 2.25 µm)**	Voltage = 14 keV Exposure time = 20s Time = 20 min	Voltage = 8.98 keV (*) Bragg = -19.655°; -19.645° (*) Id-gap = 7.89 mm Exposure time = 20s Time = 30 min
Tomography **(lens x2: Pixel size = 2.25 µm)**	Voltage = 14 keV Exposure time = 1s Rotation step = 0.4° Full rotation = 180°	Voltage = 8.98 keV (*) Bragg = -19.655°; -19.645° (*) Id-gap = 7.89 mm Exposure time = 1s Rotation step = 0.4° Full rotation = 180°
Tomography **(lens x4: Pixel size = 1.1 µm)**		Voltage = 8.98 keV (*) Bragg = -19.655°; -19.645° (*) Id-gap = 7.89 mm Exposure time = 1s Rotation step = 0.4° Full rotation = 180°

(*) Values taken after calibrating the monochromator.

3.3.4.3 Tomographic reconstruction

A mathematical algorithm based on a filtered back projection procedure for fan beam geometry is required to reconstruct the shadow images. Unfortunately, as the facilities were not fully commissioned some of the analysis was undertaken manually, including determination of the centre of rotation using a sinogram. The tomographic reconstruction is performed in 2 steps.

1) Build a sinogram (Min et al., 2011): The sinogram is a collection of a projection of a single slice, in which each column corresponds to the X-Ray projection at one angle, as shown in Figure 3.15-A. In our experiment, the sample was rotated from 0^o to 180^o with an angular step of 0.4^o. At the end of the acquisition time, all the raw data was stacked together and the sinogram was built by taking one slice coming from the middle of the sample.
2) Reconstruction of the data: The tomographic reconstruction requires the knowledge of the centre of rotation, as the latter is one of the most important factors affecting the image quality (Min et al., 2011). To define the centre, one plot corresponding to a specific position of the object through the rotation is taken. Then, a rectangular area is drawn in the sinogram, where the two opposite corners correspond to the two extremities of the plot, as shown in Figure 3.15 B). By doing this, the distance along the x-axis is measured and then the middle of that segment, known as the centre of rotation, can be identified. This method is very subjective as the two opposite corners chosen could be shifted by +/- 10 pixels. Therefore, the optimum value was identified by doing the reconstruction test for twenty centres of rotation around the current

estimate. The quality of the cross section was visualised and the best reconstruction was taken. Thus, the optimal value was applied for the reconstruction of the sample.

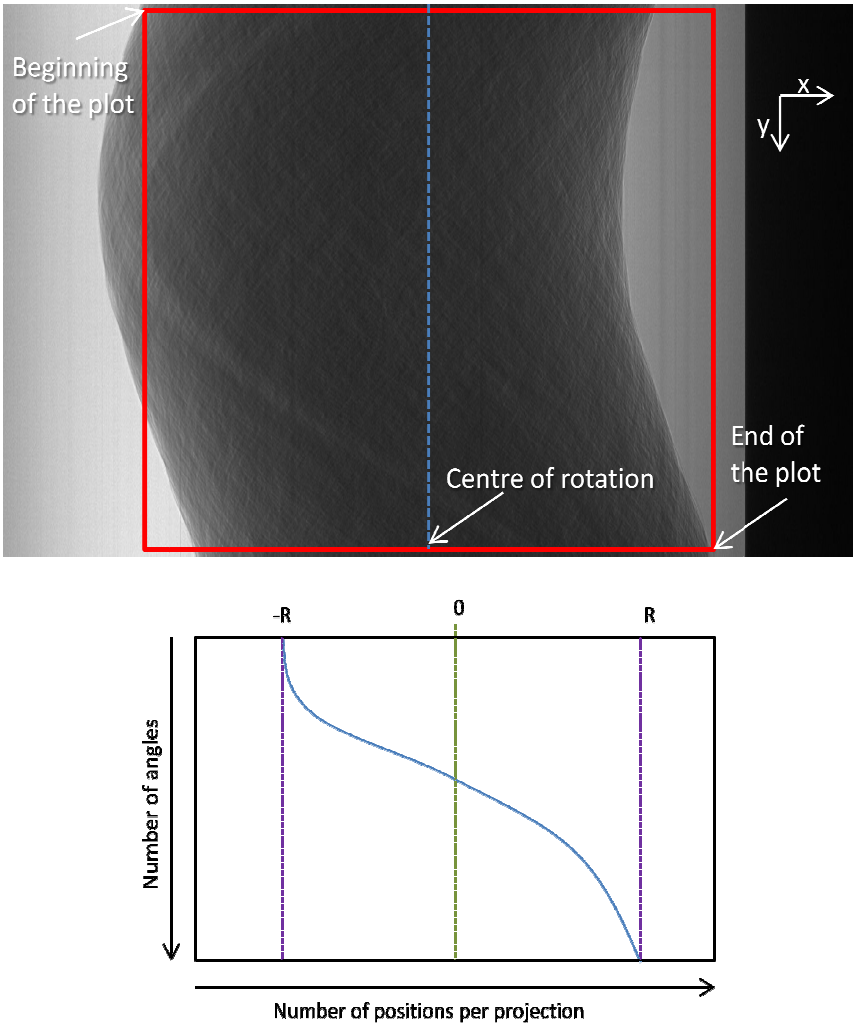

Figure 3.15: A) Sinogram of one slice taken from the shadow image. B) Schematic sinogram showing one plot of a specific point of an object during the rotation of 180^{o}.

3.3.4.4 Data processing

The slices were reconstructed from a given script developed in Diamond. The images are expressed within a 16 bit grey value range. The data processing was carried out using an open source image processing software, i.e. Image J or Fiji.

CHAPTER 4 – EFFECT OF PROCESSING ROUTE AND FORMULATION ON DENSITY DISTRIBUTION

4.1 Introduction

The investigation of the density distribution within a material has a potential importance for industries, such as pharmaceutical and catalyst industries. Porous network and strength of the catalyst support are important parameters in order to optimise the manufacturing efficiency and therefore, to improve the performance and the quality of the product.

Studies on the density of porous catalyst supports can lead to a better understanding of processes, such as sintering during production (Lu et al., 2000; Li et al., 2009). The most important aspect of a catalyst support is the fact that it consists of a suitable pore network and an overall porosity which provides a high surface area of reaction, whilst being capable of withstanding high temperatures and pressures in the reactor.

Previous studies have been reported to combine the mercury porosimetry technique with the XRCT, which was used as a complementary method (Rigby et al., 2003a; Rigby et al., 2010; Hitchcock et al., 2012), for characterising the spatial pore size distribution.

This chapter covers the capability of the X-Ray imaging technique to correlate density variation with processing route and formulation, as the internal structure depends on how catalysts have been made.

4.2 Visualisation of different type of catalyst support

To visualise the differences in the internal structure at different processing routes, five alumina support materials were scanned. The X-ray micro-Computed Tomography was set up at a voltage of 100 kV and a current of 98 µA, without the aluminium filter. Resolution of 5 µm was used. The cross sectional images resulting from the scanned samples were taken from the middle of the sample of each material, as shown in Figure 4.1.

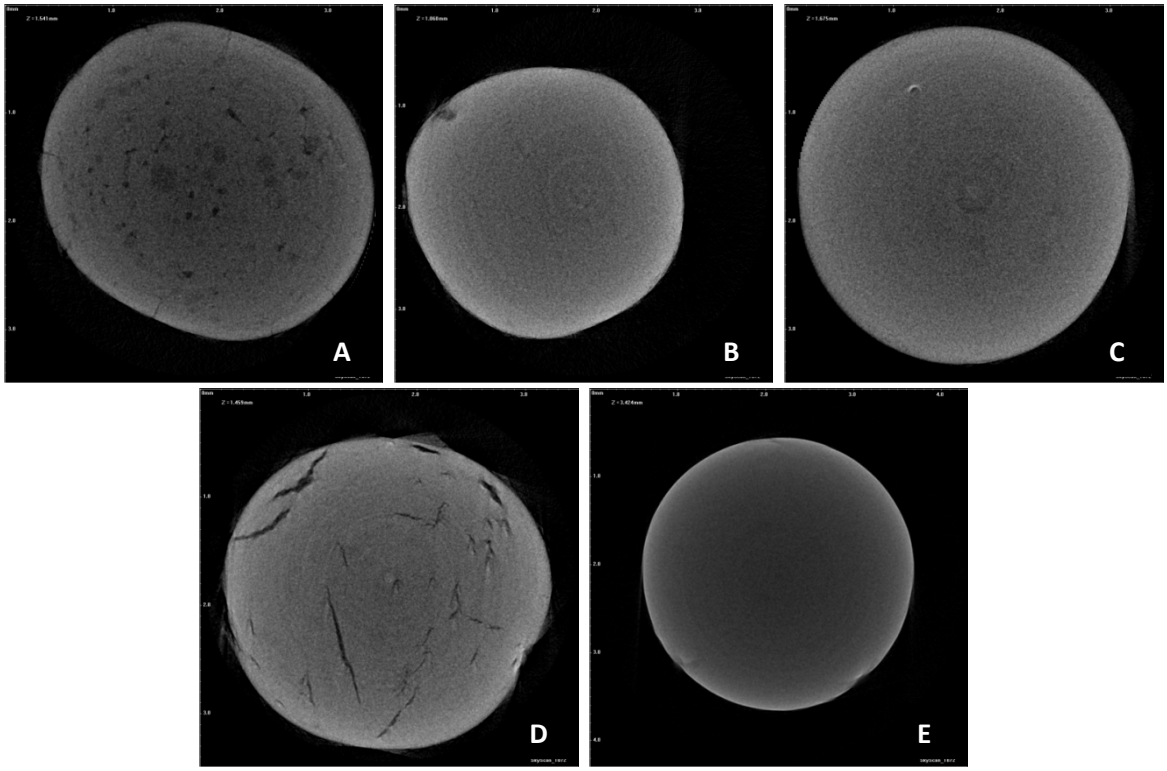

Figure 4.1: Cross sectional images of different types of catalyst supports (Skyscan 1072). A) Granule; B) Sphere; C) Tablet; D) Extrudate with cracks; E) Extrudate without cracks.

As explained in Chapter 3, the ring displayed on the reconstructed image is an artefact of the technique. Each support has a different size and shape, which are initially defined by the processing route (as seen in Chapter 2.2.4). The diameter and the standard deviation of the granule, the sphere, the tablet and the extrudate are 3123 ± 256 µm, 3252 ± 173 µm, 3154 ± 63 µm and 2870 ± 80 µm, respectively.

The information obtained from Figure 4.1 consists of the following:

- In the alumina granules, the presence of low density area dispatched in the catalyst, a high density area in the outer core, small cracks on the surface heading towards the centre and few pores, are observed.

- The two scanned extrudates resulted in different internal structures which was there before scanning, with the first one (Figure 4.1 E) showing an absence of cracks and the second one (Figure 4.1 D) showing several cracks with a tendency to grow along the z-axis, corresponding to the directionality of the extrusion.

As the visualisation on the density differences between the supports is difficult to be noticed by inspection of the reconstructed images, the grey value mean and the standard deviation were taken into account and were estimated for 200 cross sections taken from the middle of the z-axis (Figure 4.2).

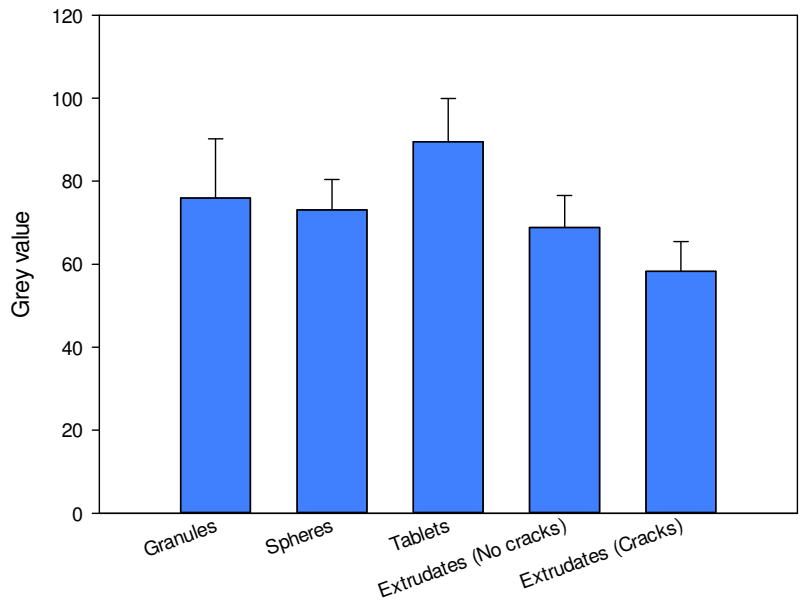

Figure 4.2: Comparison of the average of the grey value of 200 cross sectional images taken from different catalyst supports.

The density of tablets appears to be higher than that of the alumina catalyst supports. The sample with cracks has lower density than the sample without cracks. However, the densities

of the granules and spheres are similar. It is demonstrated that the change of the process has an effect on the density variation and consequently the porosity.

4.3 Investigation of the internal structure of the tablets

4.3.1 Tablets properties

In order to investigate the internal structure of the tablets in terms of density variation, four different tablets were scanned using the Skyscan 1172 micro-Computed Tomography. The formulation of those tablets is the same as the one used for the support, which is a boehmite powder. Its main purpose is to obtain catalyst supports with low macro porosity and high surface area. Graphites are also added in the formulation.

Different percentages of the graphite powder mass and different calcination temperatures were investigated for their impact on the density distribution. The formulation of those four tablets is listed in Table 4.1.

Table 4.1: Formulation of four different tablet supports.

	Tablet 1	**Tablet 2**	**Tablet 3**	**Tablet 4**
Graphite	2%	2%	10%	10%
Calcination temperature	No	607^{o}C	No	607^{o}C

4.3.2 Effect of compaction on density variation

To study the effect of compaction on density variation, the XRCT was set at a voltage of 50 kV and a current of 98 μA, with 0.5 mm aluminium filter. The resolution of 5.4 μm was applied.

The visualisation of the tomographic images and the density distribution maps from the reconstructed images, located at three different positions along the height axis (top, middle, bottom) of the tablet are shown in Figure 4.3. The sample taken as an example is the Tablet 1 (see Table 4.1).

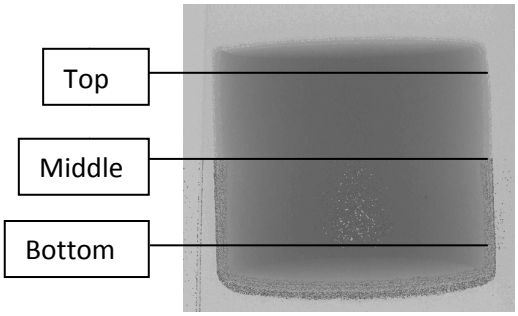

	Top	**Middle**	**Bottom**
Reconstructed images	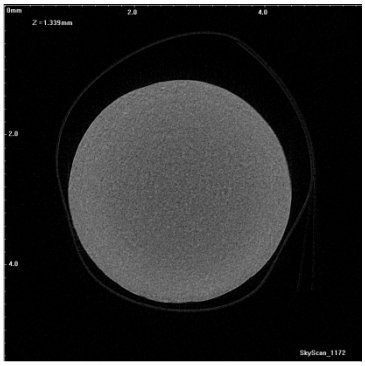	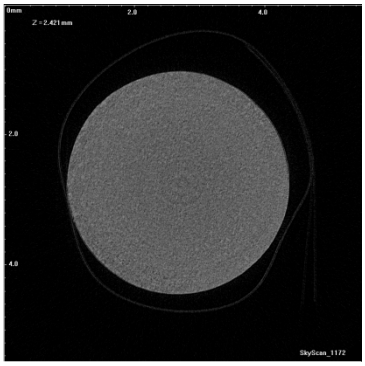	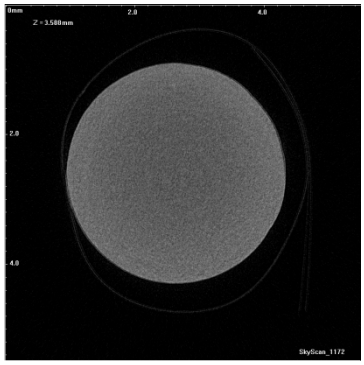
Density distribution map	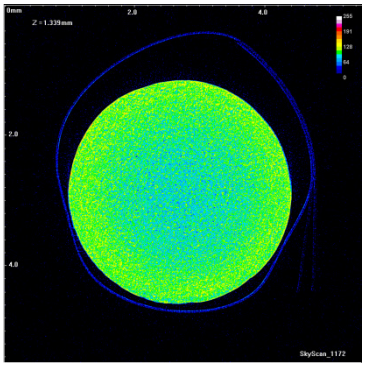	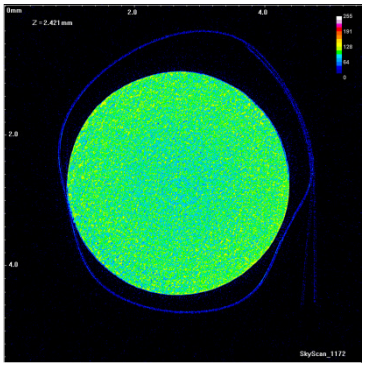	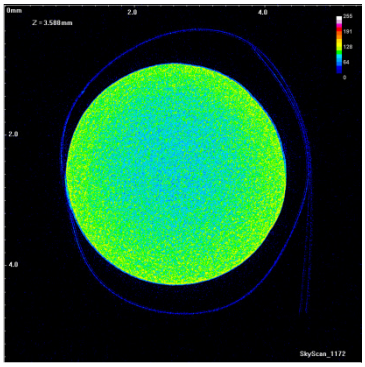

Figure 4.3: Visualisation of the tomographic images and the density distribution maps from the reconstructed images located at 3 different positions along the height axis of the tablet, example taken from the support having 2% graphite and not being calcined.

Observing the reconstructed images illustrated in Figure 4.3, it can be noticed that the internal structure of all samples is consistent and homogeneous. In order to map and compare any

density differences between the three different locations of the tablet, the density distribution map needs to be produced. The information obtained from the maps is the following: (i) the density of the outer core looks slightly higher than the inner one; (ii) a difference of density distribution is noticed by comparing the top/bottom slices with the middle one. A density variation from the centre to the surface is observed, which tends to increase by 11-15 %, as well as from the top to the bottom slices. The increase in the gradient is consistent with values reported in literature for pharmaceutical tablets (Busignies et al., 2006)

Both observations might be resulting respectively from the effect of the die wall and the punches applied during the compaction.

4.3.2.1 Effect of the die wall

To qualify and quantify the effect of the die wall on density distribution, one reconstructed image is taken from the middle of the tablet along the z-axis. The effect can be qualified by using the image processing, as shown in Figure 4.4.

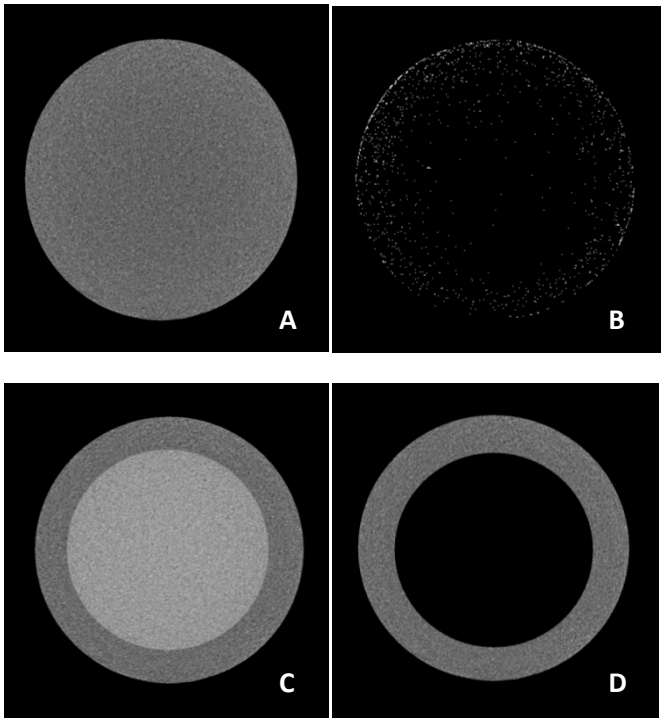

Figure 4.4: Tomographic images of the support having 2% graphite and not being calcined; A) Cross sectional image taken from the middle of the tablet along the z-axis; B) Segmented image in the range grey value scale 136-184; C) Delimitation of the outer and inner core according to the threshold range; D) Outer core (r < x < Rmax).

In order to localise the higher density area, the segmentation of the cross section is required (from picture A to picture B in Figure 4.4). The threshold range value is found by a binarisation of the image and it lies between 131 and 188.

Segmentation step is the most subjective part of the image processing, as the grey scale range chosen can have an impact on the final result. After segmentation, two areas can be distinguished on the binary image (Figure 4.4 B)): the inner core and the outer core. The thickness of the outer core depends on the localisation of the higher density area. For the threshold range between 136-188, it is the thickness of the outer core was measured to be 750 ± 23 µm. The edge of the outer core and the inner core is determined by drawing a circle from the centre of the sample (Figure 4.4 C)). Once those 2 areas are determined (Figure 4.4 D)),

the density distribution for each of them is plotted. The figure 4.5 shows the histogram of the outer and inner core of the Tablet 1.

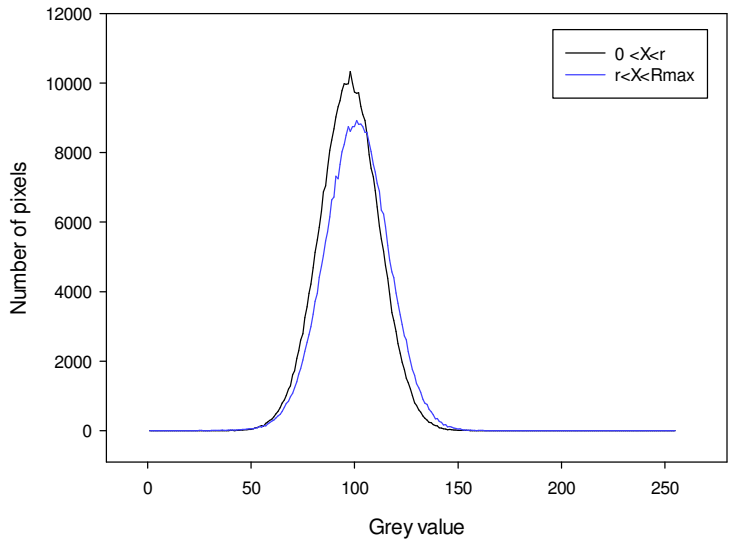

Figure 4.5: Histogram of the outer and inner core of the tablet having 2% graphite and not being calcined.

The mean and the standard deviation for the inner core and the outer core are 97.33 ± 14.24 and 100.85 ± 15.28, respectively. A chi-squared test on the intensity distribution was performed with a degree of freedom of 100 and an interval confidence selected is 0.95. Based on the chi-squared distribution table, $\chi^2_{100dl;0,95}$= 77.929. The χ^2 of the intensity distribution is approximately 83, which indicates that there is a difference between the inner and outer core. The density distribution of the outer shell shifts to the right, signifying that the surface has a higher density than the inner structure. This phenomenon could be explained by the trend of the powder to align with the direction of the die wall while the punch applies a force downwards. As the wall stops the displacement of the powder while the compaction is still in process, the particles tend to agglomerate with each other creating a strong bond. This may be an important factor depending on the force of the punch applied on the tablet.

4.3.2.2 Effect of the punches

To quantify the effect of the punches on the density distribution, three reconstructed images are taken along the z-axis; from the top, the middle and the bottom of the tablet, as shown in Figure 4.3. In order to analyse the density difference between each cross section, the whole structure was defined as being the region of interest. Figure 4.6 shows the comparison of the grey mean value and the standard deviation for each cross section taken from the top, the medium and bottom parts.

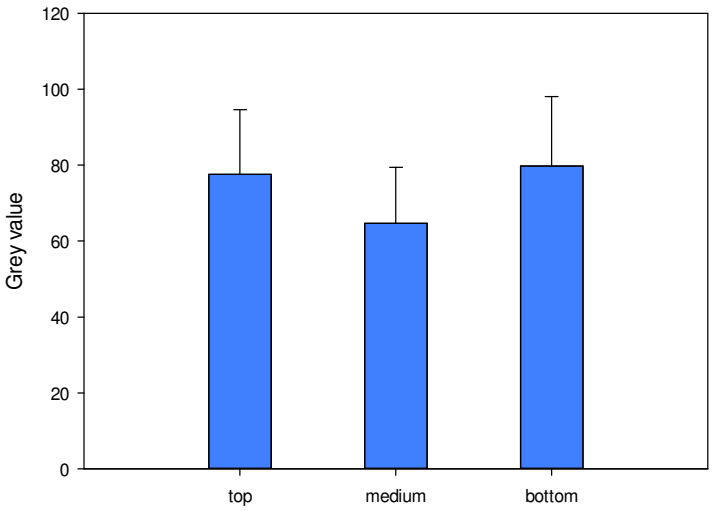

Figure 4.6: Bar chart showing the mean and standard deviation of 3 different cross sections taken from the support having 2% graphite and not being calcined, cross-sectional images are shown in the previous Figure 4.3.

According to the bar chart, the mean density on the top and the bottom of the sample is higher than the middle. That observation reveals the double compaction effect on tablets.

4.3.3 Effect of the amount of graphite added for tableting

To compare the effect of the graphite on the density distribution, two tablets with different amounts of graphite mass (2 % and 10 %) were analysed. None of the samples was calcined and they were scanned together. The comparison of the density distribution between the two samples is shown in Figure 4.7.

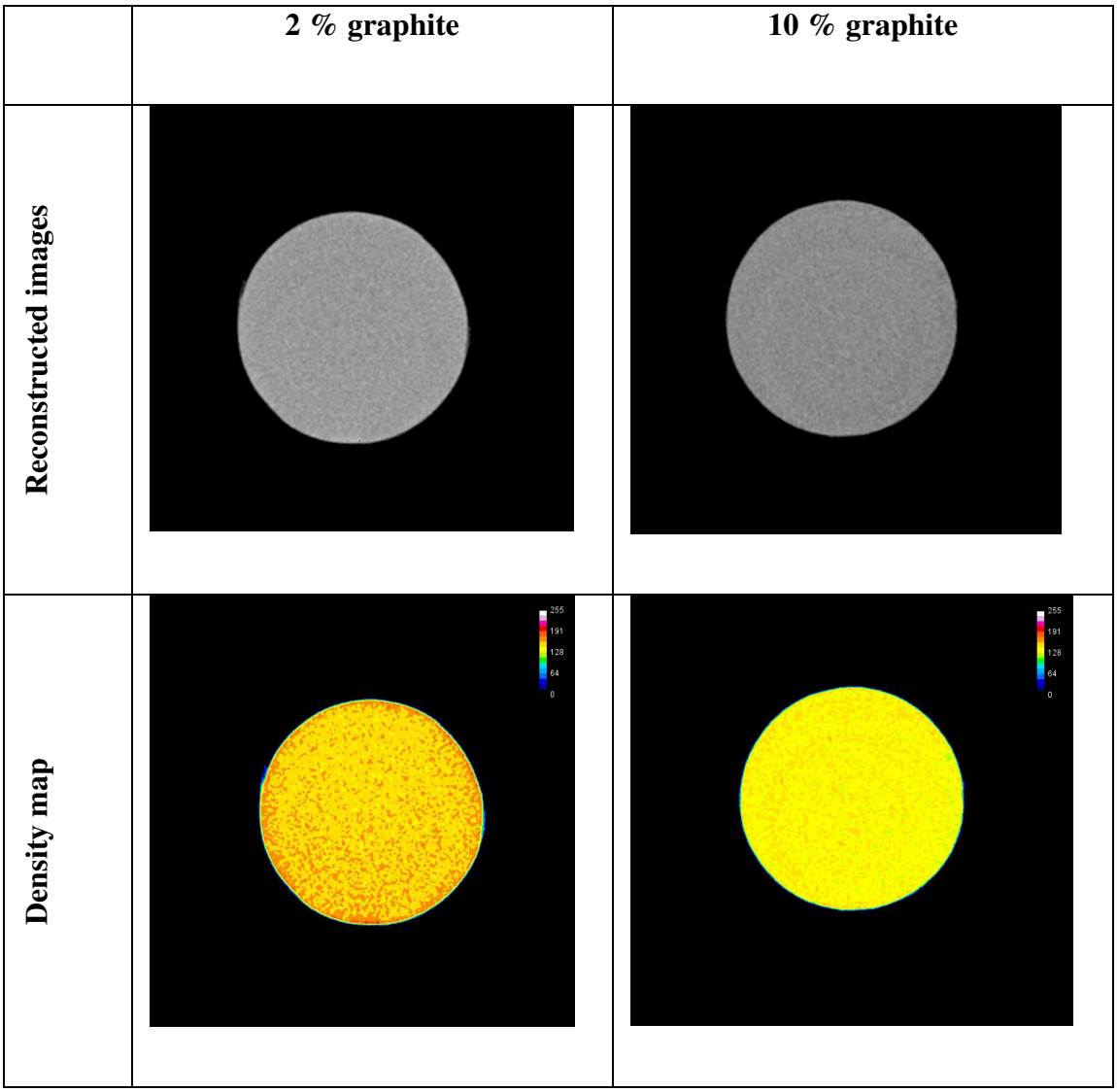

Figure 4.7: Visualisation of the reconstructed images and their respective density distribution maps of one tablet having 2 % and 10 % graphite in their formulation.

Inspection of the cross-sections taken from the middle of the catalyst support, showed small density variation, which is explained in Chapter 3.3.3.2. Indeed, both cross sectional images were similar by showing the same tendency: a heterogeneous structure with high/low intensity area within and a tiny high density ring on the surface of the support due to the compaction process (as explained in the previous section). Although the reconstructed cross section images in grey scale were similar, differences in the density map distribution were observed. The density of the sample with 10 % graphite was less intense than the one with 2 % graphite, as the mean grey values are 138±15 and 154±18 respectively. Therefore, the amount of graphite added in the formulation had an effect on the X-Ray absorption of the support. The X-Ray absorption was inversely proportional to the percentage of graphite added, consistent with work reported in literature (O Castillo-Villa et al., 2013). That can be due to fact that the absorption of the carbon in the graphite carbon-chain is lower than the alumina, based on Beer Lambert's law.

Table 4.2: Grey value mean and standard deviation on the inner and outer core for 2 tablets having respectively 2% and 10% of graphite.

Tablet	2% graphite not calcined		10% graphite not calcined	
	Inner core	Outer core	Inner core	Outer core
Grey value mean	153.75	156.86	139.13	136.38
Standard deviation	6.86	21.14	6.12	18.66

A t-test was performed to establish whether differences between the sample means are significant. For this experiment, the degree of freedom is of 100 and an interval confidence of 0.95. The null hypothesis assumes that the difference between 2% and 10% graphite means is 0. The test resulted in a means difference of 3.89 and the two tailed test resulted in a *p*-value of 0.05. The statistical result shows that there is a significant difference between 2% and 10% graphite.

4.3.4 Effect of the calcination on the support

A total number of twenty tablets was separated into four groups of five samples each.

- First group: non calcined samples with 2% of graphite
- Second group: calcined samples with 2% of graphite
- Third group: non calcined samples with 10% of graphite
- Fourth group: calcined samples with 10% of graphite

The calcined samples were heated at a temperature of 605^{o}C for a certain period of time and they resulted in size change as reported in Table 4.3. For each group, five measurements of diameter and height were taken, based on literature reported (Kong and Lannutti, 2000; Douarche et al*.,* 2001; Sinka et al*.,* 2004), and the average was calculated. The number of samples that can be used is limited by the time required for acquisition and reconstruction (approximately 1 hr for each step). The option of running an "oversize" scan was used, enabling the acquisition of multiple samples at a given time. In most of the cases, the oversize scan is used for scanning samples with a diameter greater than 4 cm. In this case, the device allowed five tablets to be scanned simultaneously.

Table 4.3: Size and standard deviation of tablets.

Tablet	2% not calcined	2% calcined	10% not calcined	10% calcined
Height (μm)	2903+/-56	2841+/-31	3055+/-27	2707+/-45
Diameter (μm)	3387+/-34	3169+/-48	3318+/-76	3209+/-64

For each group of tablets, the size of the samples is very similar, as the standard deviation is very small. These results are expected because the tableting was done under the same conditions, and the samples were produced from the same batch. In both cases, it appears that the size of the samples decreased by 15% after the calcination process. The reduction of the sample size is related to a change in structure as the support becomes more porous. The calcination process tends to develop narrow pores (Trimm and Stanislaus, 1986). Also, the pore diameter increases and the surface area decreases when increasing the calcination temperature from 500^{o}C to 800^{o}C, according to Sun et al. (2008). That observation might also suggest an increase of density due to the decrease of surface area. The effect of the calcination process on the density is shown in Figure 4.8.

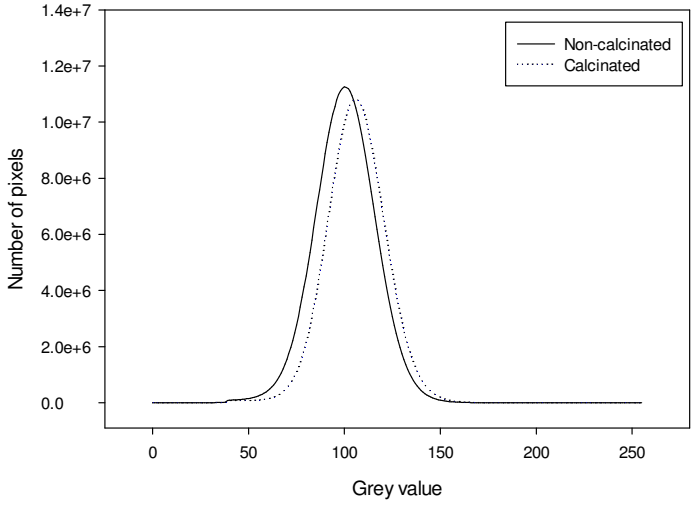

A)

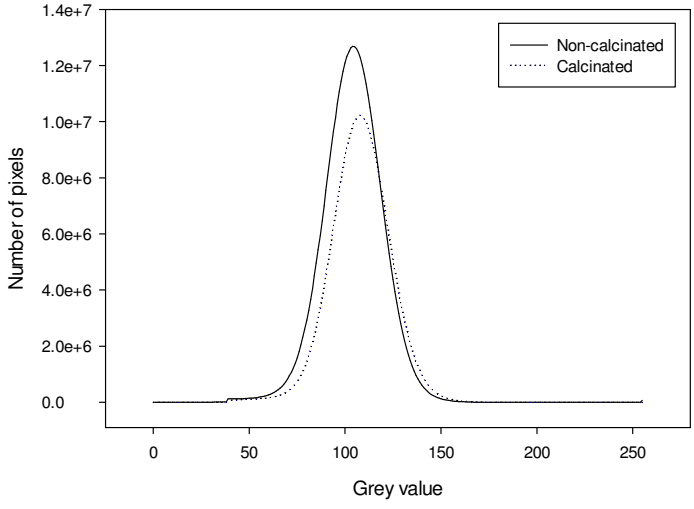

B)

Figure 4.8: Effect of the calcination process on grey value distribution for different catalyst supports; A) with 2% graphite and B) with 10% graphite.

In both conditions, (2% and 10% of graphite) the calcined sample appeared denser than the non-calcined one, as the grey value distributed is shifted towards slightly higher grey values. A chi-squared test on the intensity distribution was performed in order to see whether a difference between non-calcined and calcined sample could be shown. The degree of freedom is 100 and the interval of confidence chosen is 0.95. Based on the chi-squared distribution

table, $\chi^2_{100dl;0,95}$= 77.929. The χ^2 of the intensity distribution is about 81.63, which means that there is an effect of the calcination on density.

4.4 Investigation of the internal structure of the granules

4.4.1 Characterisation of the density distribution of granules

4.4.1.1 Visualisation of the internal structure

The density variation of the internal structure of the granules was investigated using the Skyscan 1172 micro-Computed Tomography. The system was set at a voltage of 60 kV and a current of 98 µA. The use of the 0.5 mm alumina filter was required. The resolution of the tomographic images was 5.93 µm. Figure 4.9 shows the reconstructed cross-sectional image taken from the middle height axis of the granule JM800B7 and its respective density distribution map.

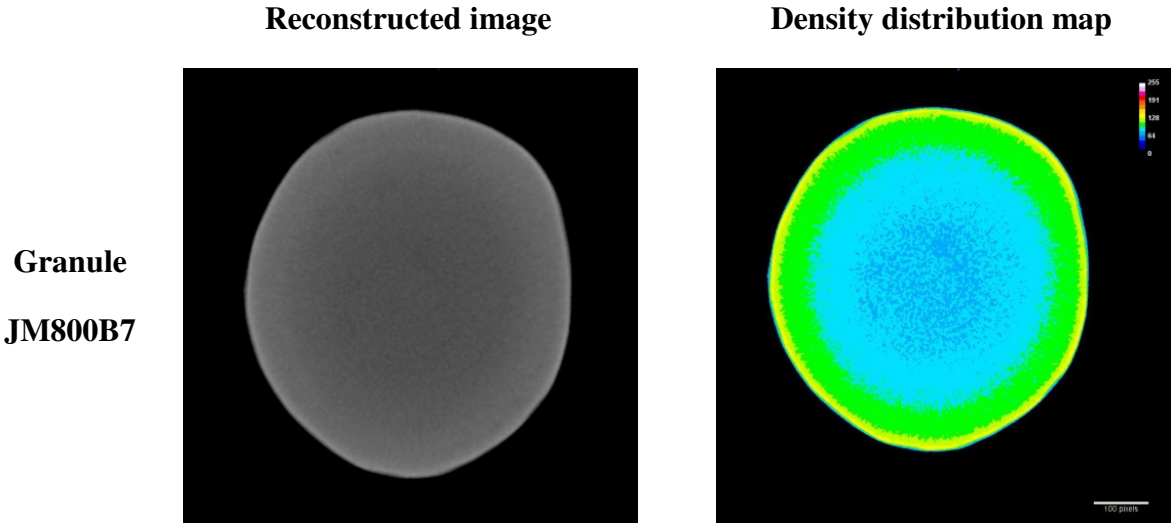

Figure 4.9: Visualisation of the reconstructed cross-sectional image taken from the middle height axis of one sample and its respective density distribution map.

The reconstructed image does not show obvious differences across the sample, in terms of density variation, as compared to the density map which provides more information. Indeed, a gradient of density from the centre to the surface is revealed, which means that the sample is not homogeneous. Four distinct regions could be visualised according to the colours. The lowest density is in the centre of the granule, and the highest one is in the periphery. The way in which different regions in the granule are organised might be related to the manufacturing process. Although a preliminary experiment was done to decrease the beam hardening artefact effect by using the aluminium filter, as detailed in Chapter 3, the same process was carried out with the granules in order to confirm the findings. The sample was cut into half and was placed in the chamber of the X-Ray micro-Computed Tomography, showing that the thin layer is part of the catalyst (not an artefact). Four well-defined regions could be visualised qualitatively by the mapping of the (X-Y) cross section, but they could not be identified quantitatively, as shown in Figure 4.10.

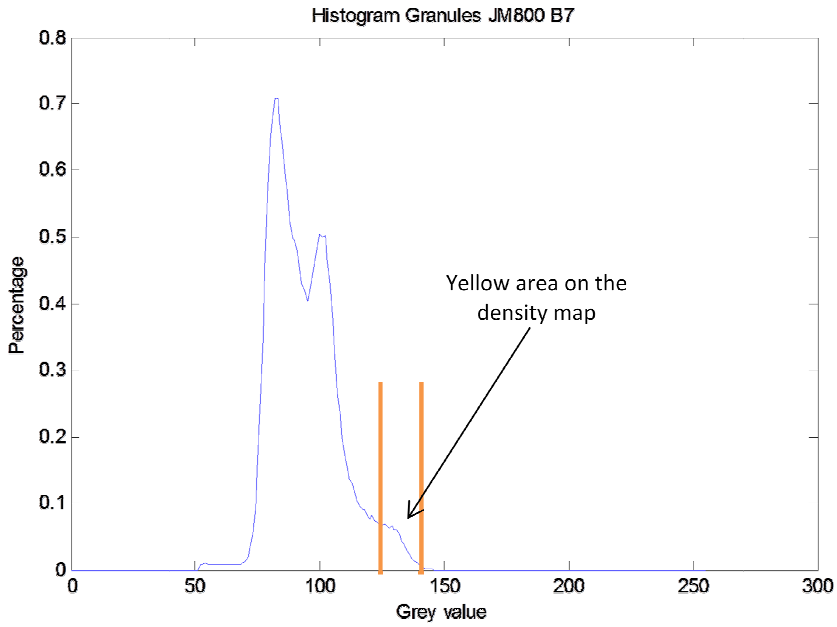

Figure 4.10: Density distribution of the granule JM800B7.

Figure 4.10 shows a bimodal distribution for the grey value revealing the presence of two peaks, those referring to the lower and higher density area. In addition, a small third peak could be identified between grey scale values of 120-150. After segmentation of the image based on the grey value range, it appears that the third peak is related to the thin high density layer on the surface. In essence, the two main peaks correspond to the inner core and the periphery of the catalyst support, respectively.

4.4.1.2 Determination of the thickness of the outer core

The combination of information obtained from the histogram and the density distribution map provides information on high and low density areas, and therefore, the presence of the inner

and outer core. Different methods were used to distinguish those 2 areas and then the thickness of the outer core was determined.

4.4.1.2.1 Deconvolution

Deconvolution is one of the methods used to determine areas of low and high density distribution. The principle is based on the separation of a bimodal distribution into two Gaussian distributions according to a given equation, using the image processing software (MATLAB, 2007a). The number of unknown parameters in the equation, made the mathematical operation challenging and therefore, the deconvolution of the bimodal distribution was done manually.

The method used to identify areas of different densities are as follows: A circle is drawn manually along the edge of the low and the high density. The grey value distribution of the two surface areas of the sample, which refers to the inside and the outside of the circle, is plotted against the number of pixels, as shown in Figure 4.11.

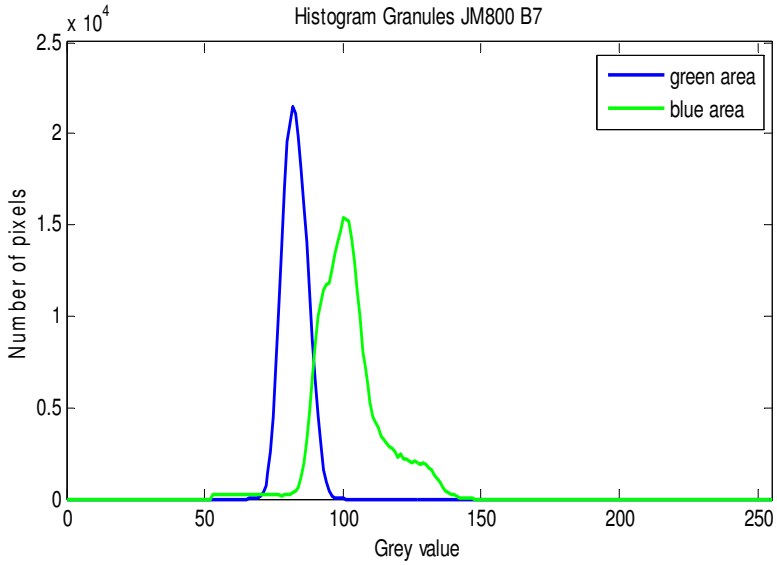

Figure 4.11: Grey value distribution of the inner core (blue) and the outer core (green).

If those two plots were merged, the resulting distribution is similar to the bimodal distribution shown in Figure 4.11. The grey value corresponding to the intersection of the two curves is approximately 96, and that value is similar to the mean grey value of the sample (GV= 95), as described in Chapter 4.4.1.2.2. Then, by defining the threshold value scale of 96-150, the thickness of the outer core can be measured and the length is obtained to be 0.52 ± 0.03 mm.

4.4.1.2.2 Method based on the intensity variation and the grey value mean

Image analysis was done with one reconstructed cross section, by finding the centre of the sample and plotting the intensity variation along a line at 4 different angles (0; π/10; π/5 and π/3), as shown in Figure 4.12.

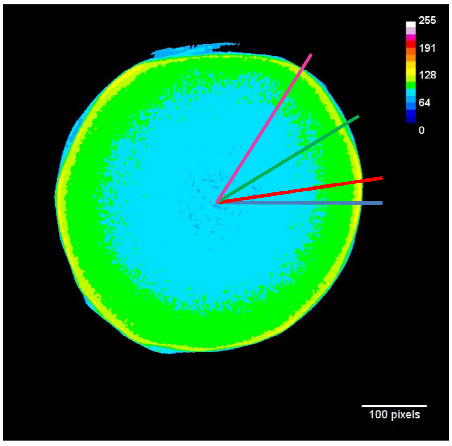

A)

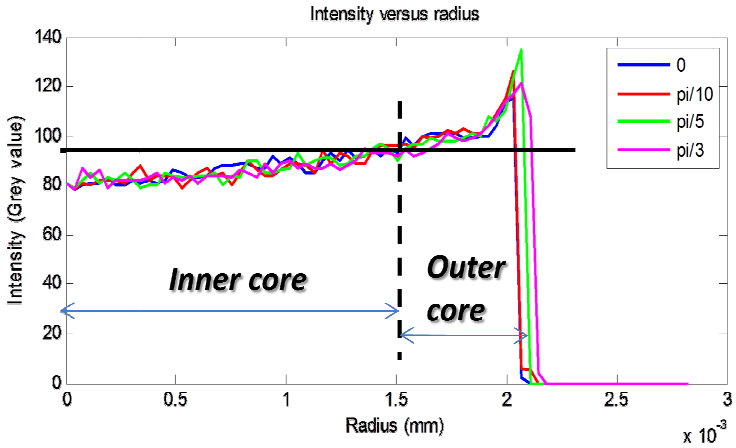

B)

Figure 4.12: A) Density map of one reconstructed cross section taken from the middle of the granule; B) Intensity variation along the line at different angles (0; π/10; π/5 and π/3).

Figure 4.12 shows that the intensity plot for each angle follows the same trend, as the intensity tends to change positively with the radius. The density increased by 37 % from the centre to the surface of the granule. The fluctuation on each plot can be explained by either the real density difference or the existence of an artefact (noise). Then based on the plot shown in Figure 4.12, it would be possible to find the thickness of the outer core by using two distinct methods with two different starting points: (i) the use of the mean grey value obtained from the data analysis; and (ii) the use of lines by drawing 2 tangent lines manually.

- Mean grey value of the sample: The mean value of the sample is approximately 95 and its standard deviation is 20. A line with y = 95 is drawn in the graph and its intersection was obtained based on the intensity plots (Figure 4.12). After determining the intersection point, its coordinate points (X_i= 1.5; Y_i= 95) could be obtained. Then, by knowing the radius of the catalyst support (X_{max}= 2.1 mm), the thickness of the outer core (X_{max}-X_i) was estimated to be 0.57 ± 0.03mm.
- By drawing two lines: Two lines are drawn manually on the graph, with their intersection referring to the limit of the 2 cores. Then, the outer core thickness could be determined. Using this method, the thickness was estimated to be 0.45 ± 0.04 mm.

Two areas were revealed in the granule, and the thickness of the outer core was determined by using the above methods. The value obtained from the deconvolution technique and the method using the grey value mean is almost similar, and the thickness calculated at the outer core is in both cases 0.54 mm. However, the understanding of the presence of the density distribution could not be explained due to a lack of information obtained from the granule JM800-B7.

4.4.2 Properties of granules

In the following section, the effect of formulation on five given granules (Johnson Matthey, UK) was investigated based on knowledge of their physical properties. Information on those granules was limited due to the commercial confidentiality constraints. Only proportions of binders and results related to the structure analysis were provided by the Johnson Matthey. Data acquired from the mechanical test and the attrition loss were used to analyse the results obtained from the XRCT. Information on those samples is shown in Table 4.4.

Table 4.4: Effect of the binders on the properties of five types of granules.

Granules	Binder A* (%)	Binder B* (%)	Strength (MPa)	Attrition loss (%)
EMC1	14	0	2.3	0.1
EMC3	7	7	6	negative
EMC5	0	14	2	16
EMD5	0	14	4	1.3
JM800-B7	unknown	unknown	unknown	unknown

* A and B were two different binder; information were very limited due to the confidentiality.

The size of the samples differed slightly from batch to batch, and the granule was taken randomly from each batch. Moreover, the main constituent was identical for the granules EMC1, EMC3 and EMC5, but different between EMC5 and EMD5. Therefore, the interest of that section was to visualise and to study the effect of formulation on density variation by modifying two parameters: (i) the main constituent and (ii) the quantity of binders.

To study those two parameters on the effect on density distribution, the granules were scanned simultaneously. Three sets of experiments were performed using different granules each time setting the system at a voltage of 60 kV and a current of 98 µA. The use of the 0.5 mm aluminium filter was required. The resolution of the tomographic images was 6.93 µm.

4.4.3 Effect of the main constituent on the density distribution

The effect of the main constituent on the density distribution was tested by comparing qualitatively the granule EMC5 (made with constituent C) with the granule EMD5 (made with constituent D), using the same binder and quantities (Table 4.4) Figure 4.13 shows the reconstructed cross-sectional images taken from the middle height axis of two samples and its respective density distribution maps.

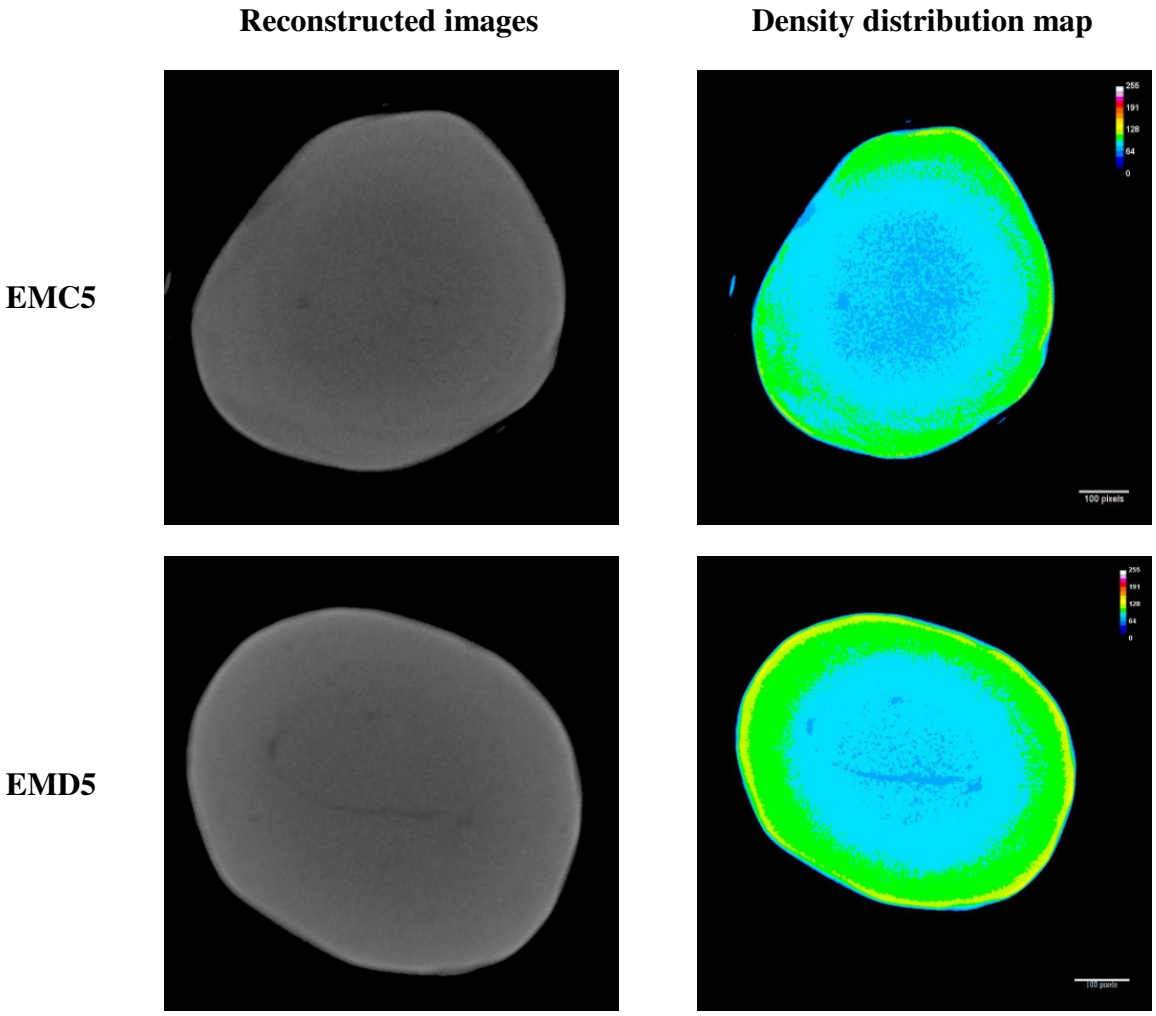

Figure 4.13: Visualisation of the reconstructed cross-sectional images taken from the middle height axis of two samples (EMC5 and EMD5) and its respective density distribution map.

The greyscale reconstructed images and the density map show differences between the 2 granules. Looking at the density map distribution, the EMC5 support seems to be a lower density as compared to the EMD5 support. The inner core appears highly porous whereas the high density layer of the outer core is thinner. A low density area of the surface that has the same density as the middle part of the sample is visualised. That can be due to the 2 granules being stuck with each other during the granulation process. As the same observation could be made with a granule taken from the same batch, the trend of agglomeration between granules

can be produced. Conversely, the granule EMD5 seems to be denser at the outer core and less porous at the inner core. In summary, the main constituent chosen, appears to have a significant impact on the final internal structure by altering its porosity. In our case study, the constituent C seems to form weaker bonds between the molecules, possibly owing to the presence of a long chain or a big molecule, creating an important pore network in the middle of the granule and therefore, reducing the strength. However, it is difficult to characterise the attrition loss by using the XRCT.

4.4.4 Effect of the binders on the density distribution

The effect of the binder on the density distribution was studied qualitatively on the granule EMC1, EMC3 and EMC5 as the main constituent is similar. Figure 4.14 shows the reconstructed cross-sectional image taken from the middle height axis of three samples and their respective density distribution map.

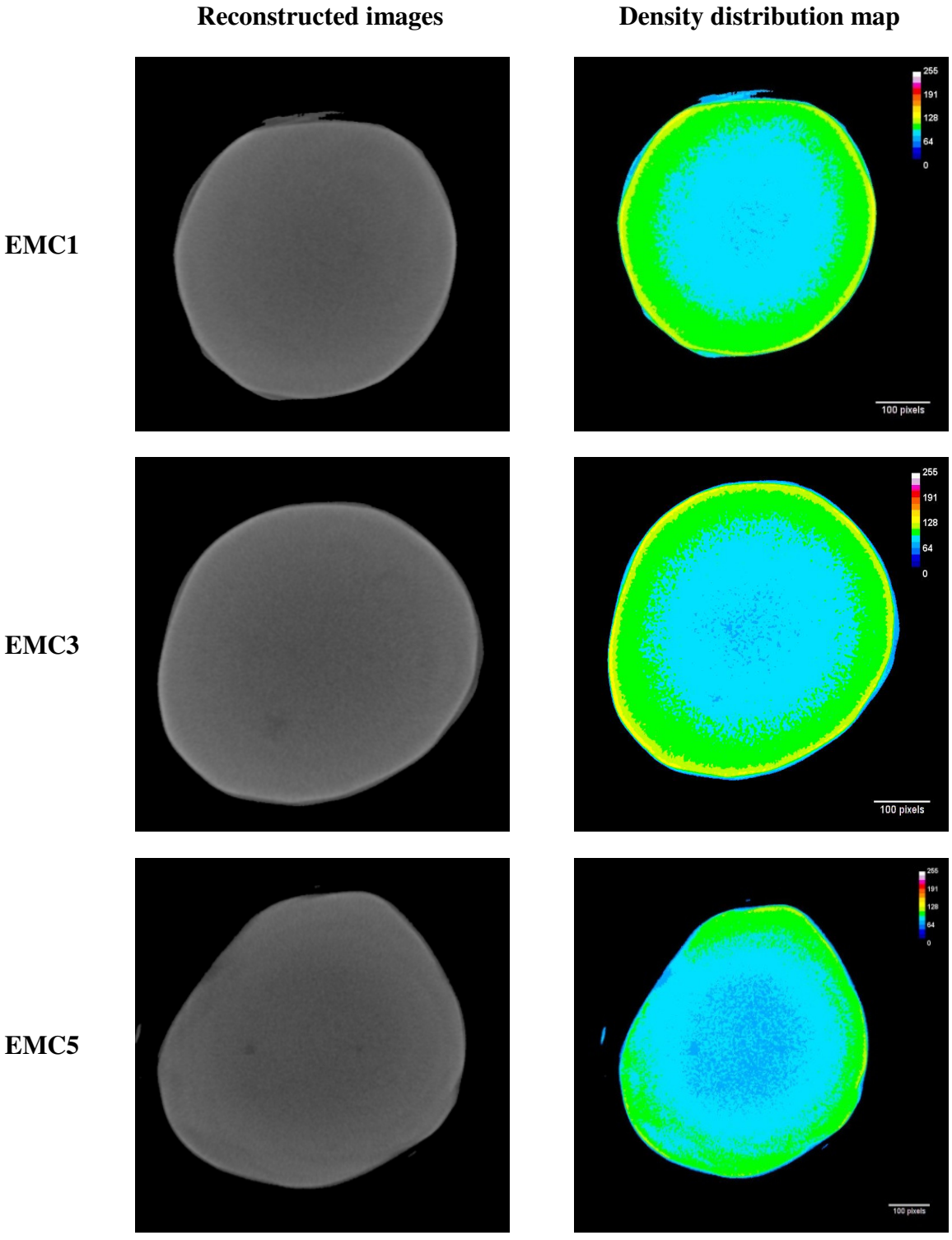

Figure 4.14: Visualisation of the reconstructed cross-sectional images taken from the middle height axis of two samples (EMC1, EMC3 and EMC5) and its respective density distribution map.

Although the reconstructed cross-sectional images of the three granules look similar, their respective density map shows differences, which means that the kind of binder and its quantity could induce an effect on the final structure. The two main differences are still the thickness of the outer core and the lower density area of the inner core. The use of the binder A or the binder B could modify the density profile of the internal structure. Indeed, the thickness of the outer core is about 466 ±42 µm for EMC1 and about 275 ±39 µm for EMC5. The significant variability in the thickness, obtained from EMC5 is due to the low density area of the surface, as discussed in the previous section. The inner core of the granule EMC5 shows an area where the porosity appears to be of importance. The binder A, which is the only binder used in the EMC1, seems to build up strong connection with the main component as the outer core is thicker and the inner core denser. As far as the use of binder B is concerned, it seems that a highly porous catalyst support is created at the inner core. According to the data obtained from the strength measurements, the strength of EMC1 is approximately 2.3 MPa whereas EMC5 is approximately 2.0 MPa. When combining half the quantity of each binder in the formulation of the granule EMC3, their respective properties were elucidated. The centre of the inner core shows a porous region and the thickness of the outer core is important (about 436 ± 92 µm). Therefore, the mixture of the two binders could introduce additional properties to the granules, and subsequently increase the strength considerably (strength of EMC3= 6 MPa).

4.5 Investigation of the extrudates

In catalysts, different supports could be used as seen in the section 4.1. Previous studies have shown how the density can be affected by the formulation and the process route in making

catalysts. The following section will focus on how the extrusion process can affect the density distribution.

Extrudates could exist in different shapes depending on the process used, e.g. cylindrical or trilobe. Those two types of extrudate were scanned and analysed. For the cylindrical extrudate, the XRCT (Skyscan 1072) was set at a voltage of 100 kV and a current of 98 µA and a resolution of 5 µm was applied. For the trilobe extrudate, the Skyscan 1172 device was set at a voltage of 50 kV and a current of 98 µm, with a pixel size of 8 µm. The cross sectional images resulting from those scans were taken in the middle of the sample of each material, as shown in Figure 4.15.

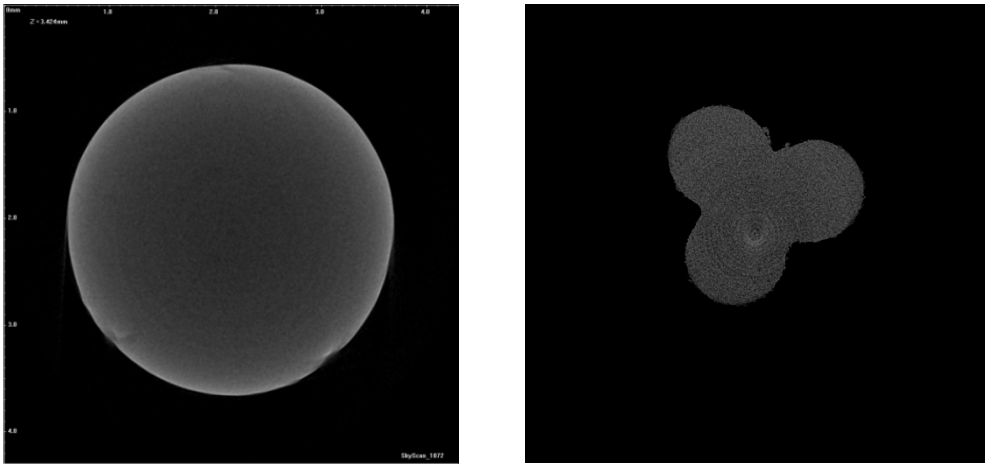

Figure 4.15: Reconstructed cross-sectional image taken from a cylindrical extrudate (on the left); from a trilobe extrudate (on the right).

Different alumina extrudates produced from the same batch were scanned. Among those catalyst supports, it appeared that 40 % of them have fault in their structure, such as cracks.

According to all the scans done, those defects mostly occurred in the inner structure but cracks could also be observed on the surface.

One cracked alumina extrudate was examined by the Scanning Electron Microscopy (SEM) after scanning the sample with the XRCT. SEM can provide magnification of up to 100000 times, sufficient to view nanopores, whereas the resolution of the tomography technique using the Skyscan 1072 device is about 2 µm. The analysis of the support surface is done at different magnifications, as shown in Figure 4.16.

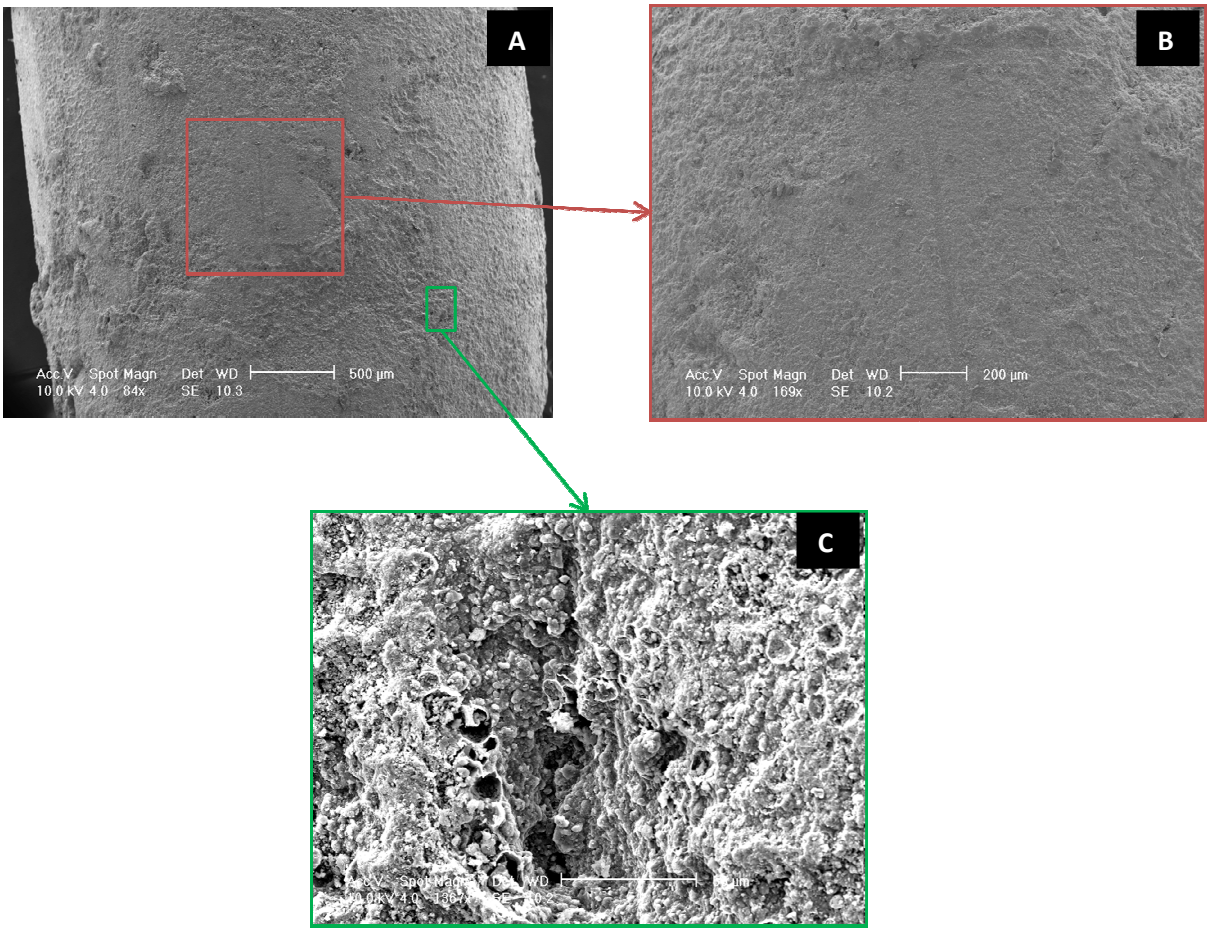

Figure 4.16: Scanning Electron Microscopy images taken from an extrudate showing cracks in the surface.

The scanning electron micrographs in Figure 4.16 (A-B) show a segment of 550 ± 10 µm on the surface that is probably caused by the die of the barrel, while the paste is under shear force during the extrusion process. It has been shown that the surface cracking is often caused by the extrusion temperature, friction, or speed of extrusion. It might also happen at lower temperatures if the extruded product temporarily sticks to the die. Two different surfaces have appeared to crack after the extrusion and the drying process: a) Cracks that appear at some distance along the extrudates; b) Cracks that occur along the entire length (Peng et al., 2004). In Figure 4.16 C), a crack of about 35 µm in size, surrounded by few pore entrance networks

could be observed. The SEM technique could provide information on the surface of the catalyst support down to the resolution of the XRCT. If the viewing of internal structure is needed, it requires cutting the sample and therefore the internal structure would be damaged. The use of the XRCT could allow us the visualisation of the internal cracks.

4.6 Conclusion

This chapter demonstrates the capability of the XRCT to correlate density distribution with processing route and formulation of different catalyst supports. By visualising the internal structure of different catalyst support, it was possible to study the effect of the processing parameters and the formulation. Cross sectional images and density maps were obtained for all catalyst supports.

The internal structure of different catalyst supports were investigated and revealed information on density variation, such as the presence of low density areas dispersed in the catalyst, a high density area in the outer core, cracks and pores. The density distribution is different, according to the catalyst shaping and the processing route. For instance, the density of tablets appears to be higher than that of the alumina catalyst supports. However, porosity could not be determined as pores size of those catalyst supports seems to be below the resolution of XRCT. The porosity level could be deduced from the grey value variation and therefore, the density distribution.

In tablets, an important heterogeneity with high density area in the periphery and low density in the inner core is shown in the cross sectional images (X-Y) and its respective density maps.

That heterogeneity is the result of the compaction process due to the effect of the punches and the die wall.

The amount of graphite added seems to have an effect on density, as the density of the sample with 10 % graphite was less intense than the one with 2 % graphite. A higher amount of graphite added in the support might decrease the density and therefore, increase the porosity of the catalyst support.

The calcination process has an effect on density, as the sample seems to be slightly denser when it is processed under higher temperature conditions. Calcination tends to develop narrow pores and therefore, changes the structure of the support, for instance, a decrease in the size of the sample.

In granules, lower and higher density areas are revealed by the presence of 2 obvious peaks in a bimodal distribution. Then, the thickness of the outer core was determined using 3 different techniques. The effect of formulation was studied. The change of component and binder has a significant impact on density distribution and strength.

The extrusion process affected the density distribution. Among the alumina extrudates, it appeared that 40 % of them have defaults in their structure, such as cracks. Those cracks can be formed inside as well as outside the support.

CHAPTER 5 – EFFECT OF THE PROCESSING CONDITIONS ON THE DEVELOPMENT OF CRACKS

5.1 Introduction

All the catalysts undergo mechanical, physical and/or chemical alterations, called deactivation (Richardson, 1989). Mechanical defects such as failures, caused during catalytic reactions can affect the performance of the catalyst. Among the failures, cracks are the most common defects, which are conventionally defined at a size higher 10 micrometres (Ammouche et al., 2001). The classical concept of crack entails the onset and propagation of micro defects along a discontinuity line, which is not necessarily linear or smoothly oriented.

The catalyst preparation is a crucial step for controlling and ensuring the quality of the final product, involving a variety of sub-steps with critical points. As described in Chapter 2.2.4.1.1., extrusion is a commonly used technique, which provides the catalyst support with a cylindrical shape (Perego et al., 1997; Campanati et al., 2007). Typically, a wet paste is extruded through a die, with a specific shape and diameter whose quality can be compromised by a defective structure observed on its surface. That kind of uneven structure can cause roughness in the paste as shown in Chapter 4. In the case of aluminium extrusion, one of the

main defects that occurres, is surface cracking (Peng et al., 2004). After being extruded, the paste is dried at a specific temperature in order to eliminate the solvent, which is usually water, obtained from the support. The drying process can induce micro-cracks, limiting the strength of the support (Pourcel et al., 2005), and therefore, increasing the probability of the propagation of cracks during the calcination stage (Mercier et al., 1998).

Failure properties have been widely investigated in a number of industrial processes and materials, such as in the concrete (Ammouche et al., 2001), stone/rocks (He, 1998), metallurgy with the Al alloy study (Peng et al., 2004; Ferrie et al., 2005), powder metallurgy (Tahir et al., 2006), pharmaceutical products (Wu et al., 2005; Wu et al., 2008) and food industries (Herremans et al., 2011). In the above studies reported, imaging techniques were used for the characterisation of failures. Different experimental techniques have been used to study the cracks and to visualise their structures in 3-D. For instance, destructive experimental techniques have been used to visualise cracks in metal by using ink penetration (Toyosada et al., 2004), heat tinting (Ravichandran et al., 1992), eddy current inversion (Bowler et al., 2002) and serial sectioning (Clement et al., 1984). However, there is not much information on the characterisation of cracks in catalysts by non-destructive techniques, such as XRCT and synchrotron tomography.

The current chapter is divided into two parts: (i) the development of a methodology on how to detect and characterise cracks within the catalyst using the XRCT; and (ii) the application of the developed method in investigating the effect of the water content, the ram extrusion speed, the drying temperature and the calcination process on the crack initiation and propagation.

5.2 Microstructure of alumina extrudates

The preparation of the catalyst support involves four different steps:

- Preparation of the paste,
- Extrusion process,
- Drying process,
- Calcination process.

Each step was carefully analysed for investigating the effect of the physical and mechanical properties on the crack formation.

The preparation of the sample is described in detail in Chapter 3. For the extrusion and drying process, extreme conditions were chosen, slow and fast ram speed (10 and 50 $mm.min^{-1}$) and drying rates (room temperature and fluidised bed dryer), respectively. As reported in literature, the choice of parameters used in the extrusion and drying steps can lead to the initiation of cracks. After extruding the paste, at the two extreme ram speeds, two drying conditions were performed. Half of the extrudates were dried at room temperature (~20-25^{o}C) overnight and the other half were dried for 20 min in a fluidised bed dryer at 105^{o}C.

5.2.1 Reconstructed images

Individual tomography scans of sixteen extrudates were acquired after the drying process. The pixel size applied for all scans was 5.5 µm. The cross sectional image of each sample is presented in Table 5.1.

Table 5.1: Visualisation of the cross sectional image of all samples for each experimental condition.

Water content	Ram speed	Drying process		Ram speed	Drying process	
		25°C	105°C		25°C	105°C
0.92 kg water/kg solid	10 mm/min	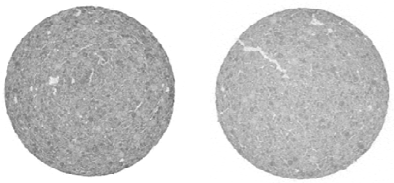		50 mm/min	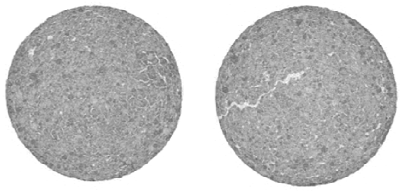	
0.96 kg water/kg solid	10 mm/min	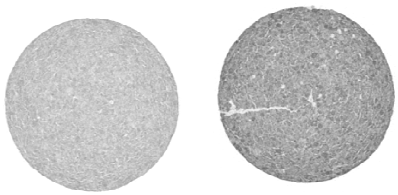		50 mm/min	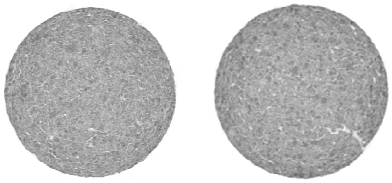	
1.00 kg water/kg solid	10 mm/min	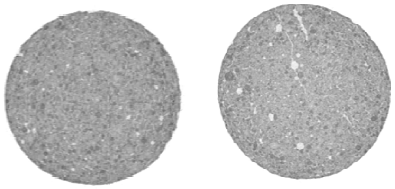		50 mm/min	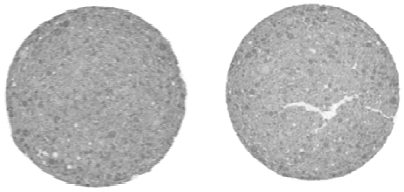	
1.04 kg water/kg solid	10 mm/min	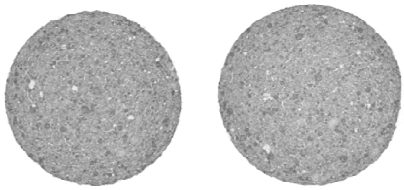		50 mm/min	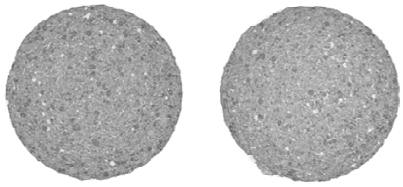	

The different density regions, the pores and cracks observed in the different extrudates induce structural heterogeneity of the catalysts. The surface of the support seems denser when compared to the core. From the above cross sectional images, it appears that the extrudates dried in the fluidised bed tend to have more cracks when compared to the samples dried in

room temperature, where only pores are observed. The above observations are made based on a 2-D visualisation along the horizontal axis. When the visualisation is extended towards the vertical axis, circular or cylindrical voids (pores and cracks) appear to be present also in the room temperature dried extrudates. The results indicate that the drying process makes the occurrence of cracks evident and consequently influence significantly the internal structure of the extrudates.

5.2.2 Spatial distribution

To visualise the spatial distribution of voids, a 3-D model was developed with the image being segmented into black and white. The threshold refers to the grey scale, which ranges between 0 and 255 and is related to the density of the object. An example of an extrudate sample with initial water content of 0.92 kg water.kg solid^{-1}, extruded at low ram speed (10 mm.min^{-1}) and dried at 105^{o}C was used in the 3D model developed and is shown in Figure 5.2.

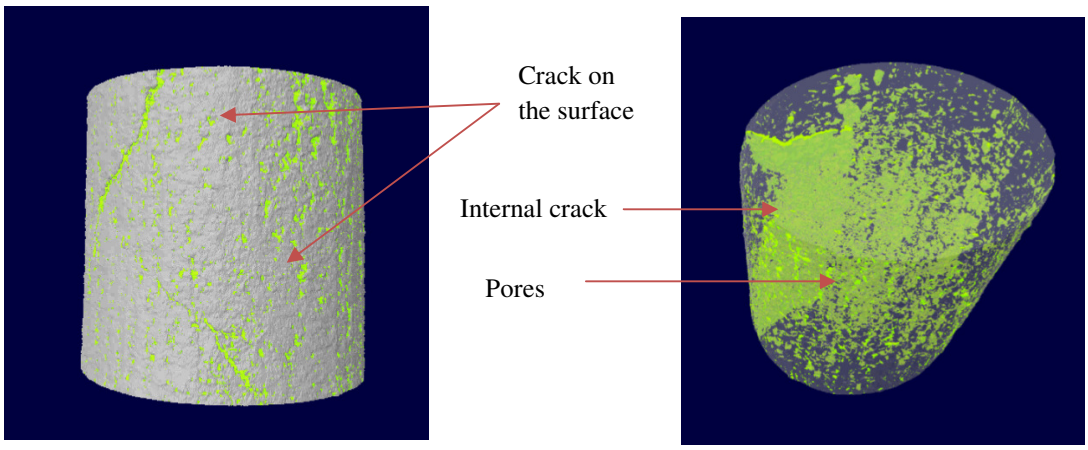

Figure 5.1: Three dimensional model of the extrudate with an initial water content of 0.92 kg water.kg solid^{-1}, extruded with a speed of 10 mm.min^{-1} and dried at 105^{o}C with the fluidised bed dryer. (Voids = green; Structure = grey).

The threshold range applied for the voids was chosen to be between 0 and 36, as the spatial distribution is more visible within the specific range, revealing a non-uniform distribution of the voids within the extrudate. Figure 5.1 also reveals the presence of a profound crack extending from the surface to the core along the vertical axis. That crack is characterised by a specific flat shape with sharper ending, and it measured to be 20 µm wide and 3 mm long. Smaller external and internal cracks can also be visualised in the above figure.

5.2.3 External cracks

A shadow image and a cross section of the extrudate with initial water content 0.92 kg water.kg solid^{-1}, extruded at low ram speed (10 mm.min^{-1}) and dried at 105^{o}C is shown in Figure 5.2.

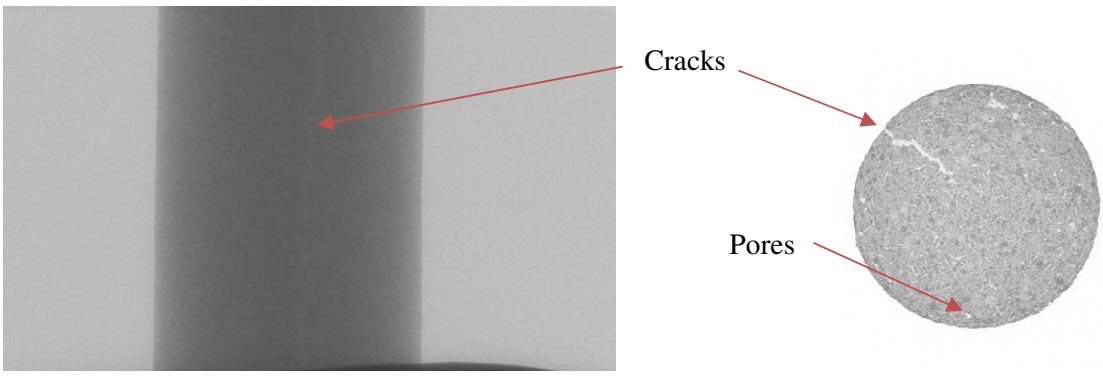

Figure 5.2: Extrudate with initial water content of 0.92 kg water.kg solid^{-1}, extruded at 10 mm.min^{-1} with a ram extruder and dried at 105^{o}C with a fluidised bed dryer (left: projected image; right: cross sectional image).

A large crack of 25 µm thickness and 3 cm length is visualised in both the shadow image and the cross sectional image. The crack did grow along the vertical axis, the direction of the ram, when dried in the fluidised bed dryer. During the experiments, the convective hot air dryer made the samples, which were in contact with the device by only one side, to oscillate without being able to invert. The vibration may have created weak points in the paste, and subsequently initiated crack development. The formation of external cracks of this type may be visible during the drying process. It would be possible to test this hypothesis by recording the drying process within the fluidised bed dryer.

5.2.4 Internal cracks

A reconstructed vertical sectional image of a cracked alumina extrudate using the Skyscan 1072 device and a cross section at a specific height Z1 is shown in Figure 5.3.

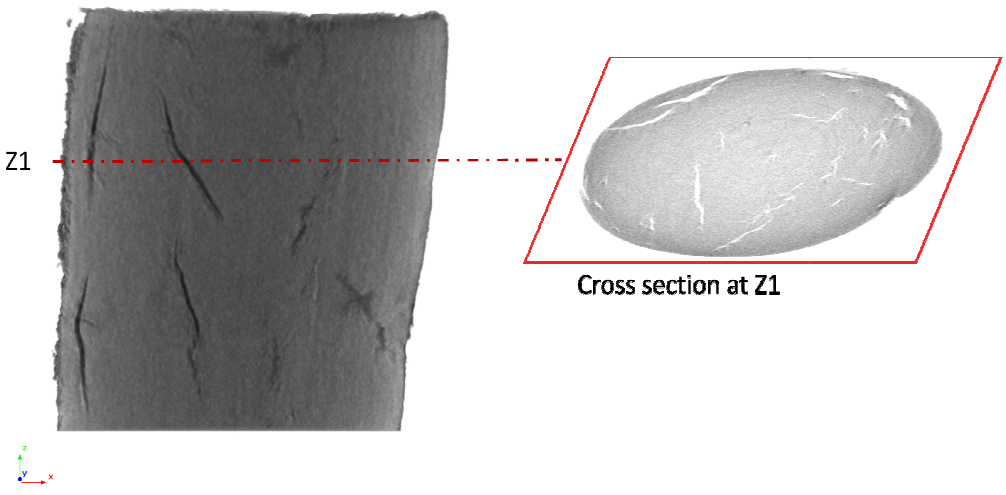

Figure 5.3: Reconstructed vertical sectional image of a cracked alumina extrudate using the Skyscan 1072 device and the cross section at a specific height Z1.

The vertical section shows the presence of internal cracks in the extrudate, which look like flat cores with sharp extremities. It appears that there is no specific point of their initiation and development, as there is no uniform distribution of the cracks throughout the sample. However, the growth of the failures tends to follow the extrusion direction. Another reason for the crack formation might be attributed to the state of stress at the centreline in the deformation zone of the die.

5.3 Effect of the processing condition on the voids size distribution

After analysing the voids qualitatively with the reconstructed images as a support, a full 3-D analysis allowed their quantification. Figure 5.4 shows the effect of the water content on the void thickness distribution of samples under the two extreme conditions of ram speed and drying method. Figure 5.4 A) illustrates the sample extruded at 10 $mm.min^{-1}$ ram speed and dried at room temperature, whereas Figure 5.4 B) shows the sample extruded at 50 $mm.min^{-1}$ ram speed and dried at 105^{o}C.

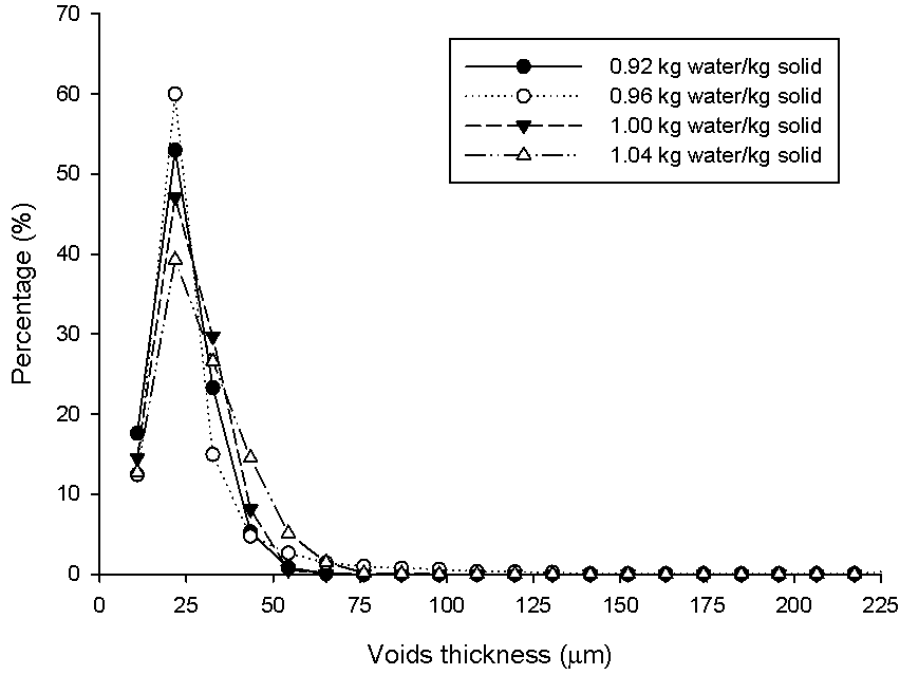

A)

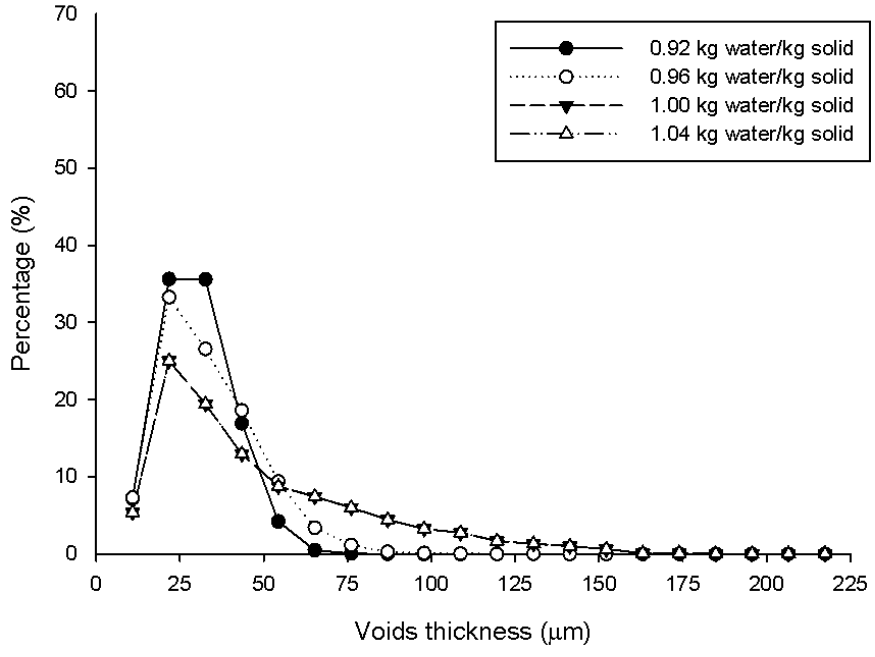

B)

Figure 5.4: A) Effect on the initial water content on the void thickness of catalyst after extruding the paste with 10 mm.min^{-1} ram speed and dried at room temperature (25^{o}C); B) Effect on the initial water content on the voids thickness of catalyst after extruding the paste with 50 mm.min^{-1} ram speed and dried at 105^{o}C with the fluidised bed dryer.

Both figures clearly demonstrate that the voids' size changes with the processing condition applied. The thickness of the majority of voids is between 20 and 35 µm, based on the resolution of 5.5 µm. In both cases, Figure 5.4 A and B, it appears that void thicknesses tends to increase with increasing water content. Indeed, the percentage of voids having 75-200 µm thickness size is higher with increasing water content. When comparing Figures 5.4 A and B, the thickness increases drastically with the ram speed and the drying temperature, between the range of 75 and 160 µm. Comparing the effect of the two parameters, temperature seems to have a greater impact on the development of voids, which is confirmed by the reconstructed images. Thus, the increase of water content and drying temperature leads to the creation of voids, which consequently leads to the reduction of the catalyst's mechanical strength (Couroyer et al., 2000). In order to limit the creation of large voids or the initiation of cracks, a decrease in the drying rate is required, which in turn leads to a reduction of the moisture gradient inside the paste (Doymaz, 2013). The pore and crack size is directly proportional to the drying temperature (Bashaiwoldu et al., 2004). Indeed, the evaporation of water can induce the collapse of the structure, creating shrinkage and subsequent failure due to cracking (Perego et al., 1997).

5.4 Characterisation of cracks

Thus far, the void distribution has been characterised qualitatively and quantitatively. The objective of this chapter is to detect and characterise cracks alone within the catalyst structure, making the separation of pores from cracks a challenging task.

Four different geometries of pores were estimated by Kaneko et al. (1994), such as the cylinder, cone-shape, slit-shape and ink bottle. Klein et al. (2004) modelled the mechanical behaviour and the failure mode based on two different crack geometries, shown in Figure 5.5.

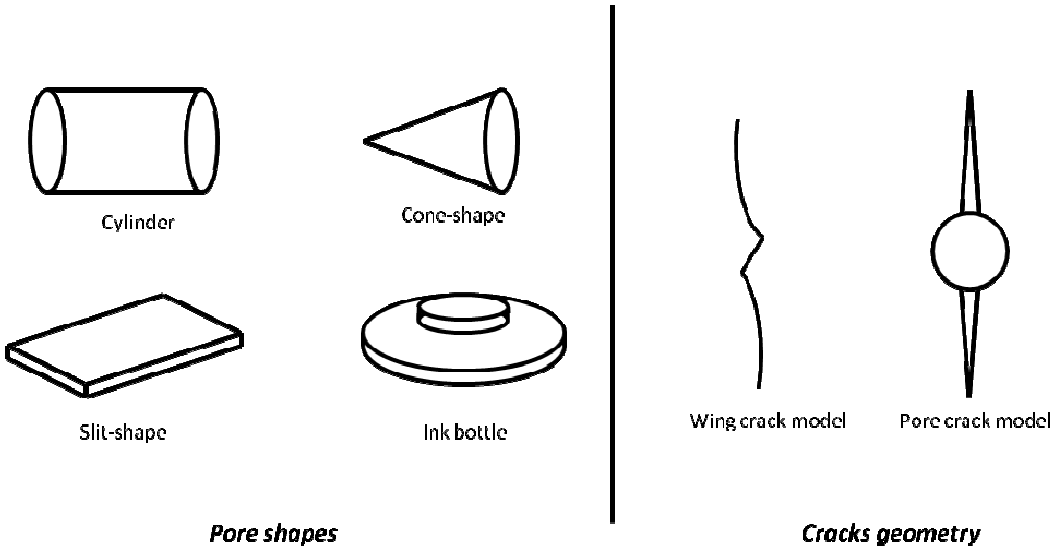

Figure 5.5: Drawing of pore shapes (Kaneko et al., 1994) and cracks geometry (Klein et al., 2004).

The wing crack model involves the growth of a secondary crack which starts from the tips of 2 other cracks, whereas the pore crack model involves the development of an axial crack from cylindrical pores (Kaneko et al., 1994).

In the following work, each void was considered to be a unique object. Then, a 3-Dimensional individual object analysis was performed in order to distinguish pores and cracks. The CT-Analyser software provides the option of characterising objects according to their shape, based on the Structure Model Index.

The Structure Model Index (SMI) is a criterion based on the morphological shape of the object. The SMI is a parameter used for quantifying the characteristic form of 3-D individual objects in terms of their plate-like or rod-like nature The SMI value is determined by the 3-D individual object analysis on the micro-Computed Tomography data. Cracks and pores can be distinguished by their SMI value. Crack is defined as an object having an elongated shape (Ammouche et al., 2001) whereas other voids have a round shape. According to Olaf Dossel and Wolfgang Schlegel (2009), SMI values smaller than 1 refer to cracks.

In order to validate and apply their observations to this work case, three different SMI values close to 1 are taken and then three different 3-D individual object models are produced. A preliminary experiment is done with the extrudate having 0.92 kg water.kg solid^{-1} water content, extruded at low ram speed (10 mm.min^{-1}) and dried at 105^{o}C using the fluidised bed dryer, as shown in Figure 5.6.

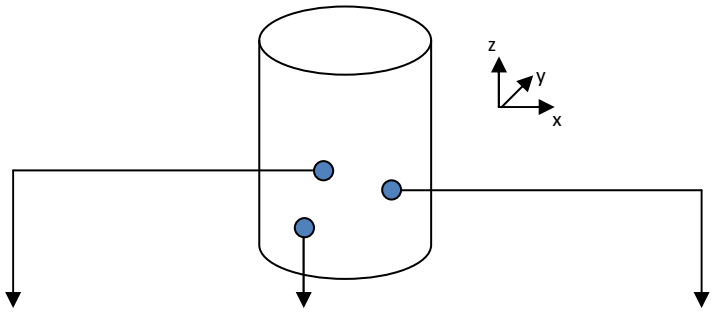

SMI Value = 0.831	SMI Value = 0.979	SMI Value = 1.169
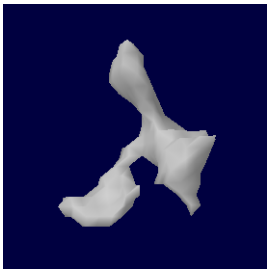		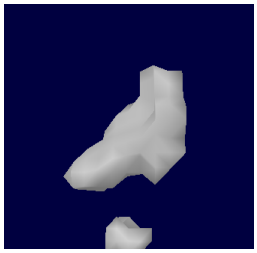
Characteristic of the object : Volume = 911,540 um^3 Surface area = 114,723 um^2 Porosity = 0.0793	**Characteristic of the object :** Volume = 5,506,667 um^3 Surface area = 666,478 um^2 Porosity = 0.0649	**Characteristic of the object :** Volume = 1,506,053 um^3 Surface area = 185,354 um^2 Porosity = 0.2404

Figure 5.6: Example taken from the extrudates with the initial water content paste of 1.04 kg water.kg solid^{-1}, extruded at 50 mm.min^{-1} ram speed and dried at 105^{o}C with the fluidised bed dryer.

The three objects shown in Figure 5.6 may be distinguished by their shape and their tips. By inspection of the shape and the extremity of the object, it is evident that those having a sharp ending are assigned at an SMI value below or equal to 1. This observation is confirmed by Hidlebrand et al. (1997). Therefore, all objects having an SMI value equal to or less than 0.979 will be considered as a crack in the following sections.

However, care is needed at this stage because all results obtained from the shape and structure of the object are dependent on the threshold applied in the image processing. Consequently, the number of cracks is partially dependent on the segmentation of the image, which is the most subjective part of the work.

Specifying the SMI value, it was possible to determine the number of cracks according to the SMI distribution. The extrudate of 1.04 kg water.kg solid^{-1} initial water content, extruded at 50 mm.min^{-1} ram speed and dried at 105^{o}C using the fluidised bed dryer is taken as an example and shown in Figure 5.7.

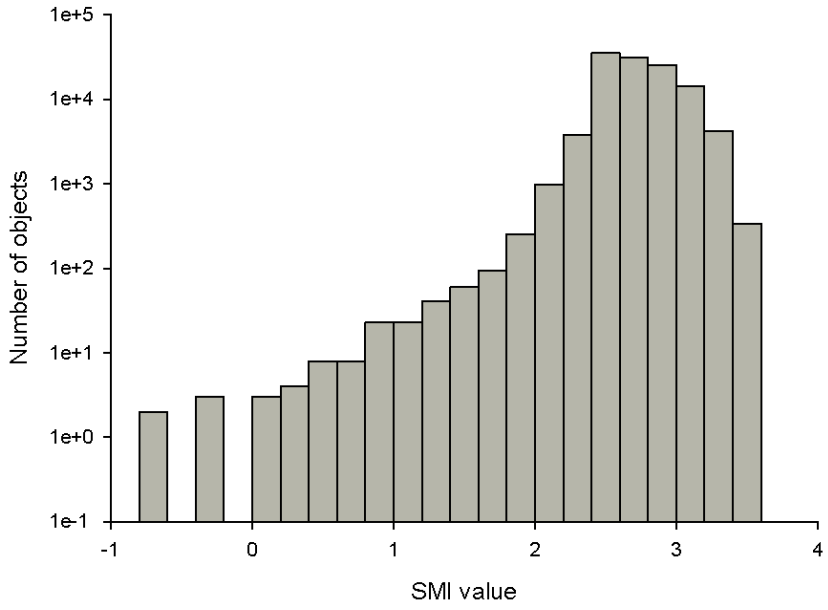

Figure 5.7: Structure Model Index (SMI) distribution of voids within a catalyst support produced from a paste of 1.04 kg water.kg solid^{-1} initial water content extruded at 50 mm.min^{-1} ram speed and dried at 105^{o}C with the fluidised bed dryer.

The SMI may have a negative value, indicating that the surface of the object is concave as opposed to convex.

The SMI distribution illustrated in Figure 5.8 provides two pieces of information:

- Objects are generally of oval geometry;
- fewer objects were considered to be cracks as compared to the pores

Therefore, based on the SMI value fixed for cracks and the segmentation of the image (threshold= 0-33), it has been found that the catalyst support has 44 cracks. The effect of different processing conditions on number of cracks inside a volume of interest was determined and analysed.

5.5 Effect of the processing condition on the development of cracks

5.5.1 Effect on the number of cracks

The same analysis was performed and extended for each processing condition. Two samples per each set of experimental condition were analysed for detecting cracks. The averages of the number of cracks for the two extreme conditions are shown in Figure 5.8.

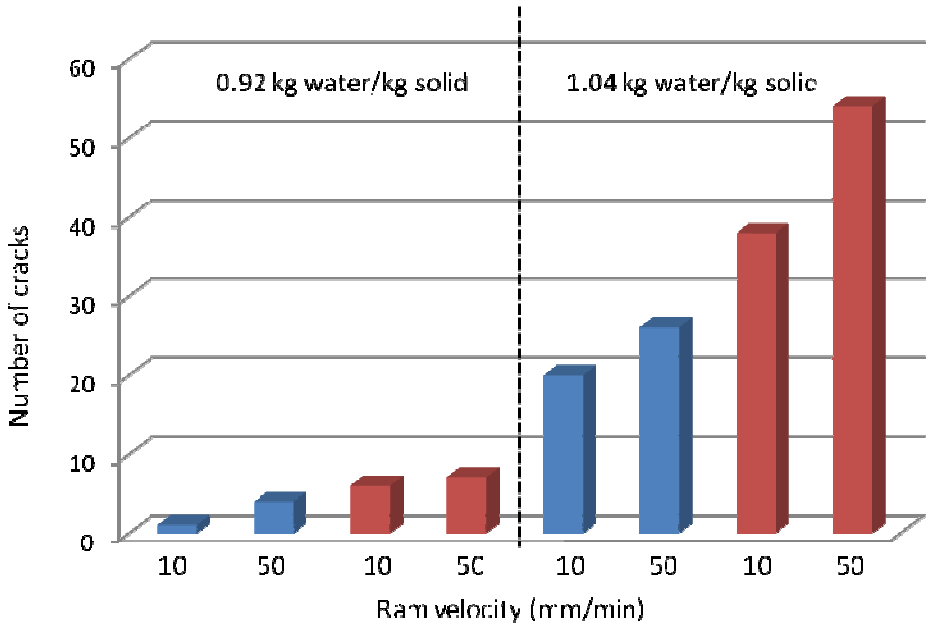

Figure 5.8: Average of the number of cracks having a SMI value below to 1 for the catalyst support having 0.92 and 1.04 kg water.kg solid^{-1} (in blue = extrudate dried at 25^{o}C and in red = extrudate dried at 105^{o}C).

Figure 5.8 shows that the water content, the ram speed and the drying temperature have a significant effect on the number of cracks, which increase with increasing the water content level, ram speed and drying temperature. For a ram speed of 10 mm.min^{-1}, a water content of 0.92 kg.kg solid^{-1}, and a drying temperature of 25^{o}C, only one crack was counted, whereas 26 cracks were observed at 1.04 kg water.kg solid^{-1}. Overall, the number of cracks increases by 75-96% between 0.92 and 1.04 kg water.kg solid^{-1}. The ram speed seems to have no effect at low water content, but the impact of that speed could be observed at a higher water content level, especially when the drying temperature was a factor. This increase is explained by the high moisture gradients inducing high stresses, resulting in paste shrinkage and creation of cracks from the surface to the core. Thus, a slower drying procedure may help produce catalysts with fewer defects (Subero-Courroyer, 2005). The drying process can induce crack

initiation when the drying rate is too fast (Pourcel, 2007). The increase of the drying temperature and the water content shows a negative impact on the quality of the catalyst support, in terms of crack initiations.

5.5.2 Effect on the surface area of the cracks

Figure 5.9 shows the average and the maximum surface area distribution of cracks for each experimental condition: A) ram speed = 10 mm.min^{-1}; B) ram speed = 50 mm.min^{-1}.

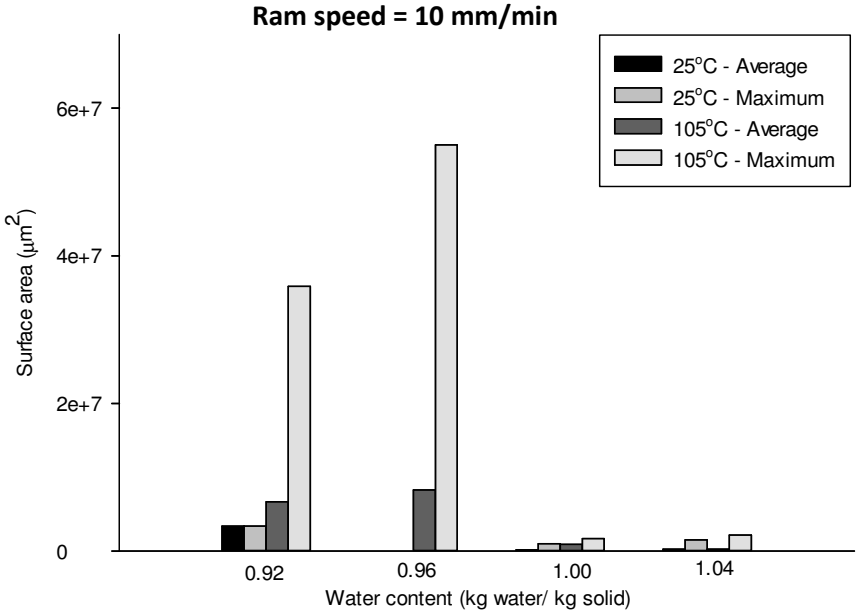

A)

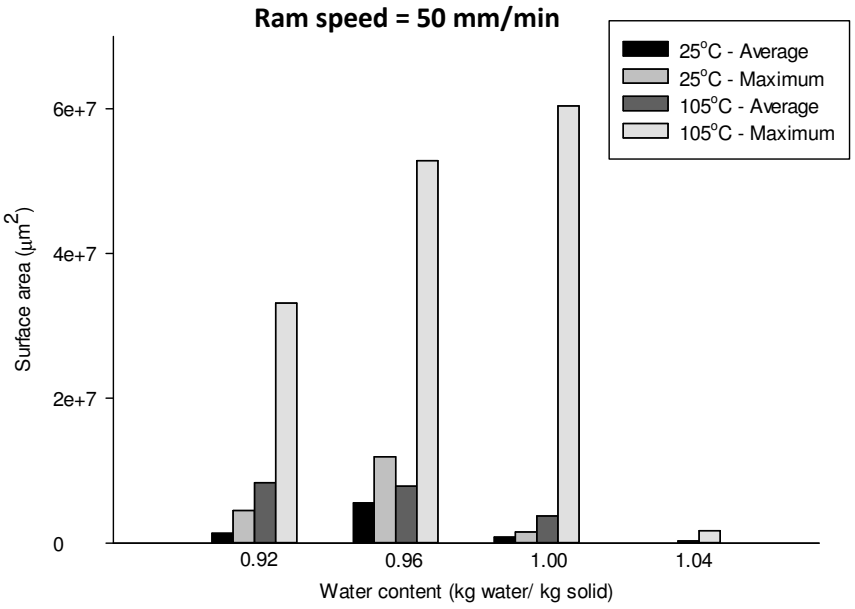

B)

Figure 5.9: Average and the maximum surface area distribution of cracks for each experimental condition: A) ram speed = 10 mm.min^{-1}; B) ram speed = 50 mm.min^{-1}.

In both graphs, the drying temperature shows an impact on the surface area of cracks, as the surface area increases with increasing the drying temperature. Parallel to that observation, the average surface area increases significantly up to a threshold value of water content, depending on the ram speed applied. Indeed, the surface area reduces drastically for a paste with a water content of 1.00 kg water.kg solid^{-1} and extruded at 10 mm.min^{-1} ram speed and for a paste of 1.04 kg water.kg solid^{-1}, extruded at 50 mm.min^{-1}. That means that either the ram speed of the extruder or the interaction of the ram extruder with the water content influences the surface area the most. When looking at Figure 5.10, the two pastes with the different water content, shows a large crack of 60.4 x10^6 µm^2 and 1.7 x10^6 µm^2 surface area, respectively.

5.6 Effect of the calcination process

After investigating the effect of the drying process on the cracks for each experimental condition, the calcination process is tested. All samples were placed in a furnace and were calcined at the temperature of 550^{o}C for 4 hours; the samples were scanned before and after the calcination. In order to compare the data accurately, one sample per processing condition was taken. Five criteria were tested in order to study the effect of the calcination:

- the diameter
- the void size
- the crack size
- the number of cracks and
- the surface area.

5.6.1 Effect on the diameter

Catalyst supports for each processing conditions were scanned before and after the calcination process. The diameter was measured and listed in Table 5.2.

Table 5.2: Measurement of the diameter of the catalyst support before and after calcination.

Water content	Ram speed	Drying process	Diameter before calcination (cm)	Diameter after calcination (cm)	Decrease of the diameter (%)
0.92 kg water/kg solid	10 mm/min	25°C	4.754 +/- 0.054	4.517 +/- 0.044	5
		105°C	4.794 +/- 0.037	4.636 +/- 0.029	3
	50 mm/min	25°C	4.740 +/- 0.024	4.535 +/- 0.052	4
		105°C	4.794 +/- 0.014	4.588 +/- 0.035	4
0.96 kg water/kg solid	10 mm/min	25°C	4.757 +/- 0.065	4.539 +/- 0.017	5
		105°C	4.729 +/- 0.042	4.538 +/- 0.024	4
	50 mm/min	25°C	4.766 +/- 0.051	4.477 +/- 0.043	6
		105°C	4.809 +/- 0.027	4.549 +/- 0.016	6
1.00 kg water/kg solid	10 mm/min	25°C	4.671 +/- 0.017	4.535 +/- 0.034	3
		105°C	4.719 +/- 0.036	4.601 +/- 0.029	2
	50 mm/min	25°C	4.745 +/- 0.034	4.508 +/- 0.040	5
		105°C	4.824 +/- 0.041	4.657 +/- 0.025	3
1.04 kg water/kg solid	10 mm/min	25°C	4.698 +/- 0.029	4.514 +/- 0.034	4
		105°C	4.791 +/- 0.020	4.541 +/- 0.024	5
	50 mm/min	25°C	4.721 +/- 0.037	4.546 +/- 0.031	4
		105°C	4.802 +/- 0.053	4.658 +/- 0.052	3

From Table 5.2 it can be observed that there was a decrease of the diameter of all catalyst supports by 3-6%. The reduction of the size of the sample after calcination might be due to the change of the internal structure resulting from the reduction of pore size. It also appeared that there is no relation between processing condition and shrinkage of the extrudate, as the difference in percentage is not significant.

5.6.2 Comparison of the void size distribution

The quantification and the comparison of the void size before and after the calcination process was performed by a full 3-D analysis. Figure 5.10 shows the effect of the sample prepared with 1.04 kg water.kg solid^{-1} on the voids thickness distribution for samples dried under both

sets of conditions. Figure 5.10 A) shows the sample was extruded at 10 mm.min^{-1}, whereas Figure 5.10 B) shows for a sample extruded at 50 mm.min^{-1}.

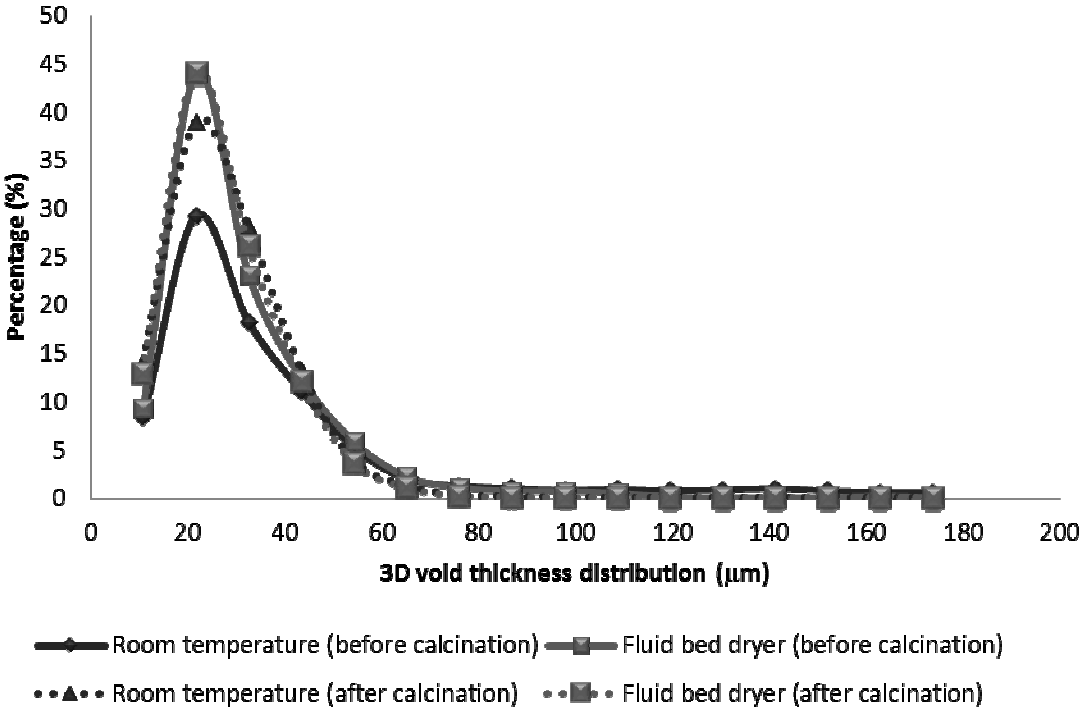

(A)

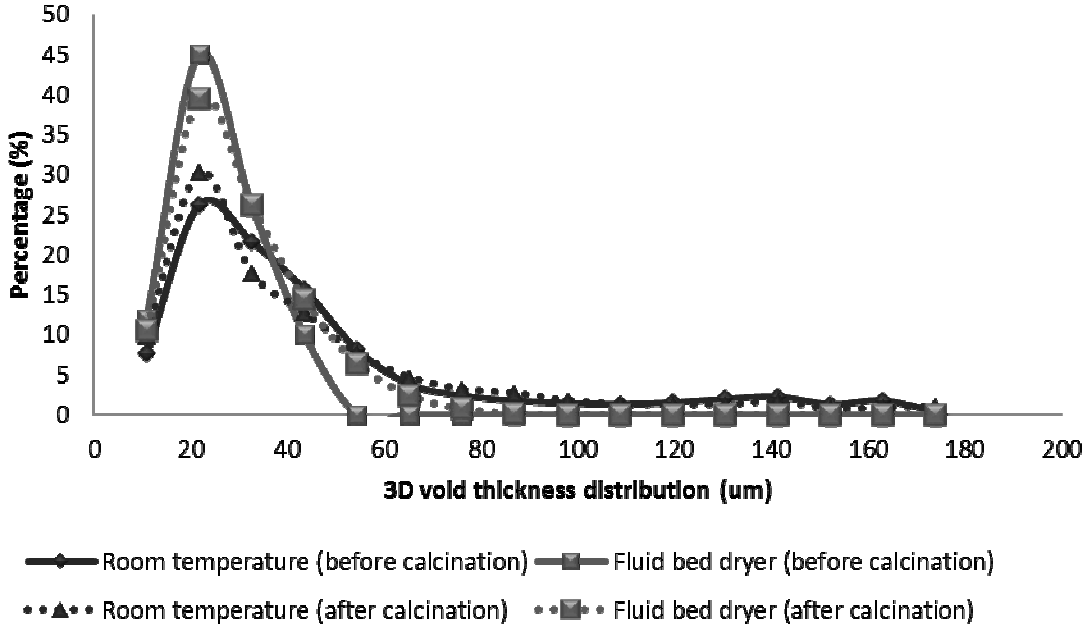

(B)

Figure 5.10: Effect of the calcination process on the void thickness distribution with a sample initially prepared at 1.04 kg water.kg solid^{-1} after different drying process. A) Catalyst support extruded at 10 mm.min^{-1}; B) Catalyst support extruded at50 mm.min^{-1}.

Figure 5.10 shows that the calcination process changes the porosity of alumina extrudates by increasing the voids thickness. In both figures, the effect of the drying condition can be observed. At a thickness range of 20-40 µm, the calcination process increases the percentage of voids when the sample was dried at room temperature, whereas the percentage decreases after drying the sample in the fluidised bed dryer. Above the value of 40 µm, the void thickness does not change at 10 mm.min^{-1} ram speed. However, the combination of high ram speed and high drying temperature has a significant effect on the porosity of the sample, as the calcination process increases the percentage of voids. The change in void size distribution can be due to the fact that the calcination process induces shrinkage of the paste (see Chapter

5.6.1), which might also change the structure of voids, such as the shape and the size. The voids could not be visualised and characterised without the calcination process, as their sizes were below the pixel size applied for that set of experiments (5.5 µm).

5.6.3 Qualitative determination of crack size

As shown described in Chapter 5.5.1., pores and cracks are distinguished by their SMI. To characterise the impact of the calcination process by a qualitative approach, the largest crack of the sample is selected. Figure 5.11 shows a 3-D model of that crack before (Figure 5.11 A) and after calcination (Figure 5.11 B).

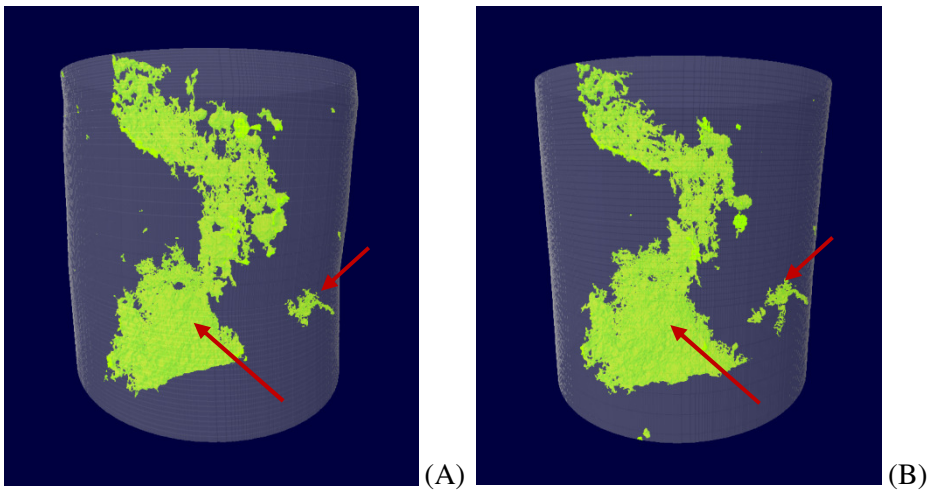

Figure 5.11: 3-D model of the largest crack within the material, A) before calcination; B) after calcination. Example taken from the extrudate with initial water content of 1.00 kg water.kg solid^{-1}, extruded at 50 mm.min^{-1} with a ram extruder and dried at 105^{o}C with a fluidised bed dryer.

By comparing the 3-D model of the crack before and after the calcination, it is observed that the crack increases in size with calcination. The biggest crack was measured using the Image J software resulting in a 121 ± 10 μm thickness and 1950 ± 26 μm length, and 159 ± 8 μm thickness and 1990 ± 34 μm length for the crack before and after calcination, respectively.

5.6.4 Effect of the calcination on the number of cracks

To quantify the number of cracks in the sample, the SMI method is used. An individual 3-D analysis was done for each processing condition before and after calcination. The following results were obtained in Table 5.3.

Table 5.3: Number of cracks within the sample before and after the calcination at 550°C for 4 hours for each processing condition.

Water content	Ram speed	Drying process	Number of cracks (SMI<1)	
			Before calcination	After calcination
0.92 kg water.kg solid^{-1}	10 mm.min^{-1}	25 °C	0	0
		105 °C	0	4
	50 mm.min^{-1}	25 °C	3	3
		105 °C	0	0
0.96 kg water.kg solid^{-1}	10 mm.min^{-1}	25 °C	2	8
		105 °C	3	4
	50 mm.min^{-1}	25 °C	3	11
		105 °C	0	6
1.00 kg water.kg solid^{-1}	10 mm.min^{-1}	25 °C	21	23
		105 °C	0	21
	50 mm.min^{-1}	25 °C	14	14
		105 °C	18	19
1.04 kg water.kg solid^{-1}	10 mm.min^{-1}	25 °C	11	12
		105 °C	1	7
	50 mm.min^{-1}	25 °C	8	10
		105 °C	20	26

By comparing the sample before and after the calcination, a small increase in the number of cracks is observed in each processing condition. The detectability of cracks is related to the resolution of the equipment and the segmentation to a binary image. In this case, the resolution of the XRCT is 5.4 μm. Therefore, any object smaller than that pixel size cannot be detected as a void but as a pixel with a low grey value. Before calcination, the presence of nano-cracks may be obscured by the limitation of the technique. These cracks could be revealed after the high temperature processing step at 550°C. The increase of the number of cracks could be explained by the limitation of the resolution of the XRCT or the change of the void structure from a pore to a pore crack (see in Chapter 5.4).

5.6.5 Effect on the surface area of the cracks

Table 5.4 shows the average surface area of cracks and the surface area of the largest crack before and after the calcination process for different processing conditions.

Table 5.4: Surface area of cracks before and after the calcination process at different processing conditions.

			Before calcination		After calcination	
Water content (kgwater. kg solid^{-1})	**Ram speed** (mm.min^{-1})	**Drying Temperature** (^{o}C)	Surface area of cracks (Average μm^2)	Surface area of the largest crack (μm^2)	Surface area of cracks (Average) μm^2	Surface area of the largest crack (μm^2)
0.92	10	25	-	-	-	-
		105	3.5 x10^6	12.4 x10^6	4.6 x10^6	16.6 x10^6
	50	25	-	-	-	-
		105	5.3 x10^6	23.2 x10^6	10.9 x10^6	32.5 x10^6
0.96	10	25	0.4 x10^6	1.2 x10^6	0.4 x10^6	4.6 x10^6
		105	0.1 x10^6	0.2 x10^6	1.2 x10^6	1.7 x10^6
	50	25	0.5 x10^6	1.1 x10^6	1.2 x10^6	9.6 x10^6
		105	-	-	0.7 x10^6	2.1 x10^6
1.00	10	25	0.2 x10^6	16.5 x10^6	0.4 x10^6	24.1 x10^6
		105	0.2 x10^6	2.6 x10^6	0.6 x10^6	7.8 x10^6
	50	25	0.3 x10^6	1.4 x10^6	4.8 x10^6	24.6 x10^6
		105	0.3 x10^6	2.7 x10^6	0.3 x10^6	2.4 x10^6
1.04	10	25	0.2 x10^6	3.4 x10^6	0.4 x10^6	4.5 x10^6
		105	0.3 x10^6	0.3 x10^6	0.4 x10^6	1.8 x10^6
	50	25	0.4 x10^6	0.5 x10^6	0.3 x10^6	1.7 x10^6
		105	0.3 x10^6	0.7 x10^6	0.3 x10^6	0.9 x10^6

The calcination slightly increases the surface area of cracks, as the magnitude of all data is in the order of 10^6 µm. The small increase can be explained by the fact that the cracks tend to

grow while calcination process occurs and/or the cracks tend to change their structure due to the shrinkage of the paste.

5.7 Conclusion

The purpose of this chapter was to develop a methodology on how to detect and characterise cracks within the catalyst using the XRCT and then to apply the method on the investigation of the effect of water content, ram extrusion speed, drying temperature as well as the calcination process on crack initiation and propagation.

The XRCT allows the visualisation of the location of pores or cracks within the sample, as well as their directionality and their shape. The crack propagation tends to follow the direction of the extrusion process. That technique can serve as an important tool in extracting quantitative bulk properties, such as void size distributions, pore volume, and pore-size distribution in 3-D individual object analysis and full 3-D analysis.

Depending on the initial moisture content, the speed of the ram extrusion and the drying rate, the internal structure and mechanical properties of the extrudate are altered accordingly. Indeed, the void thickness increases with increasing water content, extrusion ram speed and drying rate.

Pores and cracks can be distinguished by the SMI value, which can be affected by the threshold range applied. The interaction between water content and drying conditions influences the development of cracks in terms of the total volume, the surface area and the numbers of cracks. The calcination has a positive effect on the number of cracks and their development inside the sample.

The X-Ray Computed tomography is a technique, which provides only a "snapshot" on the internal structure of a material for a given time. The use of synchrotron can overcome the problem and give a better insight of the internal structure, as it functions in micro- and nano-scale, making it highly advantageous as compared to conventional techniques. The technique is described in detail in Chapter 7.

CHAPTER 6 – DISTRIBUTION OF COPPER NITRATE TRIHYDRATE SOLUTION IN THE SUPPORT BY WET IMPREGNATION

6.1 Introduction

Supported metal catalysts are widely used in industrial processes. Such catalyst supports have advantages, such as high surface area, low amount of active components called precursors, high thermal and mechanical resistance (Ertl et al., 1999). The preparation of supported catalysts is divided into three steps: (i) deposition: filling pores with a solution containing an active component through the impregnation process; (ii) drying: removal of the solvent; and (iii) calcination: transformation of the active component into a desired form (Lee and Aris, 1985; Ertl et al., 1999).

Impregnation is a crucial step in the catalyst preparation as it is directly linked to its performance. A key part in impregnation is achieving the desired distribution of the active component, as the metal profile in the support is related to catalytic performance (Heise and Schwartz, 1987). As discussed in Chapter 2.4, four different metal profiles are reported, such as uniform, egg-shell, egg-yolk and egg-white (Gavriilidis et al., 1993; Shyr and Ernst, 1980). A desired metal distribution is dependent upon the impregnation parameters selected, such as active species, pH and ionic strength (Lekhal et al., 2004; Papageorgiou et al., 1996). The

metal distribution could be controlled by the impregnation itself, however the drying process may also have an impact on its distribution within the support (Komiyama et al., 1980).

Imaging techniques provide the possibility of visualising the distribution of the metal within the catalyst at different length scales. Transmission electron microscopy (TEM) and X-ray absorption on a fine structure (EXAFS) were used to characterise the structure of copper particles after adsorption on a ZnO support (Grunwaldt et al., 2009). At a larger scale, work has been done using the XRCT technique in order to study the distribution of metal oxide particles after impregnation. Grunwaldt et al. (2009) investigated the metal profile obtained after immersion a Cu/Al_2O_3 supports for different time in a $CuCl_2$ solution metal profile. Therefore, the XRCT may be suitable for visualising the deposition of the metallic compound within the catalyst after the impregnation and drying processes.

In this chapter, alumina extrudate is used as a support and copper nitrate trihydrate is used as a metallic precursor. In practice, Cu-supported alumina is used for phenol oxidation (Sadana and Katzer, 1974). From the two impregnation methods discussed in Chapter 3, the wet impregnation method was selected. The preparation of the alumina support and the impregnation technique is detailed in Chapter 3. The visualisation and the investigation of the metal profile distribution within the catalyst support using the XRCT may assist in the development of an understanding the deposition technique of copper species in order to improve the performance. The parameters investigated were the concentration of the bulk solution, the impregnation time and the drying conditions.

6.2 Characterisation of metal profile by using XRCT

The purpose of this chapter is to investigate the potential of the XRCT to visualise and characterise the copper distribution in alumina support. Preliminary experiments were conducted in order to test the effectiveness of XRCT in visualising the impregnation front of saturated copper nitrate trihydrate solution at a 5 % concentration.

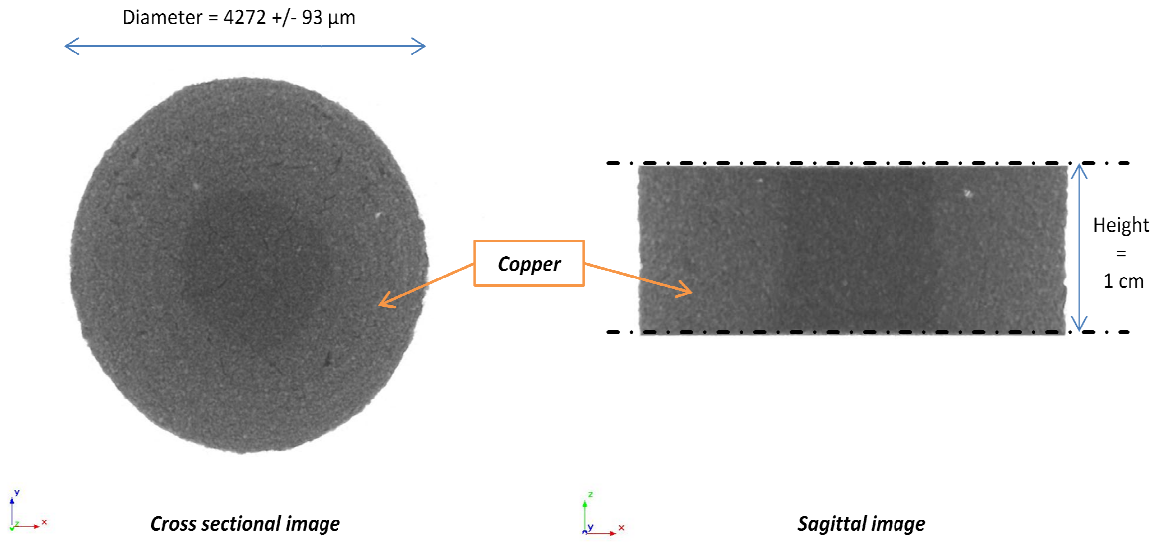

Figure 6.1: Egg-shell profile in alumina extrudate. Example taken with extrudate dipped in bulk solution saturated at 5% for 5 min and dried at room temperature overnight.

Figure 6.1 shows the copper distribution inside alumina support after being impregnated for 5 min. An egg-shell distribution is characterised by the impregnation front, revealing the presence of copper. Therefore, it is possible to distinguish copper from alumina, even if the concentration of copper nitrate trihydrate is very low.

6.3 Relation between impregnating solution and impregnation time

6.3.1 Viscosity of the copper nitrate trihydrate solution

The viscosity of copper nitrate trihydrate solutions saturated at 5 % and 90 % was measured. The protocol is detailed in Chapter 3. Results show that those solutions exhibit Newtonian behaviour, as the viscosity is independent of shear rate γ (= 1-10 s^{-1}). The viscosities for 5 % and 90 % saturated impregnating solutions at room temperature (20^{o}C) are 1.18 x 10^{-3} and 5.5 x 10^{-3} Pa.s, respectively.

6.3.2 Uptake of impregnation solution by the support

To characterise the copper nitrate trihydrate uptake, an extrudate is immersed in the saturated solution of either 5% or 90%, and is weighed at 1 minute intervals during the first five minutes and at 15 minutes intervals during the rest of the experiment, until 100 min. The alumina support is cylindrical with a 4.272 ± 0.053 mm diameter and 10 mm length. The initial mass of each extrudate was 0.17 ± 0.1 gram and the experiment was repeated 3 times at room temperature. Figure 6.2 shows the uptake of copper nitrate trihydrate solutions (5 and 90%) by the catalyst support.

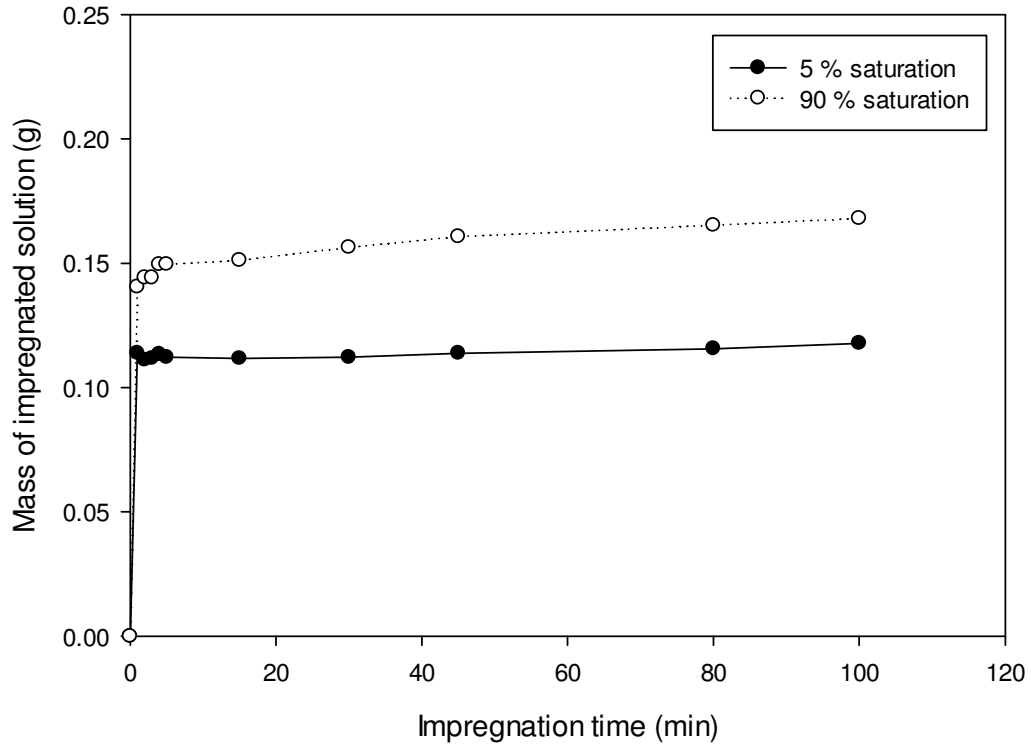

Figure 6.2: Uptake of the copper nitrate trihydrate solution saturated at 5% and 90% by the alumina extrudate.

Figure 6.2 indicates that the uptake of copper nitrate trihydrate solution by the catalyst support occurs within the first 5 seconds after dipping the sample, irrespective of the concentration of the bulk solution. Within one minute, the mass of the metallic solution absorbed by the catalyst support is about 0.118±0.005 g for a solution saturated at 5%, and 0.142±0.009 g for a solution saturated at 90%. Therefore, 95% of the metal uptake by the catalyst support occurred at the early stage of impregnation. Between 1 and 5 minutes, the metal loading is still visible when the solution is highly saturated (90%), due to higher viscosity, while the uptake of the metallic solution is null for a solution saturated at 5%. After 5 min, the uptake seems to have been stabilised with the presence of the plateau. Catalyst supports were dry

before being immersed in the solution. When the bulk solution (fluid) penetrates the pores, the air inside the pores is entrapped and compressed. The fluid penetration stops when the capillary pressure is equal to the pressure of the air (Lekhal et al., 2001). Therefore, the impregnation process cannot be completed. In the case of dry samples, pores are often evacuated or filled with soluble gases (Lekhal et al., 2003). At that time, the existence of small uptakes of copper nitrate trihydrate solution by the support is thought to be due to the high tortuosity of pore network. Therefore, active components might exhibit some difficulty in travelling through narrow pore connexions and to fill nano-pores.

The uptake of the highly saturated bulk solution appears to be higher (0.11 mL) than that of the lower saturated solution (0.096 mL). In Figure 6.2, the calculated weights of the bulk solution absorbed by the alumina support are shown.

6.4 Effect of the impregnation time

Metal loading is related to the porosity of the catalyst support. Open pores are typically involved in the process of impregnation.

Dried alumina supports were immersed in the saturated solutions (5% or 90%) at different impregnation times (5 sec, 5 min and overnight) and were then removed and cut into half, along the cross-section. The samples were scanned at different impregnation times, after being dried, as when wet they could not be scanned due to the instability of the solution. The cross sections and their respective schematics are shown in Figure 6.3.

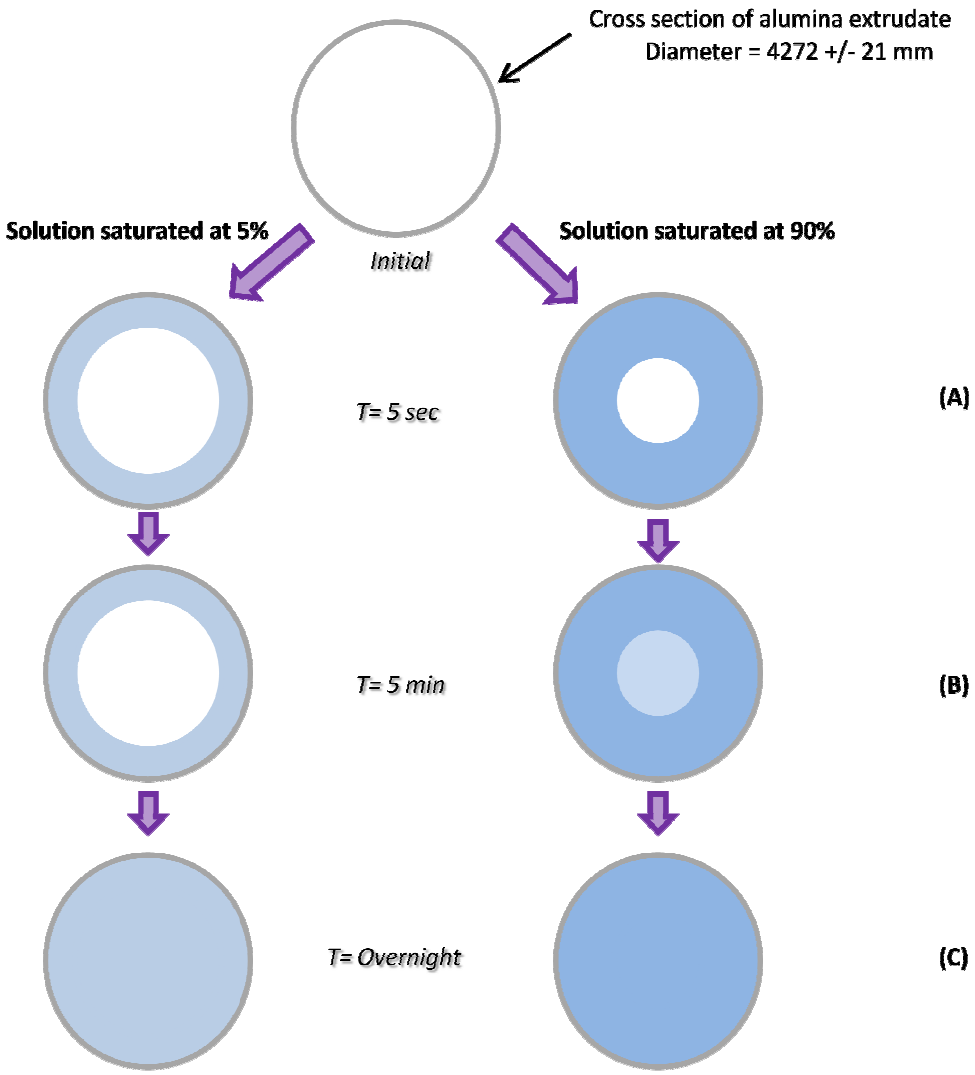

Figure 6.3: Schematics of alumina supports after being immersed in a solution saturated at 5 % (on the left) and in a solution saturated at 90% (on the right) for different time (0 s, 5 s, 5 min and overnight).

The distribution of the metallic solution could be visualised, as copper nitrate trihydrate has a characteristic blue colour. It can be observed that the impregnation front moves towards the core of the catalyst and the dissolved active components move due to the effect of capillary flow, diffusion and adsorption, which are the three steps involved in the impregnation process in the case of dried catalyst supports (Lekhal et al., 2004).

In addition, the impregnation time appears to have a significant impact on the metal distribution profile. The metal profile is shown in Chapter 2.2.5.3. As the surface of support is directly in contact with the metallic solution, the contact area between the surface and the solution is important. The impregnation solution is going to the surface of catalyst, creating an egg-shell profile, whose thickness is dependent on the concentration of the impregnation solution. After 5 seconds, the thickness of the 5% saturated solution is about 1 mm, whereas it is about 3 mm in the 90% saturated solution (Figure 6.3 A). It appears that the active species migrates into the core at 2 different speeds. Mass transfer is dependent on the concentration of the solution, which seems to increase the capillary flow inside the support.

The impregnation front moves towards the centre of the catalyst support, as the impregnation time increases. From the egg-shell profile, the metal distribution is uniform (Figure 6.3 C). The active components of the 5% saturated solution seem to diffuse faster than the 90% saturated solution from the impregnation solution, through the pore network towards the centre of the support (Figure 6.3 B).

Two phenomena appear during the impregnation: the diffusion of the solute into pores, Fick's law of diffusion (Perego and Villa, 1997), and the adsorption of the active component on the support, based on Langmuir's law (Lekhal and al., 2001; Spieker and Regalbulto, 2001). Thus, the distribution of the active components depends on the relationship between diffusion and adsorption. The slowest step determines the impregnation profile. If adsorption is faster than diffusion, impregnation front moves slowly. This is the characteristic of egg shell profile. While slow adsorption and fast diffusion gives uniform profile. At t = 5 min, the concentration of the bulk solution generates two different responses in terms of metal distribution. Fast adsorption and slow diffusion occurs at the low saturated solution (5%), whereas slow adsorption and fast diffusion is observed for high saturated solutions (90%).

6.5 Effect of drying process on the metal distribution

In order to study the effect on the drying process, samples were either dried at room temperature (25^{o}C) or at 100^{o}C for 20 min in the oven. The XRCT was set up at a voltage of 50 kV and a current of 98 µA, with 0.5 mm aluminium filter and the resolution of 5.4 µm was applied.

The following samples were scanned individually, making the density comparison between them complicated. The X-ray beam is slightly different according to the scans although the settings of the XRCT were similar. The metal distribution in alumina support could be revealed.

6.5.1 Effect of drying on the 5 % saturated copper nitrate trihydrate solution

6.5.1.1 Impregnation for 5 min

Figure 6.4 shows two cross sectional images (A) and their respective density distribution maps (B).

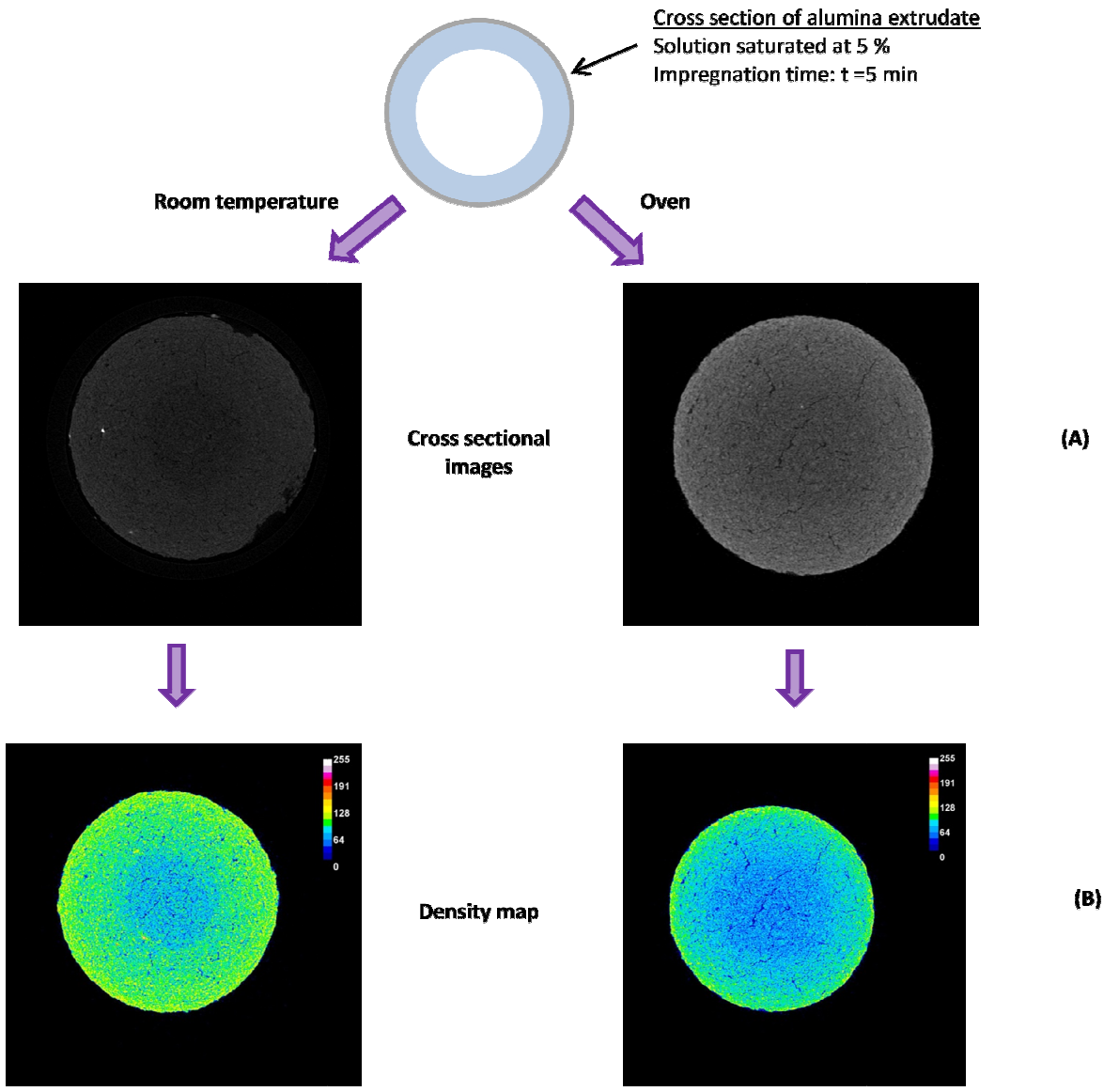

Figure 6.4: Cross sectional images (A) and its respective density distribution maps (B) showing the effect of drying condition on the metal distribution after impregnating the alumina support for 5 min in a solution saturated at 5%.

As the visualisation of density distribution could be challenging in a grey scale, the density distribution map is done for each cross sectional image. By visualising the density distribution map (Figure 6.4 B), egg-shell profile is observed with the two different drying processes. The thickness of the metal distribution varies with the drying condition; the outer shell has a

thickness 1188 ± 73 µm and 297 ± 62 µm after being dried at room temperature and at 100^{o}C, respectively. Prior to drying process, egg-shell of 1 mm thickness was initially characterised. The change of the metal distribution suggests a redistribution of active components during the drying process. Redistribution might be a consequence of desorption phenomena.

During drying, water on the surface of the support evaporates first and the liquid is transported towards the surface by capillary flow. The rate of liquid removal increased as drying temperature increased. The mass transfer of solvent also led to a transport of ions by convection and capillary flow. In fast drying processes, copper ions, which seem to be weakly interacting with the surface, tend to follow the migration of water towards the surface as the convective flow is the predominant transport mechanism (Lekhal et al., 2001). The fact that ions are accumulated at the surface and are interacting with the alumina support, it does explain the thin egg-shell profile. However, a loss of copper ions during drying was noticed, as tiny amounts of blue solution were found dried between the catalyst support and aluminium foil. This observation implies that the interaction between the copper ions and alumina support is weak. In the case of slow drying processes, the back diffusion mechanism is observed and copper ions tend to migrate towards the centre of the support. Therefore, the egg-shell thickness is greater than the observed prior to drying.

6.5.1.2 Impregnating overnight

Figure 6.5 shows two cross sectional images (A) and their respective density distribution maps (B).

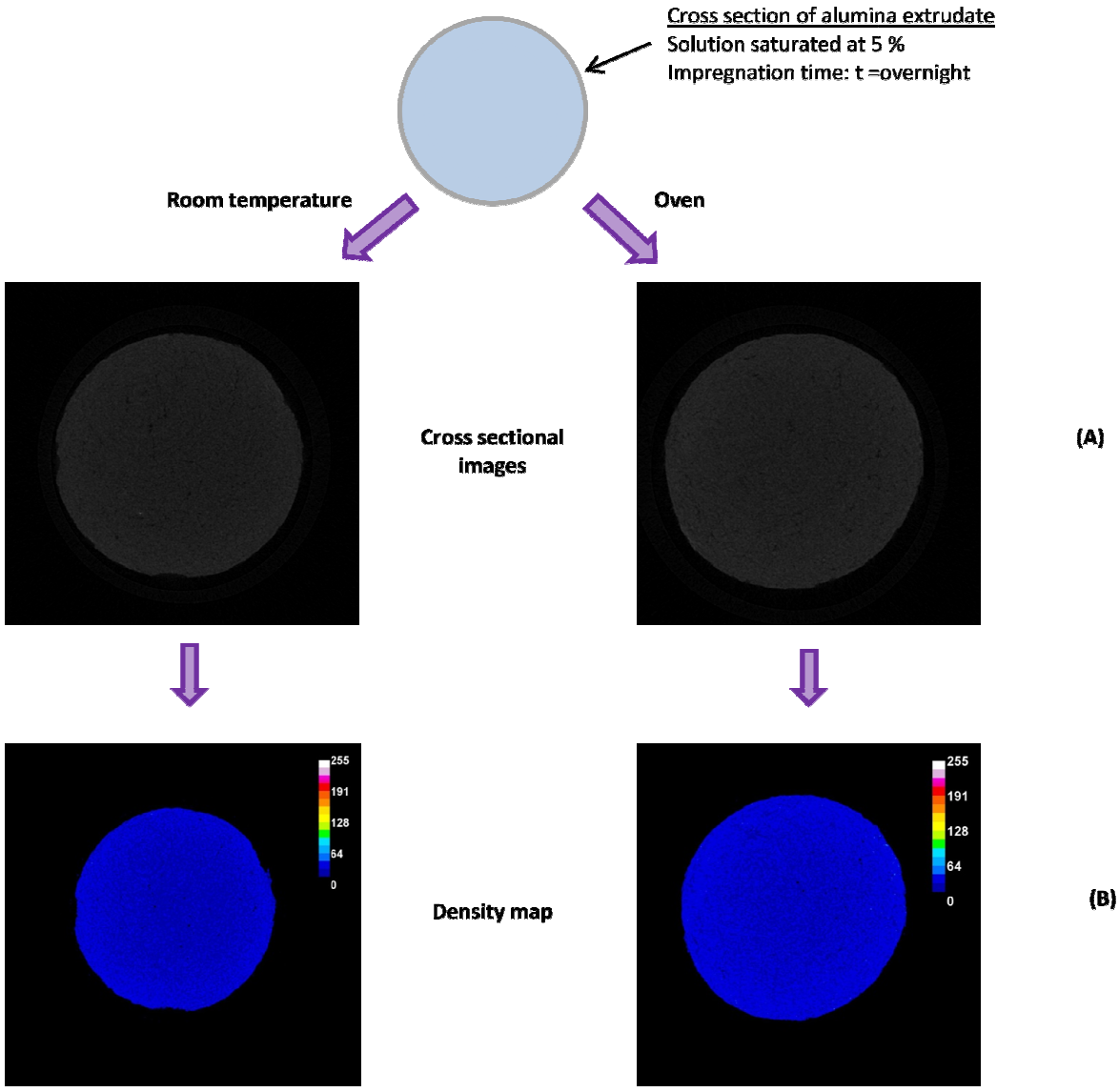

Figure 6.5: Cross sectional images (A) and its respective density distribution maps (B) showing the effect of drying condition on the metal distribution after impregnating the alumina support overnight in a solution saturated at 5%.

By visualising the density distribution map (Figure 6.5 B), a uniform profile is observed for both drying conditions. When extrudates are kept immersed in the solution overnight, the 5% copper nitrate trihydrate solution has enough time to diffuse to the pore network and allow the adsorption of the active component onto the alumina support. Drying processes do not seem

to have any influence on the metal redistribution, as the distribution of the metal is still uniform. The non-redistribution of ions suggests a strong interaction with alumina support.

6.5.2 Effect of drying on the 90 % saturated copper nitrate trihydrate solution

6.5.2.1 Impregnation for 5 min

Figure 6.6 shows two cross sectional images (A) and its respective density distribution maps (B) for alumina samples impregnated for 5 min.

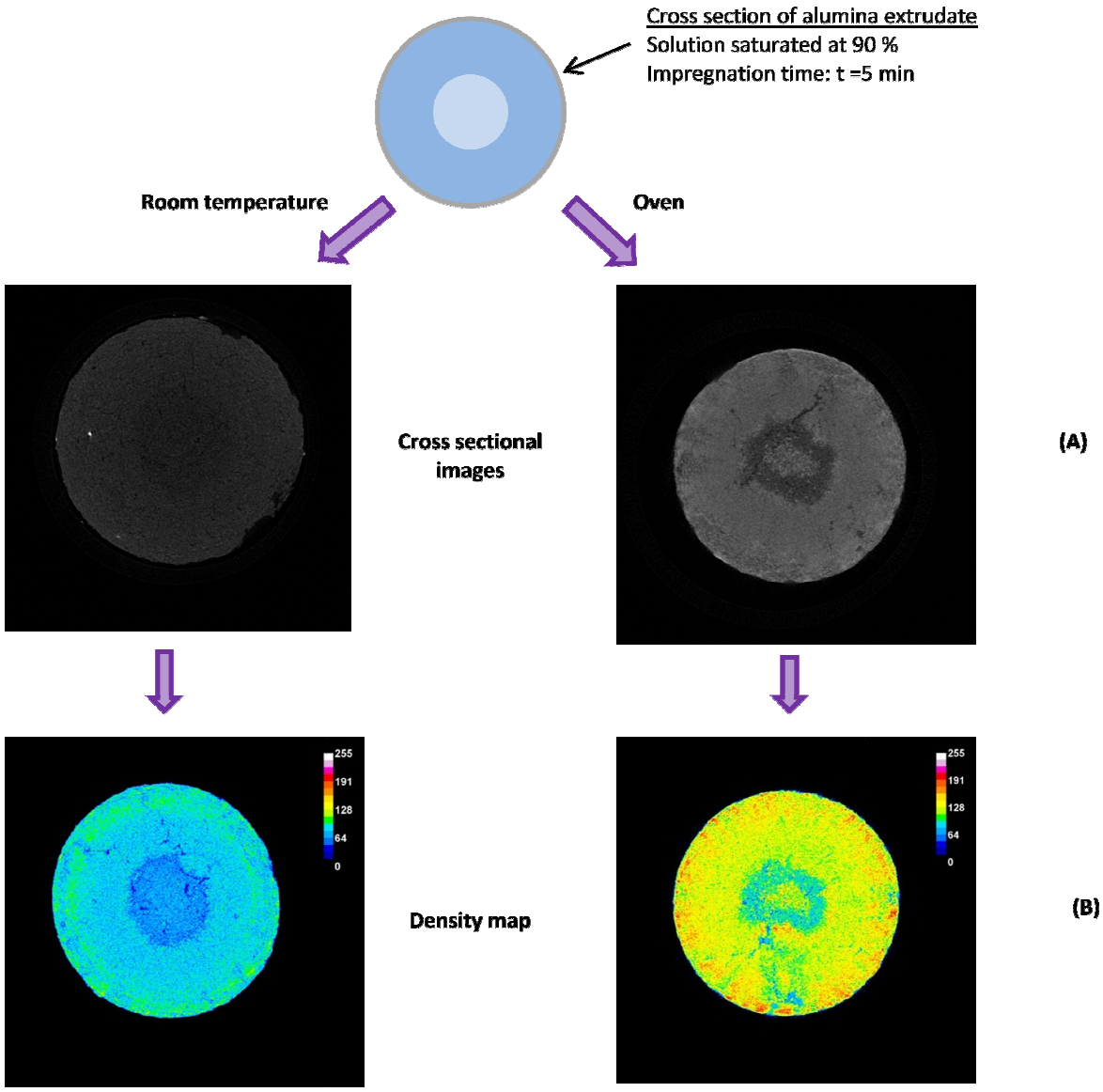

Figure 6.6: Cross sectional images (A) and its respective density distribution maps (B) showing the effect of drying condition on the metal distribution after impregnating the alumina support for 5 min in a solution saturated at 90%.

The density distribution map (Figure 6.6 B) reveal, the egg-shell and egg yolk profiles for both drying conditions. The thickness of the metal distribution is similar before and after the drying conditions are applied, showing a value of 1377±52 µm.

The slow drying process does not seem to have any significant effect on metal redistribution. The presence of a high density area close to the surface characterises the metal redistribution inside the support. However, that phenomenon is difficult to prove as the scan of alumina support before drying, at room temperature was impossible to be carried out. The drying process occur immediately after removing samples from the bulk solution. The fast drying process shows a redistribution of ions due to the presence of egg-yolk profile. During drying, the back diffusion mechanism is observed, as copper ions tend to migrate towards the centre of the support. This redistribution is a consequence of two different phenomena: (i) Interaction between copper ions and alumina support is weak. (ii) Convective flow and back diffusion are not the predominant transport mechanisms during fast drying.

6.5.2.2 Impregnating overnight

Figure 6.7 shows two cross sectional images (A) and its respective density distribution maps (B).

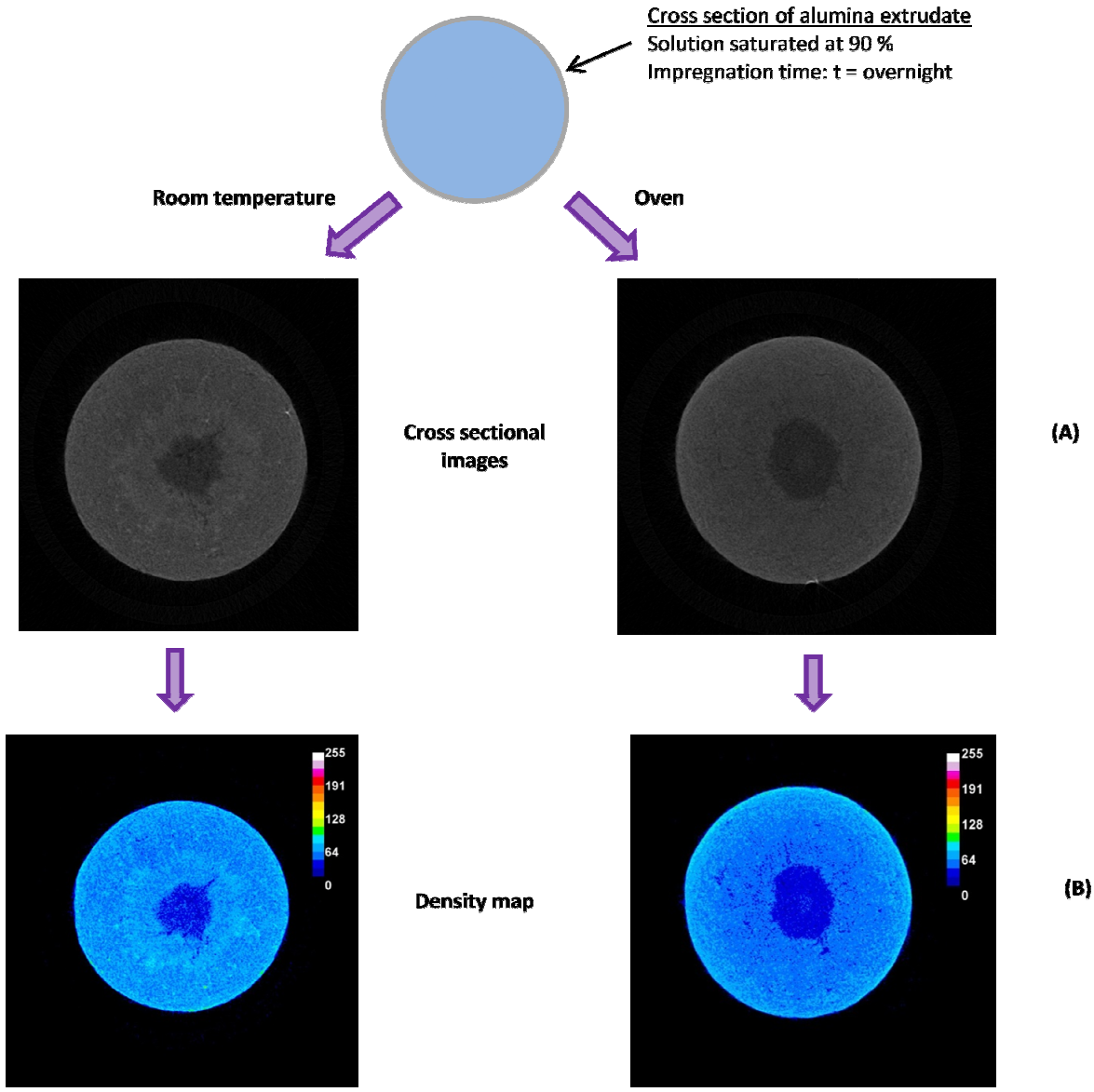

Figure 6.7: Cross sectional images (A) and its respective density distribution maps (B) showing the effect of drying condition on the metal distribution after impregnating the alumina support overnight in a solution saturated at 90%.

By visualising the density distribution map (Figure 6.7 B), the presence of an egg-shell distribution, after immersing the alumina extrudate in the solution saturated at 90% at the 2 drying conditions, is observed. In both conditions, the thickness of the outer shell is 1328 ±67 µm. Prior to the drying process, a uniform profile and a redistribution of the active species was visualised, indicating weak interaction between ions and support. In addition, the

convective flow is the predominant transport phenomenon as the ions moved towards the surface of catalyst support. In the case of low drying rates, the presence of high density areas with 610 ±32 µm thickness near the centre, characterise the back diffusion mechanism of ions.

6.6 Conclusion

XRCT is a promising technique in understanding the metal deposition inside the catalyst supports. The effect of concentration of the bulk solution, impregnation time and drying conditions on the metal profile was investigated.

The uptake of copper nitrate trihydrate solution occurs at the early stage of impregnation. The metal loading depends on the viscosity of the bulk solution, as the solution saturated at 90% required more time to migrate into smaller pores. As the metal loading is related to the porosity of catalyst support, opened pores are involved in the process of impregnation.

Both parameters, concentration of the bulk solution and impregnation time, have a significant impact on the metal distribution profile. At the beginning of impregnation, egg-shell profile is visualised and the thickness is related to the concentration of the impregnation solution. Mass transfer appears to be correlated to the concentration of the solution. The transport mechanism is revealed when comparing the cross-sectional images of the 5% and 90% saturated solutions impregnated after the drying process. Lee and Aris (1985) observed that the capillary flow changes with the viscosity of the solution. It is suggested that the high concentration of the solution increases the capillary flow inside the support. Thus, results suggest a capillary flow type mechanism. However, uniform profile is obtained after a certain impregnation time and

the distribution of the active components depends on the between diffusion and adsorption relation. Fast adsorption and slow diffusion occurred at low saturated solution (5%), whereas slow adsorption and fast diffusion occurred in the highly saturated solution (90%).

Drying has a strong impact on the metal profile. A redistribution of copper can be seen after comparing images before and after that thermal process. However, in the case of strong adsorption of the copper on the alumina support, the redistribution did not occur. A significant change of distribution is observed when the adsorption of the copper was weak. The convective flow tends to move particles towards the surface, whereas the back-diffusion transports molecules towards the centre of the support. The latter leads either to a uniform or egg-yolk distribution.

Consequently, impregnation time and drying process are significantly affecting the metal profile.

CHAPTER 7– INVESTIGATION OF THE MICROSTRUCTURE OF CATALYST SUPPORT USING THE SYNCHROTRON

7.1 Introduction

The performance of a catalyst is characterised in terms of physical parameters such as porosity, pore size distribution, specific surface area, and pore network and connectivity (Rigby and Daut, 2002).

Multiple methods have been used for the characterisation of the pore structure (Tariq et al., 2011). Typically, nitrogen adsorption and mercury porosimetry have been used to study porosity with a resolution ranging from 500 μm to 2 nm (Rigby et al., 2003a; Rigby et al. 2008; Rigby et al., 2011). Mercury porosimetry is based on the intrusion of a fluid that is non-wetting for the majority of materials through application of an externally imposed pressure. Pressure is required to force the fluid into the pores of the material. It has been shown that this technique could also be complemented with the X-Ray micro-Computed Tomography (XRCT) (Rigby et al., 2011; Peng et al., 2012). In Chapters 4 it is shown that the XRCT allows information on the density distribution of the sample (Busignies et al., 2006), the characterisation of the void size distributions and pore distribution in 3-D space (Novak et al., 2009; Tariq et al., 2011), and the characterisation of cracks. The resolution of the technique is

0.8 µm and the time required for each measurement is in the order of 45 min, imposing a significant limitation. Dynamic conditions having a characteristic time less than 45 min could not be investigated using this method. Consequently, the drying and metal impregnation of catalysts, which occur within a time scale of 45 min cannot be investigated using XRCT.

The synchrotron facilities provide a better understanding on the above phenomena (Baruchel et al., 2006). The higher resolution of the synchrotron tomography method, which is in the order of nanoscale, is a major advantage in visualising and following the development of cracks (Toda et al., 2004; Buffiere et al., 2006; Zhang et al., 2009) and/or the diffusion of metallic solution. A number of researchers have investigated crack initiation and growth in different areas, such as cast alloys (Ludwig et al., 2003; Marrow et al., 2004; King et al., 2011), polycrystalline microstructures (Herbig et al., 2001), metals (Buffiere et al., 2006), bone structures (Larrue et al., 2007), and pharmaceuticals (Morita and Yamahara, 2006; Laity and Cameron, 2010). The dynamic of the structure drying front in a porous media was also studied (Shokri et al., 2012). In terms of diffusivity of a solution inside a material, Markötter et al. conducted a study on water transport phenomena in the gas diffusion layer by using X-ray synchrotron radiography and tomography.

The experiments were performed in the I13 synchrotron beamline in Diamond Light Source, which is UK's national synchrotron facility, located at the Harwell Science and Innovation Campus in Oxfordshire. I13 is newly established and was not fully commissioned at the time the experiments were carried out. The principle objective of I13 beamline is to visualise internal features of materials at the micrometre scale by using the tomography technique and to follow the change of behaviour of the material under different processing conditions using the radiography technique. Therefore, the advantages of the I13 beamline used in the current experimental work are:

- The capability to visualise the internal structure using the tomography technique and,
- To follow the structural changes under different environmental conditions ,using the radiography technique.

The primary objective of the experiments conducted in Chapter 7 is to explore the effectiveness of the I13 synchrotron beamline in characterising the dynamic behaviour of the catalyst support, during the drying process and the impregnation of a metallic solution. Radiography and tomography were used for the investigation of those two study cases.

7.2 Effect of the hot air drying on the properties of the paste

It is worth noting that in the experiments undertaken using the radiographic technique, the initial time (t = 0 min) corresponds to the time at which the first image was taken, and does not refer to the beginning of the experiment. A time delay, typically of 2 – 3 minutes, is present due to the requirement to secure the area in the vicinity of the high-radiation beam for safety reasons. This was necessary to prevent the exposure of high-radiation to personnel and as such is present in all experiments.

7.2.1 Drying dynamic of the wet extrudate

Figure 7.1 shows four radiographic images of an extrudate having 0.92 kg water.kg solid^{-1} and extruded at 50 mm.min^{-1}. The images correspond to different drying times: 0, 5, 10 and 20 min.

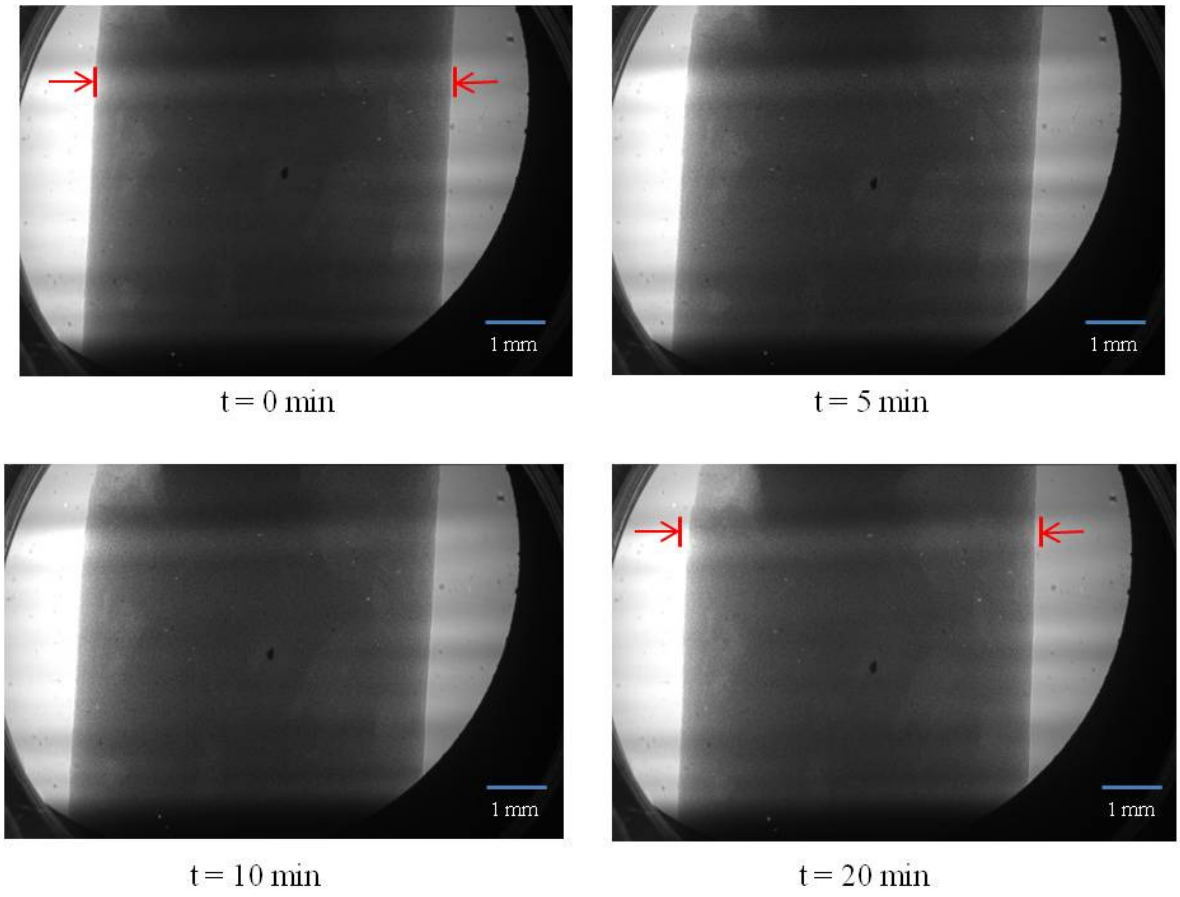

Figure 7.1: Radiography of the extrudates (water content= 0.92 kg water.kg solid^{-1}; ram speed extrusion= 50 mm.min^{-1}) while the drying process occurs. Images taken at different drying time: t = 0, 5, 10 and 20 min. (D = diameter of the extrudate at the beginning of the acquisition time).

It can be seen that the diameter of the extrudate support decreases, as indicated by the 2 red arrows. Parallel to the shrinkage of the paste, a modification of its structure occurred during the drying process. The fact that the catalyst structure tends to become brighter by increasing the drying time, indicates the change of the density inside the sample. Indeed, X-Ray attenuation is linked with density differences within the specimen material (Mousavi et al., 2005). Density is itself linked with the grey value which is between 0 and 255, in 8-bit

greyscale images (Sinka et al., 2004). The relationship between the attenuation coefficient, density and GV are given by equations presented in the Chapter 2.4.2. The change of the internal structure is induced by the water evaporation during drying process. The removal of water lead to a creation of porous network and therefore a change in density.

During the drying stage, both the diameter and the height are changing, as shown in Figure 7.2.

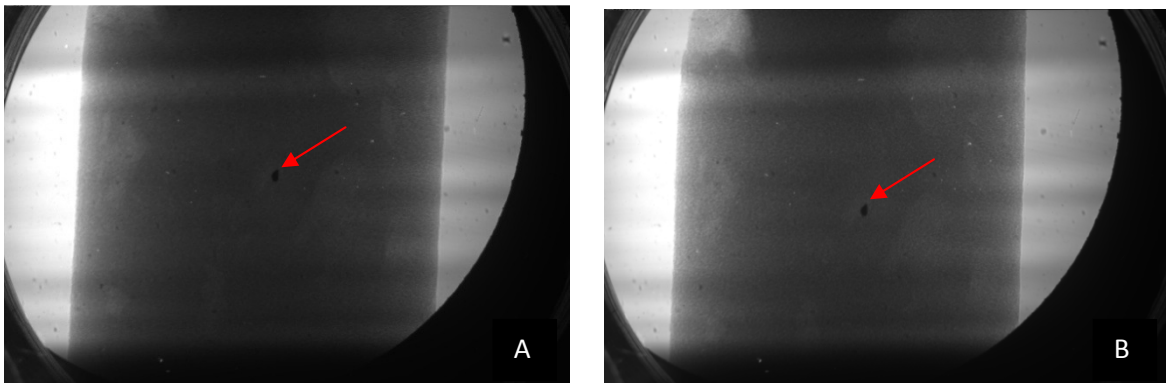

t = 0 min t = 20 min

Figure 7.2: Visualisation of shrinkage of the extrudate (water content= 0.92kg water.kg solid^{-1}; ram speed extrusion= 50 mm.min^{-1}). A) At the beginning of the acquisition time (t = 0 min) and B) at the end of the acquisition time (t = 20 min).

The volume decreases by 13% after drying the sample for 20 min. As a result of undesired contamination during the mixing of the powder samples, a high density particle can be seen in the sample. Although the introduction of this particle was unintentional, this particle can be used as a marker to follow the reduction in the height of the sample. After drying for 20 min, the particle moves by 70 µm.

7.2.1.1 Shrinkage during drying

Figure 7.3 shows the change in diameter as a function of the acquisition time for two different ram speeds (10 and 50 mm.min^{-1}), using the extrudate with an initial water content of 1.04 kg water.kg solid^{-1}.

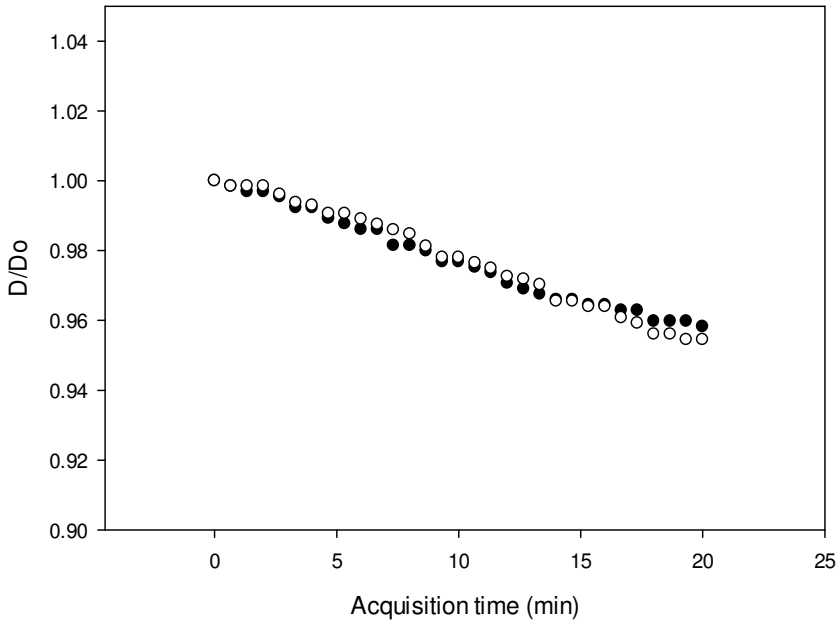

(A)

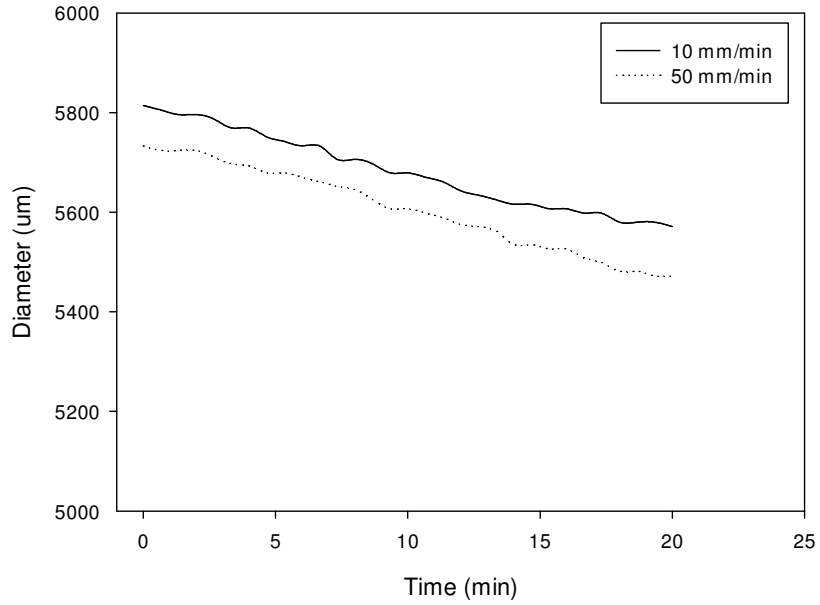

(B)

Figure 7.3: Change in diameter in (A) Drying kinetics of those 2 samples having 1.04 kg water.kg solid^{-1} and extruded at different ram speeds (white spot= 10mm.min^{-1}; black spot= 50 mm.min^{-1}); (B) Change of the diameter of those 2 samples at 2 different ram speeds through the acquisition time.

In Figure 7.3, D_o is defined as being the initial diameter at time = 0 min (i.e. D_o= 5810 µm at 10 mm.min^{-1} ram speed) and D is the diameter at a given time. D/D_o is the diameter change when the sample is under the drying condition. Figure 7.3 A) shows that the change of the ram speeds has no effect on the drying process as the drying rate follows the same trend.

The diameter of the extrudate is reduced by 4.5% and the decrease of the volume is estimated to be 3.8% during the experiment. Initially, the samples have the same size as a 5 mm diameter die was used. However, the size of the sample at t = 0 min appears to be higher than 5 mm diameter. The higher initial diameter is a result of a relaxation of the sample during the storage. The increase of the diameter is explained by two effects: (i) the relaxation of the

cylindrical paste straight after the exit from the die (Burggraaf and Cot, 1996); (ii) the expansion of the paste at the beginning of the drying stage. At t = 0 min, the expansion of the paste for the two ram speeds is about 14%. The shrinkage of the paste prior to the experiment or at the early stage of the drying process was not characterised in the preliminary experiments. The effect of the expansion cannot be characterised as the recording of the pictures started 3-4 min after the beginning of the drying process. Moreover, in terms of diameter, a discrepancy between the 10 and 50 $mm.min^{-1}$ ram speed appears. At t= 0 min, the diameter of the paste extruded at 10 $mm.min^{-1}$ is higher than the paste extruded at 50 $mm.min^{-1}$. This discrepancy is explained by the effect of the ram speed on the liquid phase migration when the pressure is applied (Liu et al., 2012).

7.2.1.2 Characterisation of the modification of the structure

During the experiments, four samples having two different water contents (0.92 and 1.04 kg water.kg $solid^{-1}$) and two ram speeds (10 and 50 $mm.min^{-1}$) were scanned. Each pixel of the projected images contains a grey value, and that value is linked to the attenuation coefficient and in turn the density of the internal structure (Mousavi et al., 2005). Therefore, the distribution of grey values is related to the microstructure. Projected images from radiography experiments were taken and the grey value distribution is shown in Figure 7.4. The distributions correspond to two different acquisition times (t = 0 min and t = 20 min).

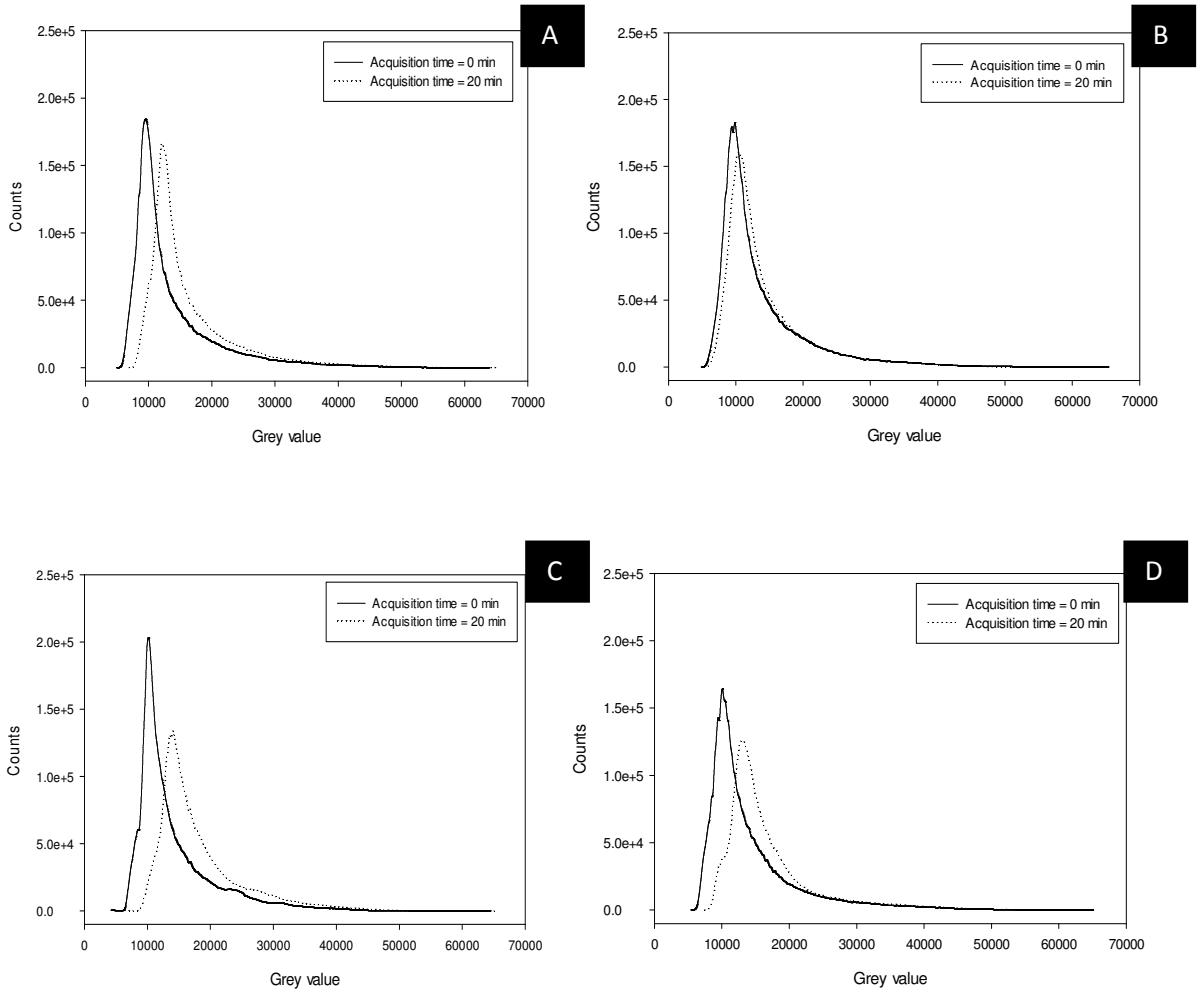

Figure 7.4: Distribution of grey values for images obtained at the beginning and at the end of the acquisition. A) 0.92 kg water.kg solid^{-1} and 10 mm.min^{-1} ram speed; B) 0.92 kg water.kg solid^{-1} and 50 mm.min^{-1} ram speed; C) 1.04 kg water.kg solid^{-1} and 10 mm.min^{-1} ram speed; D) 1.04 kg water.kg solid^{-1} and 50 mm.min^{-1} ram speed.

The four graphs shown in Figure 7.4 follow the same trend. Distribution of intensity for the images obtained at 20 min shifts towards higher grey values, implying that the brightness of the image is greater. The "darkness" of the sample, i.e. lower intensity values, is related to the attenuation of the beam due to the presence of water (Van der Merwe et al., 2007). During drying, evaporation of the water results in a porous structure and a creation of a pore network. Pores have a diameter from micrometre to nanometre scale (Sing et al., 1985; Leofanti et al.

1997), and pores below the resolution of the I13 beamline (= 2.2 µm) could not be visualised. The extrudates, with an initial water content of 1.04 kg water.kg solid^{-}1, seems to be slightly brighter than the one made with 0.92 kg water.kg solid^{-1}, showing a positive effect of water content level on the creation of pore network, and thus on porosity.

7.2.2 Cracks onset and propagation

Crack initiation and propagation can take place during drying (Potter et al., 2003). The drying process changes the structure of the material by creating a porous network for instance. The shrinkage of the paste and the creation of high porosity can reduce the strength of the material (Bataille et al, 1993). Therefore, defects could be initiated during the thermal treatment. Indeed, pores act as stress concentrators and cracks are often initiated there (Par Jonsen, 2006). In the radiographic experiments, the onset and the development of defects was not observed due to the thickness of the sample. In addition, no external cracks were revealed.

In order to evaluate the presence of internal cracks, a tomography scan is carried out using the same sample. In Figure 7.5, the two dimensional reconstructed cross section obtained after drying the sample show the inner structure and the pore distribution.

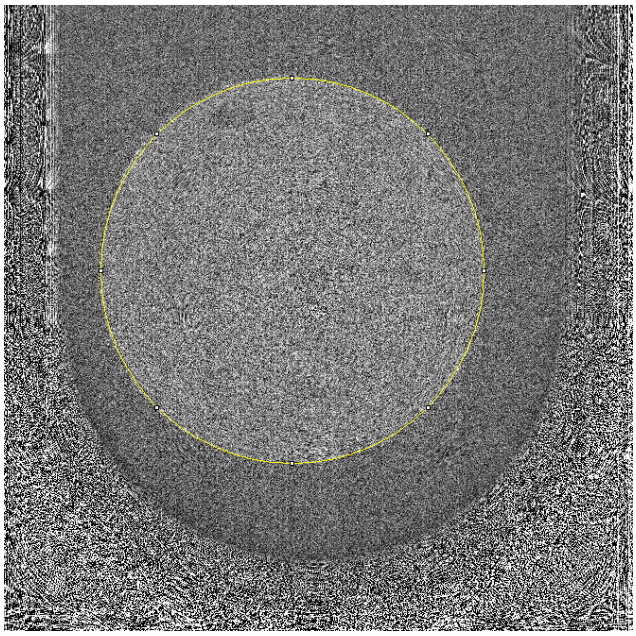

(A)

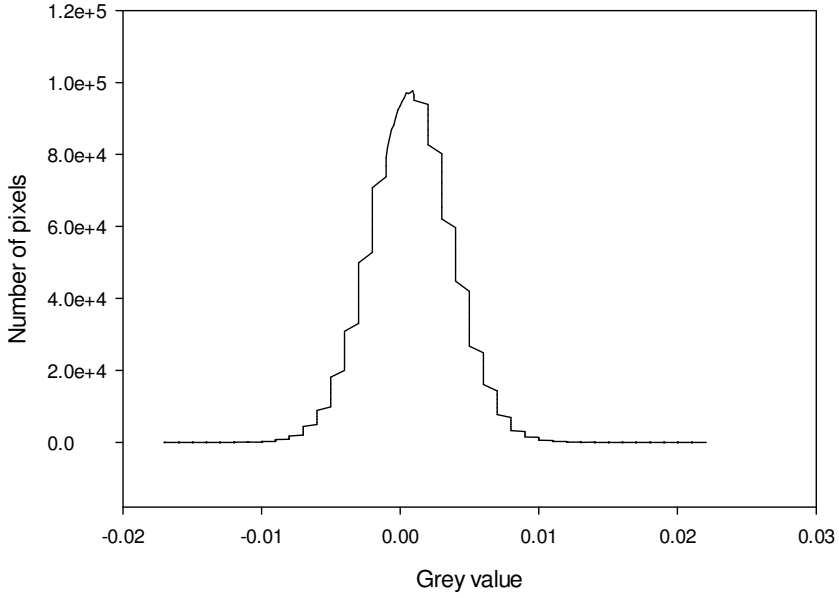

(B)

Figure 7.5: A) Two dimensional reconstructed cross sectional image after finding the centre of rotation; B) Its distribution of grey value.

To characterise cracks, a segmentation of the image is necessary to distinguish objects (pores and cracks) from the material. The principle is explained in Chapter 4.6.2.2. The selection of cracks among pores was carried out by the determination of the aspect ratio value closer to 0 or the Structure Model Index (SMI) which is inferior or equal to 1 (Olaf Dossel and Wolfgang Schlegel (2009)). Unfortunately, the distinction between pore network and structure is not possible after processing the reconstructed images. The different trials of threshold range were applied but failed due to the substantial noise and blurring incorporated in the image. Reconstructed images are of low quality as the reconstruction program is still under development. Several parameters of the reconstruction script, such as the reduction of noise, increase of the contrast or even the change of the rotation step (see Chapter 3.3.2), were modified. None of the parameter modified within the script enhanced the image quality.

7.3 Extrudate impregnation

Alumina catalyst support is impregnated using copper nitrate trihydrate solution, saturated at 90%. The aim of this work is to visualise the distribution of the copper within the extrudate during the wet impregnation. Extrudates are dipped into a copper nitrate trihydrate ($Cu(NO_3)_2$) solution saturated at 90%, as shown in Figure 7.6.

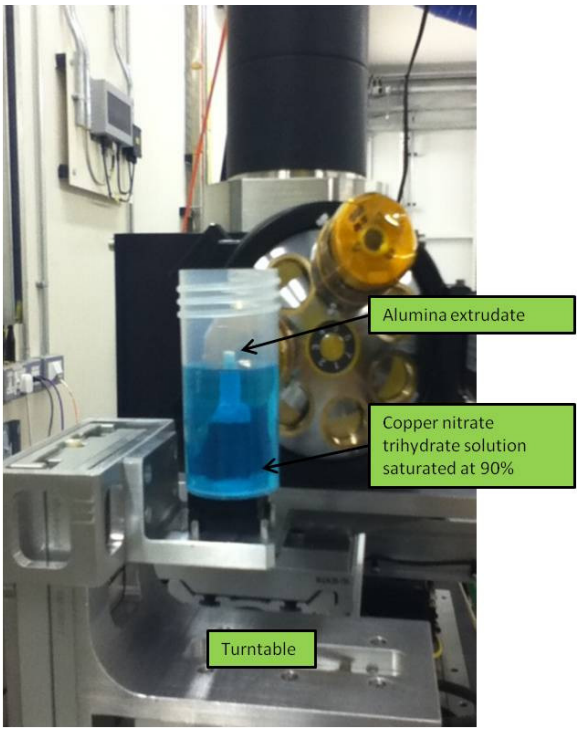

Figure 7.6: Photograph of the installation for radiography experiments.

Dynamic behaviour of the catalyst support immersed in a metallic impregnation was recorded for 20 min by radiography, following by the visualisation of the metal profile with tomography scan.

7.3.1 Calibration of the monochromator

In order to observe its distribution in the alumina support, a calibration of the monochromator around the K-edge (K-edge $_{copper}$ = 8.979 keV) is required. The monochromator is a device transmitting a narrow band of wavelength of radiation among a wider range of them input at the beginning. A single wavelength is selected from the beam using a crystal.

A preliminary experiment is performed using a copper foil placed in between the X-ray tube and the detector. To determine the Bragg angle values, consecutive experiments were carried out. The absorption of the foil is observed and recorded by changing the Bragg angle. Figure 7.7 shows two radiographic pictures taken from two different Bragg angles, in which the density distribution of the copper foil is visualised. At some point, the change of the absorption, which corresponds to the energy range below and above the copper K binding energy, is observed.

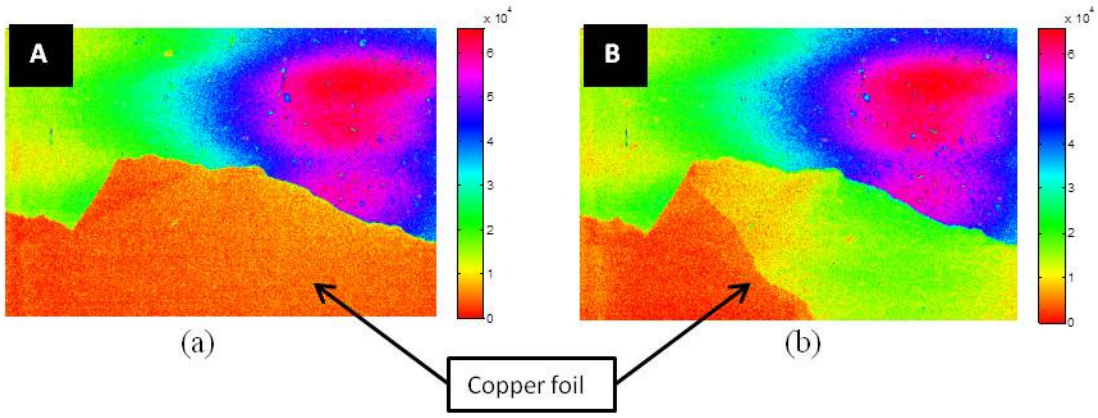

Figure 7.7: Radiography images of the copper foil obtained by changing the Bragg angle while calibrating the monochromator; A) Bragg angle = -19.655^{o}; B) Bragg angle = -19.645^{o}.

7.3.2 Distribution of the copper nitrate trihydrate

After finding the 2 values of the Bragg angles in which the copper could be localised in the sample, two tomography scans were carried out. Figure 7.8 shows 2-D reconstructed cross sectional images of the alumina support impregnated in the copper nitrate trihydrate solution saturated at 90% for 5 min and dried at 100^{o}C in the oven. The cross sections are 32-bit images, meaning that the greyscale value is from -1 to 1.

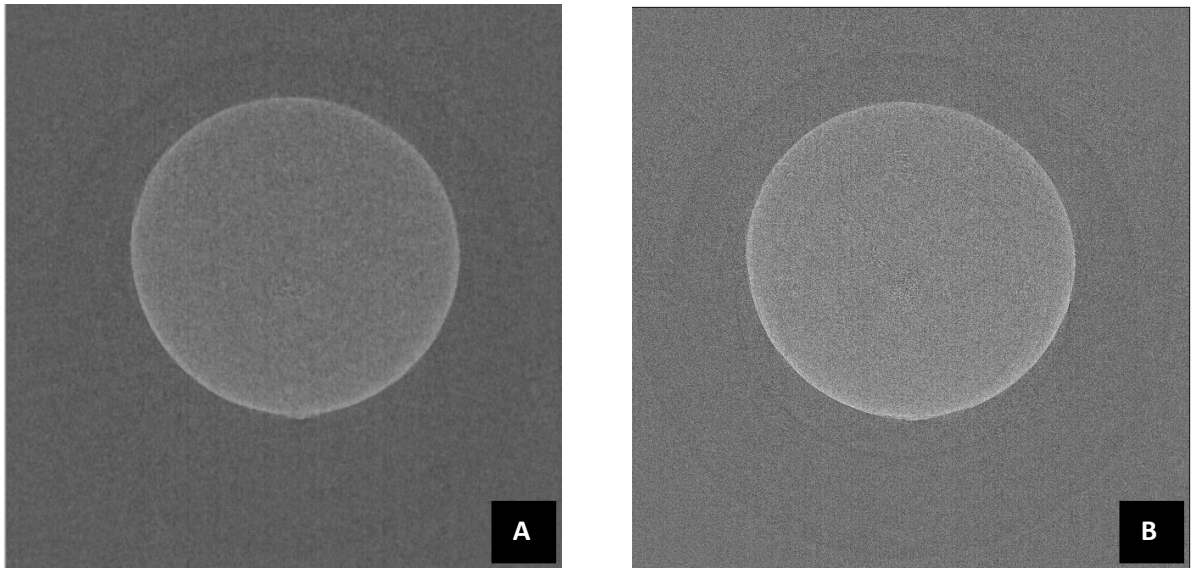

Figure 7.8: 2-D reconstructed cross sectional images of two different scans: A) below the copper K binding energy; B) above the copper K binding energy.

In principle, comparison of the two images should identify the location of the copper in the sample. Copper should be brighter, as it is adsorbed by the X-Ray. Reconstruction leads to a noisy 2-D image with artefacts that assist in locating the copper distribution. By comparing those two cross-sectional images from the middle of the sample, a density variation, determined by the mean grey value and the standard deviation, is observed, as shown in Table 7.1. Three areas were defined for each reconstructed image: the centre of the extrudate, the surface of the extrudate corresponding to a thickness of 50 µm, and the background of the images.

Table 7.1: Grey value mean and the standard deviation taken from 3 different areas of each cross sectional image, shown in figure 7.8.

	Centre of the extrudate	Surface of the extrudate	Background
Below the copper K binding energy	0.002 +/- 0.002	0.005 +/- 0.003	-0.00020 +/- 0.00200
Above the copper K binding energy	0.002 +/- 0.002	0.004 +/- 0.003	-0.00019 +/- 0.00200

The fact that the value of the standard deviation is 10 times higher than the mean grey value, suggests the heterogeneity of the background is a result of the noise. In theory, the background of the image should be black, with a very small standard deviation. The surface of the catalyst shows a high absorption of the monochromatic beam on the surface of the catalyst. The density from the centre to the surface is increased by 250 %. By comparing the mean grey value obtained from below and above the copper K binding energy on the surface, a small difference is observed suggesting the presence of the copper. The standard deviation is important, and its value is similar over the image. The presence of artefacts causes problems in the data analysis of density variation through in the sample and on the distinction between structure and pores as the mean grey value of the inner core is equal to the standard deviation. Consequently, it is difficult to see how the copper is distributed within the sample, although that the high density layer over the entire surface of the sample suggest the presence of that compound. The inability of the non-visualisation of the metallic compound on the tomographic scan using the synchrotron could be raised as a question. To answer to that interrogation, a comparison with another imaging technique is required.

7.3.3 Comparison with the X-Ray micro-Computed Tomography

The sample that was used to undertake radiographs, was scanned using another imaging technique, the X-Ray micro-Computed Tomography (Skyscan 1172). Figure 7.9 shows the tomographic cross section of the alumina support impregnated in the copper nitrate trihydrate solution saturated at 90 % for 5 min and dried at 100^{o}C in the oven.

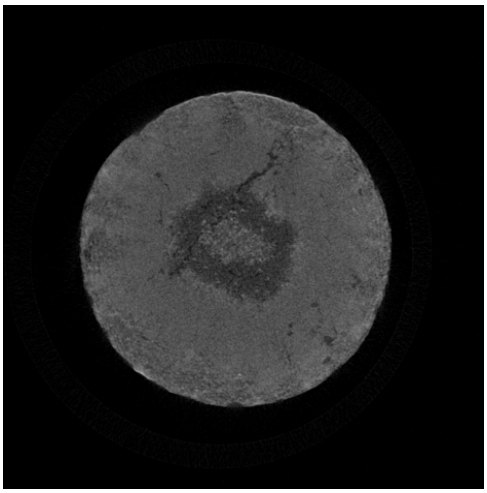

Figure 7.9: Visualisation of metal profile of alumina support impregnated in the copper trihydrate solution saturated at 90% and dried at 100^{o}C from the tomographic image by using the X-Ray micro-Computed Tomography (Skyscan 1172).

The tomographic picture obtained from the XRCT reveals information that was not obtained from the synchrotron in Figure 7.8. Metal distribution is visualised by the presence of egg-shell and egg yolk profile. The thickness of the metal is 1377±52 µm. A density distribution is observed with high and low intensity areas. Intensity follows the Beer-Lambert law of absorption (de Paiva *et al.,* 1998; Phillips and Lannutti, 1997). The equation is shown in

Chapter 2.4.2.1. That law depends on the beam intensity, on the intensity of the beam after traversing a layer of material of thickness 'x' and on the attenuation coefficient (μ(x)). The linear attenuation coefficient, μ, is dependent on atomic number and mass density (Van Geet et al., 2000; Salvo et al., 2003). The atomic number of copper and alumina are respectively Z_{copper}= 29 and $Z_{alumina}$= 13. Absorption of the copper should be higher when compared to absorption of alumina. Therefore, the observation of the reconstructed image reveals the presence of copper in the outer core and in the centre area, as those parts are denser. The distribution of the copper inside the support after drying at 100°C in the oven shows an egg shell and egg yolk formation.

7.3.4 Dynamics of impregnation

The second part of the work aimed at following the impregnation of the metallic solution into the sample by using the radiography method. In this experiment, the alumina support was partially installed in a plastic beaker half-filled with the copper nitrate trihydrate solution saturated at 90%, as shown in Figure 7.10 A). The diffusivity of the solution into the catalyst will be followed from the area in which the sample is not dipped into the metallic solution. The recording of the impregnation lasted 20 min and pictures were captured every 20 seconds. Figure 7.10 B) shows the radiographic image taken at t = 0 min.

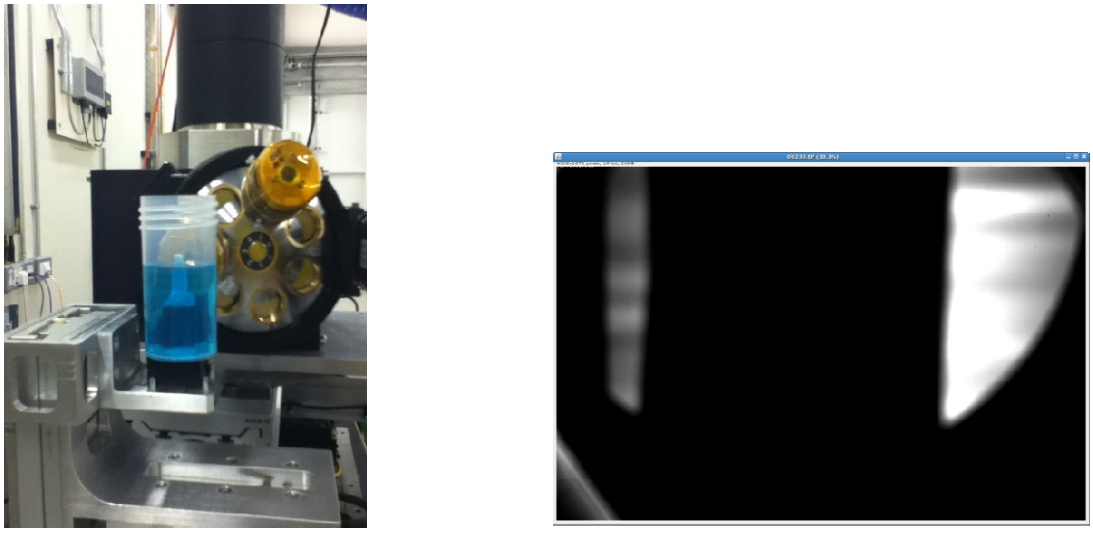

Figure 7.10: a) Photograph of the installation for the radiography; b) Picture of the sample captured during the radiography experiments at t= 0 min.

In Figure 7.10 B), the image is blurred, which could be explained by the X-ray absorption of the plastic beaker. In addition, the extrudate is very dark, not allowing the visualisation of the migration of the copper nitrate trihydrate solution. The darkness of the images remains similar throughout the experiments, which was not allowing the visualisation of the sample. Therefore, the diffusivity of the metallic solution could not be traced and analysed. It would have been interesting to see if the mass transfer of the solution into the sample could not be seen because of the high absorption of the plastic beaker.

7.4 Conclusion

Experiments on the visualisation of the crack propagation and the diffusivity of the metallic solution in the sample during the impregnation were carried out using the new I13 beamline.

In those two study cases, radiography and tomography scans were undertaken and results were analysed.

Information about the kinetics of shrinkage could be seen using the radiography. The size of the sample decreased by 4.5% due to the removal of the water from the catalyst support, which also induced a change of the structure, i.e. a pore network. It was not possible to identify the development of cracks during drying. The characterisation of internal cracks with the tomography technique was not possible due to the experimental noise and the ring artefact on the image.

Regarding to the diffusivity of the copper nitrate trihydrate inside the sample, it could not be followed by radiography as a result of the opacity of the image and the absorption of the plastic beaker. It was also impossible to visualise the egg shell and egg yolk distribution of the copper in the extrudate in the tomography experiments, even though a calibration of the monochromator was done.

The new I13 synchrotron beam provides advantages, such as the ability to follow the dynamic behaviour of the paste under drying conditions, to use a monochromatic beam and to visualise the internal structure at microscale. Significant challenges were encountered when performing the tomography experiments. The key part of the process that can be improved is the reconstruction step using the script written, developed and adapted to the beamline and developed in Diamond. In order to acquire high-quality images, further trials on the modification of input parameters in the script are required.

CHAPTER 8 – CONCLUSION

8.1 Introduction

A catalyst support is selected according to certain characteristics, such as desirable mechanical properties (attrition resistance and strength), stability, high surface area and porosity (Satterfield, 1970). These characteristics depend on the preparation of catalyst support, which is divided into several steps from the formulation to the finishing. Control of physical and chemical parameters is necessary, since the internal structure of catalyst support changes after each stage of the processing route. Catalyst preparation has a strong impact on density distribution and porosity. Knowledge of the internal porous structure is essential in improving the development of a catalyst, leading to an enhanced performance. XRCT is a non-invasive and non-destructive technique that can be used to obtain 3-D images of scanned samples and to visualise the internal structure of materials (Phillips and Lannutti, 1997; Burch, 2002).

The three principal objectives defined at the beginning of the project, and specified in Chapter 1, were achieved. The development of the capability of the XRCT to characterise catalyst structure was undertaken. Formed particles and the comparison of density/porosity

distributions in order to help develop forming technologies that produce the desired structures were characterised. Metal distribution in impregnated catalysts, that is very important in order to improve support selection and understanding of deposition techniques, was investigated. Finally, X-Ray micro-Computed Tomography and Synchrotron X-Ray Tomography have been compared.

8.2 Density studies using XRCT

This research shows the capability of the XRCT imaging technique to correlate density distribution with processing route and formulation of different catalyst supports. The technique was applied successfully and, the visualisation of internal structure of several catalyst supports, the effect of processing parameters and formulation were studied.

The internal structure between different catalyst supports was investigated and information was revealed on the density variation, such as the presence of low density areas in the catalyst, a high density area in the outer core, cracks and pores. Pores could not be visualised, as the pores size is below the resolution of XRCT. However, the density variation provides information on the porosity of the sample.

In tablets, an important heterogeneity with a high density area in the periphery and low density in the inner core is shown in the cross sectional images (X-Y) and their respective density maps. That heterogeneity is the result of the compaction process due to the effect of punches and the die wall. In addition, the amount of graphite added appears to have an impact on the density, as the density of the sample with 10 % graphite was less intense than the one with 2 % graphite. A higher amount of graphite added in the support decreased the density

and therefore, increased the porosity of the catalyst support. The calcination process has a significant effect on density, as the sample is slightly denser under higher temperature condition. Calcination tends to develop narrow pores and therefore, to change the structure of the support by decreasing the size of the sample.

In granules, lower and higher density areas are revealed by the presence of 2 obvious peaks in a bimodal distribution. The effect of formulation, such as the main component and the binders, were studied. The change of components and binders has an important impact on density distribution and strength of the final product.

The extrusion process appeared to affect the density distribution. Among the alumina extrudates, 40 % of them showed a failure (cracks) in their structure, which were formed internally and externally.

8.3 Effect of the extrusion process on the cracks development

The purpose of this investigation was to develop a methodology on how to detect and characterise cracks within the catalyst using the XRCT, and then to apply the method in investigating the effect of the water content, the ram extrusion speed, the drying temperature as well as the calcination process on the crack initiation and propagation.

The XRCT allows the localisation of cracks to be visualised within the sample, and shows its direction and shape. The cracks' propagation tends to follow the direction of the extrusion process. According to the initial moisture content level, speed of the ram extrusion, and drying rate, the internal structure and the mechanical properties are different. Indeed, the voids' thickness increases with increasing the water content, the ram speed extrusion and the

drying rate. Pores and cracks were distinguished by the Structure Model Index value. The interaction between water content and drying process influences the development of cracks in terms of the total volume, the surface area and the numbers of cracks. The calcination has a positive effect on the number of cracks and their development inside the sample.

8.4 Metal distribution in the support by wet impregnation

The distribution of the copper nitrate trihydrate solution in alumina extrudate was characterised by the XRCT technique. The effects of concentration of bulk solution, impregnation time and drying condition on the metal profile were investigated.

Both parameters, concentration of the bulk solution and impregnation time, have a significant impact on the metal distribution profile. At the beginning of impregnation, mass transfer is correlated to the concentration of the solution and a uniform profile is obtained after a certain impregnation time. It also seems that the high concentration of bulk solution increases the capillary flow inside the support. In addition, the distribution of the active components depend on the diffusion and adsorption correlation. Fast adsorption and slow diffusion occurred at low saturated solution (5%), whereas slow adsorption and fast diffusion is observed at high saturated solution (90%).

Drying has a strong impact on the metal profile, as a redistribution of copper was noticed by comparing images before and after the thermal process. However, the redistribution did not take place in the case of strong adsorption of copper on the alumina support. Under condition of weak adsorption, a significant change in distribution is observed. The convective flow

tends to move particles towards the surface, whereas the back-diffusion transports molecules towards the centre of the support. The latter leads either to a uniform or egg-yolk distribution.

Consequently, impregnation time and drying process are the two major parameters affecting the metal profile. Impregnation time is a critical factor, as diffusion and adsorption of metal in the support are occurring.

8.5 Synchrotron

Experiments on the visualisation of the propagation of the cracks and the diffusion of the metallic solution in the sample during the impregnation, were carried out using the new I13 beamline. For those two study cases, radiography and tomography scans were undertaken and the results were analysed.

With regard to the behaviour of the extruded paste, the results of the radiographic scans show a 3-D shrinkage of the paste while the drying process occurs. The removal of the water from the catalyst support induces a change of the structure, creating a pore network. However, it was not possible to see the development of cracks during the drying process, meaning that surface cracking is not visible. The characterisation of internal cracks with the tomography technique was not achievable because of noise and ring artefact on the image. The same problem occurred for the visualisation of the copper nitrate trihydrate solution inside the sample.

The new I13 synchrotron beam provides advantages, such as the ability to follow the dynamic behaviour of the paste under drying conditions, the use of a monochromatic beam and the visualisation of the internal structure at microscale. Significant challenges were encountered

when performing the tomography experiments. The key component is the reconstruction step using the script written, developed and adapted to the beamline and developed in Diamond. In order to acquire high-quality images, further trials on the modification of input parameters in the script are required.

8.6 Conclusion

The XRCT technique is fast and can be used to perform routine check-up. Effects of the formulation and the processing route on the internal structure of catalysts were studied. The technique allows the visualisation of density, as well as pore distribution and the presence of defects at different stages of the processing route. However, the XRCT technique shows limitations. A comparison of densities between samples could be undertaken only if the samples are scanned under the same condition. Although the input parameters are fixed, the power of X-ray beam could be slightly different, which introduces differences in terms of the material's absorption. Characterisation of pores and cracks is dependent on the image segmentation, blurredness and noise.

The X-Ray computed tomography is a technique which only provides a "snapshot" of the internal structure of the material for a given time. the I13 beamline synchrotron tomography in DIAMOND provides a better understanding in following the drying phenomena and/or the diffusion of metallic solution in the catalyst during impregnation, which are not achievable with any other conventional methods. The porous structure of the catalysts and the development of cracks in them would happen at nano-scale as well as at the micro-scale. I13 beamline is newly established and was not fully commissioned at the time the experiments were carried out. The main issue of the work was about the tomography experiments. The key

part is the reconstruction step using the script written, developed and adapted to the beamline in Diamond. In order to have high quality images, more trials on the modification of input parameters in the script are required. It would have been interesting to repeat the reconstruction part with the projected images.

After comparing the results obtained from the XRCT with the ones from the synchrotron tomography, the possibility of following different phenomena in real time using radiography experiments and the characterisation of internal structure using the tomographic technique could provide advantages. Johnson Matthey is mostly interested in using the synchrotron technique for future research.

REFERENCES

Acres, G.J.K. (1980). The characterisation of catalysts, a survey of present industrial practice. *Platinum Metal Review*, 24, (1), 14-25.

Ahange, G., Schwartz, G.B., Schanaare, R.L. (1990). Effects of spheronization technique on drug release from uncoated beads. *Drug Dev. Ind. Pharm*., 16, 1171–1184

Allen, T. (1997). *Particle size measurement*, 5th Ed., Chapman & Hall, New York, USA, p. 251.

Allisy-Robert, P., Williams, J. (2008). *Farr's physics for medical imaging*. 2nd edition. Saunders Elsevier.

Antoine, C., Nygård, P., Gregersen, O.W., Holmstad, R., Weitkamp, T., Rau, C. (2002). 3D images of paper obtained by phase-contrast X-ray micro-tomography: image quality and binarisation. *Nuclear Instruments and Methods in Physics Research,* A 490, 392-402

Ammouche, A., Riss, J., Breysse, D., Marchand, J. (2001). Image analysis for the automated study of microcracks in concrete. *Cement and concrete composites*, 23, 267-278.

Appoloni, C.R., Fernandes, C.P., Rodrigues, C.R.O. (2007). X-ray tomography study of a sandstone reservoir rock. *Nucl Inst Meth*, 32, 580-629.

Atwood, R.C., Jones, J.R., Lee, P.D., Hench, L.L., (2004). Analysis of pore interconnectivity in bioactive glass foams using X-ray microtomography. *Scripta Materialia*, 51, 1029-1033.

Auvinet, G., Bouvard, D. (1989). Pore size distribution of granular media. *Powders and grains*. Biarez & Gourves (Eds.), Balkema, Rotterdam, 35 – 40.

Bashaiwoldu, A.B., Podczeck, F., Newton, J.M. (2004). A study on the effect of drying techniques on the mechanical properties of pellets and compacted pellets. *European Journal of Pharmaceutical Science*, 21, 119–129.

Barrett, E.P., Joyner, L.G. and Halenda, P.P. (1951). The determination of pore volume and area distributions in porous substances. *I. Computations from nitrogen isotherms*. J. Amer. Chem. Soc. 73, 373 – 380.

Baruchel, J., Buffiere, J-Y., Cloetens, P., Di Michiel, M., Ferrie, E., Ludwig, W., Maire, E., Salvo, L. (2006). Advances in synchrotron radiation microtomography. *Scripta Materialia*, Volume 55, Issue 1, 41-46.

Bataille, B., Ligarski, K., Jacob, M., Thomas, C., Duru, C. (1993). Study of the influence of spheronisation and drying conditions on the physico-chemical properties of neutral spheroids containing Avicel PH 101 and lactose. *Drug Dev. Ind. Pharm*., 19, 653–671.

Beucher, S., Lantuejoul, C. (1979). *Use of watersheds in contour detection*. In: Proceedings of the internal workshop on image processing. CETT/IRISA.

Bird, M.I., Ascough, P.L., Young, I.M., Wood, C.V., Scott, A.C. (2008). X-ray microtomographic imaging of charcoal. *Journal of Archaeological Science,* 35, 2698-2706.

Boas, F.E., Fleischmann, D. (2012). Evaluation of two iterative techniques for reducing metal artifacts in computed tomography. *Radiology*, 259(3), 894-902.

Bond, G.C., Tahi,r S.F. (1991). *Application in Catalysts*. 71.

Boshoff-Mostert, L., Viljoen, H.J., (1996). Crack propagation in catalytic pellets due to thermal stresses. *AICheE Journal*, 42, n^{o}8, 2288-2294.

Bowler, J.R., (2002). Thin-skin eddy-current inversion for the determination of crack shapes. *Institute of physics publishing inverse problem,* 18, 1891-1905.

Buffière, J.-Y., Ferrie, E., Proudhon, H., Ludwig, W. (2006). Three dimensional visualisation of fatigue cracks in metals using high resolution synchrotron X-ray micro-tomography, *Materials Science and Technology,* 22 (9), 1019-1024.

Burch, S., (2002). Measurement of density variations in compacted parts using X-ray computerised tomography. *MPR Technical Trends*, 24-28.

Burggraaf, A.J., Cot, L. (1996). *Fundamentals of inorganic membrane science and technology*. Elsevier, 124.

Busignies, V., Leclerc, B., Porion, P., Evesque, P., Couarraze, G., Tchoreloff, P. (2006). Quantitative measurements of localized density variations in cylindrical tablets using X-ray microtomography. *European Journal of Pharmaceutics and Biopharmaceutics*, 64, Issue 1, 38-50.

Campanati, M., Fornasari, G., Vaccari, A., (2003). Fundamentals in the preparation of heterogeneous catalysts. *Catalysis today*, 77, 299-314.

Clarke and Eberhardt (2000). *Microscopy technique for materials science*. 342.

Clausnitzer, V., Hopmans, J. W. (2000). Pore-scale measurements of solute breakthrough using microfocus X-ray computed tomography. *Water resources research*, 36, 8, 2067-2079.

Cloetens, P., Pateyron-Salomi, M., Buffiere, J.Y., Peix, G., Baruchel, J., Peyrin, F., Schlenker, M. (1997). Observation of microstructure and damage in materials by phase sensitive radiography and tomography. *Journal of Applied Physics*, 81, 5878-5886.

Conesa-Boj, S., Estradé, S., Rebled, J. M., Prades, J.D., Cirera, A., Morante, J.R., Peiró, F., Arbiol, J. (2010). Advanced Electron Microscopy Techniques on Semiconductor Nanowires: from Atomic Density of States Analysis to 3D Reconstruction Models. Book: *Nanotechnology and Nanomaterials*.

Cormack, A.M. (1963), Representation of a function by its line integrals, with some radiological applications, Part I, *Journal Application of Physics*. 34, 2722–2727.

Cormack, A.M. (1964), Representation of a function by its line integrals, with some radiological applications, Part II, *Journal Application of Physics*. 35, 2908–2913.

Couroyer, C., Ning, Z., Ghadiri, M. (2000). Distinct element analysis of bulk crushing: effect of particle properties and loading rate. *Powder Technology*, 109, 241–254.

Cunningham, I. A., Judy, P. F. (2000). *Computed Tomography*. The Biomedical Engineering Handbook: Second Edition. Ed. Joseph D. Bronzino

Datye, A.K. (2003). Electron microscopy of catalysts: recent achievement and future prospects, *Journal of catalyst*, 216, 144-154.

De Man, B., Nuyts, J., Dupont, P., Marchal, G., Suetens, P. (1999). Metal streak artifacts in x-ray computed tomography: A simulation study, *IEEE Trans. Nucl. Sci.,* 46, 691–696.

De Paiva, R.F, Lynch, J., Rosenberg, E., Bisiaux, M. (1998). A beam hardening correction for X-Ray micro-Computed Tomography. *NDT&E International*, 31, 1, 17-22.

Dees, P.J. and Polderman, J. (1981). Mercury porosimetry in pharmaceutical technology. *Powder Technology*, 29, 187 - 197.

Doesburg, E.B.M., van Hooff, J.H.C (1993). An Integrated Approach to Homogeneous, Heterogeneous and Industrial Catalysis, *Studies in Surface Science and Catalysis*, vol. 79, Elsevier, Amsterdam, Chapter 8.

Donath, T. (2007). *Quantitative X-ray Microtomography with Synchrotron Radiation*. GKSS-Forschungszentrum Geesthacht GmbH. Geesthacht.

Douarche, N., Rouby, D., Peix, G., Jouin, J.M., (2001). Relations between X-ray tomography, density and mechanical properties in carbon-carbon composites. *Carbon*, 39, 1455-1465.

Doymaz, I. (2013). Effect of blanching temperature and dipping time on drying time of broccoli. *Food Science and Technology International*. 0(0). 1–9.

Ek, R., Lennholm, H., Davidson, R., Nyström, C. and Ragnarsson, G. (1995). Pore swelling in beads made of cellulose fibres and fibre fragments. *Int. Journal Pharmaceutic*. 122, 49 - 56.

Erdogan, S., Quiroga, P., Fowler, D., Saleh, H., Livingston R., Garboczi E. (2006). Three-dimensional shape analysis of coarse aggregates: New techniques for and preliminary results on several different coarse aggregates and reference rocks. *Cement and Concrete Res*, 36,1619–27.

Ertl, G., Knözinger, H., Weitkamp, J. (1997). *Handbook of Heterogeneous Catalysis*, vol. 1, Wiley/VCH, New York/Weinheim, 49.

Farber, L., Tardosb, G., Michaelsa, J.N. (2003). Use of X-ray tomography to study the porosity and morphology of granules, *Powder Technology*, 132, 57–63.

Feldkamp, L. A., Davis, L. C., Kress, J. W. (1984). Practical conebeam algorithm. *Journal Optical Society American*, 1, 612–619.

Ferrie, E., Buffiere, J-Y., Ludwig, W. (2005). 3-D characterisation of nucleation of a short fatigue crack at a pore in a cast Al alloy using high resolution synchrotron microtomography. *International Journal of Fatigue*, 27, 1215-1220.

Flannery, B.P., Deckman, H.W., Roberge W.G., D'Amico K.L. (1987), Three dimensional X-ray micro-tomography, *Science*, 237, 1439–1444.

Gai, P.L. (2001). Developments of electron microscopy methods in the study of catalysts. *Current Opinion in Solid State and Materials Science*, 5, 371–380.

Gavriilidis, A., Varma, A., Morbidelli, M. (1993). Optimal distribution of catalyst in pellets. *Catalysis Reviews-Science Engineering*, 35, 399–456.

Goodhew, P.J., Humphreys, F. J. (2001). *Electron Microscopy and Analysis*. Third edition. Taylor & Francis, 251 pages.

Goula, M.A. (1992). Development of molybdena catalysts supported on γ-alumina extrudates with four different Mo profiles: preparation, characterisation and catalytic properties. *Journal of catalysts*, 137, 285-305.

Grunwaldt, J.D., Kimmerle, B., Baiker, A., Boye, P., Schroer, C.G., Glatzel, P., Borca, C.N., Beckmann F. (2009). Catalysts at work: From integral to spatially resolved X-ray absorption spectroscopy. *Catalysis Today*. 145, 3–4, 267–278.

Heise, M.S., Schwartz, J.A. (1987). Preparation of Metal Distributions within Catalyst Supports. *Studies in Surface Science and Catalysis*, 31, 1–13.

Herbig, M., King, A., Reischig, P., Proudhon, H., Lauridsen, E.M., Marrow, J., Buffière, J.-Y., Ludwig, W. (2011). 3-D growth of a short fatigue crack within a polycrystalline microstructure studied using combined diffraction and phase-contrast X-raytomography, *Acta Materialia*, 59, 590-601.

Herremans, E., Chassagne-Berces, S., Chanvrier, H., Atomniuk, A., Kusztal, R., Bongaers, E., Verlinden, B.E., Jakubczyk, E., Estrade, P., Verboven, P., Nicolai, B., (2011). *Possibilities of X-Ray nano-CT for internal quality assessment of food products*. 11th conference on Engineering and Food: Novel technologies to explore food microstructure, 22-26th May 2011, Athens, Greece.

Hidlebrand, T., Ruegsegger, P. (1997). Quantification of bone microarchitecture with the structure model index. *Computer method biomechanical biomedical engineering*, 1, 15-23.

Johansson, B., Wikberg, M., Ek, R., Alderborn, G. (1995). Compression behaviour and compactability of microcrystalline cellulose pellets in relationship to their pore structure and mechanical properties. *Internal Journal Pharmaceutical*, 117, 57–73.

Kaneko, K. (1994), Determination of pore size and pore size distribution: absorbents and catalysts, *Journal of Membrane Science*, 96, 1-2, 59-89.

Kaestner, A, Schneebeli, M, Graf, F (2006). Visualizing three-dimensional root networks using computed tomography. *Geoderma,* 136:459–69.

Kastner, J., Bernhard, H., Requena, G., Brunke, O. (2010). A comparative study of high resolution cone beam X-ray tomography and synchrotron tomography applied to Fe- and Al-alloys. *NDT E Int.*, 43(7-3), 599–605.

King, A., Ludwig, W., Herbig, M., Buffière, J.-Y., Khan, A.A., Stevens, N., Marrow, T.J. (2011) Three-dimensional in situ observations of short fatigue crack growth in magnesium. *Acta Materialia*, 59, 17, 6761-6771.

Kleinebudde, P. (1994). Shrinking and swelling properties of pellets containing MCC and low substituted hydroxy propyl cellulose. Part II. Swelling properties *International Journal Pharmaceutical*, 109, 221–227.

Komiyama, M., Merrill, R.P., Harnsberger, H.F. (1980). Concentration profiles in impregnation of porous catalysts: Nickel on Alumina. *Journal of Catalysis*, 63, 35–52.

Kong, C.M., Lannutti, J.J. (2000). Effect of agglomerate size distribution on loose packing fraction, *Journal American Ceramique*, 83(9), 2183-2188.

Kotter, M., Riekert, L. (1983). Impregnation type catalysts with non uniform distribution of the active component. Part II: Preparation and properties of catalysts with different distribution of the active component on inert carriers. *Chemical Engineering Fundamentals*, 2, 31–38

Kowalski, S.J. (2000). Toward a thermodynamics and mechanics of drying processes. *Chemical Engineering Science*, 55, 1289–1304.

Larrue, A, Rattner, A, Laroche, N, Vico, L, Peyrin, F. (2007). Feasibility of micro-crack detection in human trabecular bone images from 3D synchrotron microtomography. *Conf Proc IEEE Eng Med Biol Soc*., 21,3918.

Le trong, E., Rozenbaum, O., Rouet, J.L, Bruand, A. (2008). A simple methodology to segment X-Ray tomographic images of multiphasic building stone. *Image Anal Stereol*, 7, 175-182.

Lee, S.Y., Aris, R. (1985). The distribution of active ingredients in supported catalysts prepared by impregnation. *Catalysis Reviews-Science and Engineering*, 27, 207.

Lekhal, A., Glasser, B., Khinast, J. (2001). Impact of drying on the catalyst profile in supported impregnation catalysts. *Chemical Engineering Science*. 56, 15, 4473–4487.

Lekhal, A., Glasser, B., Khinast, J. (2004). Influence of pH and ionic strength on the metal profile of impregnation catalysts. *Chemical Engineering Science*. 59, 5, 1063–1077.

Leofanti, G., Tozzola, G., Padovan, M., Bordiga, S., Zecchina, A., (1997). Chapter 4, Catalyst characterisation: Characterisation techniques. *Catalysis today*, 34, 307-327.

Li, W.D., Li, Y.W., Qin, Z.F., Chen, S.Y. (1994). Theoretical prediction and experimental validation of the egg-shell distribution of Ni for supported Ni/Al2O3 catalysts. *Chemical Engineering Science*, 49,. 4889–4895.

Li, Z. Y., Young, N. P., Di Vece, M., Palomba, S., Palmer, R. E., Bleloch, A. L., Curley, B. C., Johnston, R. L., Jiang, J., Yuan, J. (2008). Three-dimensional atomic-scale structure of size-selected gold nanoclusters. 451, doi:10.1038/nature06470.

Limodin, N., Rethore, J., Buffiere, J.Y., Hild, F., Ludwig, W., Rannou, J., Roux, S. (2011). 3-D X-ray microtomgraphy volume correlation to study fatigue crack growth. *Advanced Engineering Materials*, 13, n^{o}3, 186-193.

Lin, C.L., Miller, J.D., (2001). *A new cone beam X-ray microtomography facility for 3D analysis of multiphase materials*. Proceedings of 2nd World Congress on Industrial Process Tomography, Hannover, Germany, Aug. 29-31.

Ludwig, W, Buffière, J-Y, Savelli, S, Cloetens, P. (2003). Study of the interaction of a short fatigue crack with grain boundaries in a cast Al alloy using X-ray micro-tomography. *Acta Material*, 51(3),585–598.

Maatman, R.W., Prater, C.D. (1957). Adsorption and exclusion in impregnation of porous catalytic supports. *Industrial and Engineering Chemistry*, 49, 253–257.

Maire, E., Elmoutaouakkil, A., Fazekas, A., Salvo, L. (2003). In situ measurements of deformation and failure of metallic foams using X-ray tomography. *MRS Bull*, 28, 284.

Marrow, T.J., Buffière, J.-Y., Withers, P.J., Johnson, G., Engelberg D. (2004). High-resolution X-ray tomography of short fatigue crack nucleation in austempered ductile cast iron, *International Journal of Fatigue*, 26, 717-725.

McCullough, E., (1975). Photon attenuation in computed tomography. *Medical Physics*, 2:6, 307-320.

Mees, F., Swennen, R., Van geet, M., Jacobs, P. (2003). Applications of X-ray Computed Tomography in the Geosciences. *Geological Society*, London, Special Publications, 215, 1-6.

Mercier, F., Puiggali, J.-R, Roques, M., Brunard, N., Kolenda, F., (1998). *Convective and microwave drying of alumina beads: Modelling shrinkage.* 3rd world congress on particle technology, 6-9 july 1998, Brighton, UK.

Miguélez-Morán, A.M., Wu, C., Dong, H., Seville, J.P.K., (2009). Characterisation of density distributions in roller-compacted ribbons using micro-indentation and X-ray micro-computed tomography. *European Journal of Pharmaceuticals and Biopharmaceutics*, doi:10.1016/j.ejpb.2008.12.005.

Mul, G., Moulijn, J.A. (2005). *Supported metals in catalyst*, Vol 5, Imperial college Press.

Moreno-Atanasio, R., Williams, R. A., Jia, X. (2010). Combining X-ray microtomography with computer simulation for analysis of granular and porous materials. *Particuology*, 8, 2, 81–99.

Morita, T., Yamahara, H., (2006). Three-dimensional imaging and analysis of granules by high resolution X-ray computed microtomography at the third-generation synchrotron radiation facility. *Pharm. Tech. Japan*, 22, 2533–2539

Mousavi, R., Miri, T., Cox, P.W., Fryer, P.J. (2005). A novel technique for ice-crystal visualisation in frozen solids using X-ray micro-computed tomography. *Journal of Food Science*, 70:5, 437-442

Müller, B., Beckmann, F., Huser, M., Maspero, F., Székely, G., Ruffieux, K., Thurner, P., Wintermantel, E., (2002). Non-destructive three-dimensional evaluation of a polymer sponge by micro-tomography using synchrotron radiation. *Biomolecular Engineering,* 19, 73-78.

Neimark, A.V., Kheifez, L.I., Fenelonov, V.B. (1981). Theory of preparation of supported catalysts. Industrial and Engineering Chemistry. *Product Research and Development*, 20, 439.

Novák, V., Štěpánek, F., Kočí, P., Marek, M., Kubíček, M. (2010). Evaluation of local pore sizes and transport properties in porous catalysts. *Chemical Engineering Science*, 65, 7, 2352-2360.

O Castillo-Villa, P., Baro, J., Planes, A., Salje, K H, Sellappan, P., Kriven, W.M., Vives, E. (2013). Crackling noise during failure of alumina under compression: the effect of porosity. *Journal of Physics*, 25.

Page, J.F (1987). *Applied heterogeneous catalysis*, 515 pages.

Papageorgiou, P., Price, D. M., Gavriilidis, A., Varma, A. (1996). Preparation of Pt/γ-Al_2O_3 pellets with internal step distribution of catalyst: Experiments and theory. *Journal of Catalysis*, 158, 439–451.

Peng, Z., Sheppard, T. (2004). Study of surface cracking during extrusion of aluminium alloy AA 2014. *Materials science and technology*, 20, 1179-1191.

Perego, C., Villa, P. (1997). Catalyst preparation methods. *Catalysis today*, 34, 281-305.

Pierret, A., Capowiez, Y., Belzunces, L., Moran, C.J. (2002). 3D reconstruction and quantification of macropores using X-ray computed tomography and image analysis. *Geoderma*, 106, 247-271.

Pinto, J.F. (1993). Formulation and tableting of controlled release pellets produced by extrusion–spheronization. *Ph.D. Thesis*, University of London, UK.

Phillips, D.H., Lannutti, J.J. (1997). Measuring physical density with X-ray computed tomography. *NDT & E International*, 30, 6, 339-350.

Potter, A.R., Austin, J.C., Ormerod, R.M., Haycock, P.W., Heywood, B.R., George, S.D. (2003). X-ray images of defect formation in porcelain ceramics during drying. *NDT & E International*, 36, 2, 77-83.

Portsmouth, R.L, Gladden, L.F (1991). Determination of pore connectivity by mercury porosimetry. *Chemical Engineering Science*. 46, 12, 3023–3036

Pourcel, F., Jomaa,, W., Puiggal,i J.-R., Rouleau, L., (2007). Criterion for cracks initiation during drying: Alumina porous ceramic strength improvement. *Powder technology*, 172, 120-127.

Radon, J., (1917). Über die Bestimmung von Funktionen durch ihre Integralwerte längs gewisser Mannigfaltigkeiten. *Berichte Sachsische Akademie der Wissenschaften Leipzig*, 69, 262-277.

Ramlau, R., Ring, W. (2007). A Mumford-Shah level-set approach for the inversion and segmentation of X-ray tomography data. *Journal Computer Physic*, 221:539–57.

Ravichandran, K.S., Larsen, J.M., (1997). Effect of crack aspect ratio on the behaviour of small surface cracks in fatigue: Part II Experiments on a titanium (Ti-8Al) alloy. *Metallurgy and materials transaction,* 28A, 157-169.

Reimschussel, A.M., Fredericks, R.J. (1969). Application of Scanning Electron Microscopy to the study of the morphology of multicomponent catalyst system. *Journal of material science*, 4, 885-889.

Richardson, J.T., (1989). Principles of catalyst development, *Fundamental and applied catalysis*.

Rigby, S.P., Daut, S., (2002). A statistical model for the heterogeneous structure of porous catalyst pellets. *Advances in Colloid and Interface Science*, 98, 2, 87-119.

Rigby, S.P., Barwick, D., Fletcher, R.S., Riley, S.N., (2003a). Interpreting mercury porosimetry data for catalyst supports using semi-empirical alternatives to the Washburn equation. *Applied Catalysis A: General*, 238, 303-318.

Rigby, S.P., Fletcher, R.S. (2004). Interfacing Mercury Porosimetry with Nitrogen Sorption. *Particle & Particle Systems Characterization*. 21, 2, 138–148.

Rigby, S.P., Watt-Smith, M.J., Chigada, P., Chudek, J.A., Fletcher, R.S., Wood, J., Bakalis, S., Miri, T., (2006). Studies of the entrapment of non-wetting fluid within nanoporous media using a synergistic combination of MRI and micro-computed X-ray tomography. *Chemical Engineering Science,* 61, 7579-7592

Rigby, S.P., Chigada, P.I., Evbuomvan, I.O., Chudek, J.A., Miri, T., Wood, J., Bakalis, S., (2008). Experimental and modelling studies of the kinetics of mercury retraction from highly confined geometries during porosimetry in the transport and the quasi-equilibrium regimes. *Chemical Engineering Science,* 63, 5771-5788.

Rigby, S.P., Chigada, P.I., Wang, J., Wilkinson, S.K., Bateman, H., Al-Duri, B., Wood, J., Bakalis, S., Miri, T. (2011). Improving the interpretation of mercury porosimetry data using computerised X-ray tomography and mean-field DFT, *Chemical Engineering Science*, 66, 11, 2328-2339.

Rigby, S.P., Tariq, F., Haswell, R., Lee, P.D., McComb, D.W. (2011). Characterization of hierarchical pore structures in ceramics using multiscale tomography, *Acta Materialia*, vol. 59, pp. 2109-2120.

Ruffino, L., Mann, R., Oldman, R., Stitt, E.H, Boller, E.,Cloeten, P., Dimichiel, M., Merino, J. (2005). Using the X-Ray Microtomography for characterisation of catalyst particle pore structure. *The Canadian Journal of Chemical Engineering*. Volume 83, 1, 132-139.

Sadana, A., Katzer, J.R. (1974) Catalytic oxidation of phenol in aqueous solution over copper oxide. *Ind. Eng. Chem. Fundam*. 13, 127-134.

Salvo, L, Cloetens, P, Maire, E, Zabler, S, Blandin, JJ, Buffière, JY (2003). X-ray micro-tomography an attractive characterisation technique in materials science. *Nuclear Instruments and Methods in Physics Research Section B*. 200:273–286.

Satterfield, C.N. (1970), Mass transfert in heterogeneous catalysis, *MIT Press*, Boston.

Sezgin, M, Sankur, B (2004). Survey over image thresholding techniques and quantitative performance evaluation. *J Electron Imaging*, 13:146–68.

Shyr, Y., Ernst, W. (1980). Preparation of nonuniformly active catalysts. *Journal of Catalysis*, 63, 425–432.

Sing, K.S.W., Everett, D.H., Haul, R.&W., Moscou, L., Pierotti, R.A., Rouquerol, J., Siemieniewska, T.(1985). Reporting physisorption data for gas/solid systems with special reference to the determination of surface area and porosity, *Pure Application Chemical*, 57, 603.

Sinka, I.C., Burch, S.F., Tweed, J.H., Cunningham, J.C., (2004). Measurement of density variations in tablets using X-ray computed tomography. *International Journal of Pharmaceutics,* 271, 215-224

Sukop, M. C., Huang, H., Lin, C. L., Deo, M. D., Oh, K., &Miller, J. D. (2008). Distribution of multiphase fluids in porous media: Comparison between Lattice Boltzmann modelling and micro-X-ray tomography. *Physical Review E*, 77, 026710.

Shokri, N., Muhammad, S. (2012). Structure of drying fronts in three-dimensional porous media. *Physical Review E*, vol. 85, Issue 6, id. 066312.

Skyscan Co., (2003). T view: Visualisation, alteration, cut, *measurements user manual. Aartselaar*, Belgium: Skyscan Co.. Available from www.skyscan.be. Accessed Feb. 2009.

Spieker, W.A., Regalbuto, J.R. (2001). A fundamental model of platinum impregnation onto alumina. *Chemical Engineering Science*, 56, p. 3491.

Soustruznik, G., Carl, K., Paula, K. (1968). Alumina-based catalyst and method of preparing same. *Patent, US 3361682 A*.

Subero-Couroyer, C., Ghadiri, M., Brunard, N., Kolenda, F., (2005). Analysis of catalyst particle strength by impact testing: The effect of manufacturing process parameters on the particle strength. *Powder Technology,* 160, 67-80.

Tahir S.M., Ariffin, A.K., (2006). Fracture in metal powder compaction. *International Journal of Solids and Structures*, 43, 1528-1542.

Tariq, F., Haswell,, R., Lee,, P.D., McComb D.W., (2011a). Characterisation of hierarchical pore structures in ceramics using multiscale tomography. *Acta Materiala* 59, 2109-2120.

Tariq, F., Lee P.D., Haswell R., McComb,, D.W., (2011b). The influence of nanoscale microstructural variations on the pellet scale flow properties of hierarchical porous catalytic

structures using multiscale 3D imaging. *Chemical Engineering Science*, Vol. 66, Issue 23, 5804-5812.

Taud, H., Martinez-Angeles, R., Parrot, J.F., Hernandez-Escobedo L. (2005). Porosity estimation method by X-ray computed tomography. *Journal of Petroleum Science and Engineering,* 47, 3–4, 209–217.

Thomson, W. (1871). On the equilibrium of vapour at a curved surface of liquid. *Phil. Mag*. 42, 448-452.

Toda, H., Sinclair, I., Buffière, J.-Y., Maire, E., Khor, K.H., Gregson, P., Kobayashi, T. (2004); A 3D measurement procedure for internal local crack driving forces via synchrotron X-ray microtomography. *Acta Materialia*, 52, 5, 1305-1317.

Toyosada, M., Gotoh, K., Niwa, T. (2004). Fatigue life assessment for welded structures without initial defects: an algorithm for predicting fatigue crack growth from a sound site. *International Journal of Fatigue*, 26, 993-1002.

Trimm, D.L., Stanislaus, A., (1986). The control of pore size in alumina catalyst support: a review. *Applied catalysis*, 21, 215-238.

Uemura, Y., Hatate, Y., Ikari, A. (1987). Formation of nickel concentration profile in Nickel/Alumina catalyst during post-impregnation drying. *Journal of Chemical Engineering* Japan, 20, 117–123.

Vachier, C, Meyer, F (2005). The viscous watershed transform. *Journal Math Imaging Vis,* 22:251–67.

Van Den Berg, G. H., Rijnten, H. Th. (1979). The impregnation and drying step in catalyst manufacturing. *Preparation of catalysts II: Proceedings of the second international symposium on the scientific bases for the preparation of heterogeneous catalysts*. 265–277.

Van Geet, M., Swennen, R., Wevers, M. (2000). Quantitative analysis of reservoir rocks by microfocus X-ray computerised tomography. *Sediment. Geol*., 132,25–36.

Videla, A, Lin, C, Miller, J (2007). 3D characterization of individual multiphase particles in packed particle beds by X-ray microtomography (XMT). *Int Miner Proc,* 84:321–6.

Walendziewski, J., Trawczynski, J. (1994). Influence of the forming method on the pore structure of alumina supports, *Applied catalysis: general*. 119, 45-58.

Wang, G., Yu, H., De Man, B. (2008). An outlook on x-ray CT research and development. *American Association of Physicist in Medicine*. 35 (3), 1051-1064.

Washburn, E.W., (1921). The dynamics of capillary flow. *Physical Review,* 17, 273-283.

Webb, P.A., Orr, C. (1997). Analytical methods in fine particle technology. *Micromeritics Instrument Corp.*, Norcross, GA, USA, 301.

Weyland, M. (2002). Electron tomography of catalysts. *Top Catal.*, 21, 175–183.

Wu, C.Y., Ruddy, O.M., Bentham, A.C., Hancock, B.C., Best, S.M., Elliott, J.A. (2005) Modelling the mechanical behaviour of pharmaceutical powders during compaction, *Powder Technol.* 152 (1–3) 107–117.

Wu, C.Y., Hancock, B.C., Mills, A., Bentham, A.C., Best, S.M., Elliott, J.A., (2008). Numerical and experimental investigation of capping mechanisms during pharmaceutical tablet compaction, *Powder Technol*. 181 (2) 121–129.

Zečević, J., de Jong, K., de Jongh, P.E. (2013). Progress in electron tomography to assess the 3D nanostructure of catalysts. *Current Opinion in Solid State and Materials Science*. 17, 3, 115–125.

Zhang, H., Toda, H., Qu, P.C., Sakaguchi, Y., Kobayashi, M., Uesugi, K., Suzuki, Y. (2009). Three-dimensional fatigue crack growth behavior in an aluminum alloy investigated with in situ high-resolution synchrotron X-ray microtomography. *Acta Materialia*, 57, 11, 3287-3300.

Zhao, X.S., Bao, X.Y., Guo, W., Lee, F.Y. (2006). Immobilising catalysts on porous materials. *Materials today,* 9, n^{o}3, 32-39.

APPENDIX

Matlab Codes

Determination of intensity variation along a line at 4 different angles (0; π/10; π/5 and π/3).

A) Calculation centroid of the catalyst support

Compute the centroid of each cross sections, and superimpose its location on the image. View the results using imtool and imgca.

```
I = imread('v700_10g_0396_without filter.bmp');
figure, imshow(I)
bw = im2bw(I, graythresh(getimage));
figure, imshow(bw)
bw2 = imfill(bw,'holes');
L = bwlabel(bw2);
s  = regionprops(L,'centroid');
centroids = cat(1, s.Centroid);
imtool(I)
hold(imgca,'on')
plot(imgca,centroids(:,1), centroids(:,2), 'r*')
hold(imgca,'off')
```

B) Creation of function in order to determine the intensity variation along a line for several angles.

```
function [r, vals]=gradient(theta)


% input
point = [492 547];              pixel location (centroid)
I = imread('v700_10g_0396_without filter.bmp');     sample grayscale image
np=1024; number of pixels (image size= 1024x1024)
dxpix= 4.02e-6;  pixel size


%% calculations


L=dxpix*np;
dxlin= L/150;
r=0:dxlin:L/2;
vals=ones(length(r),1);
for k=1:length(r)
   % line equation : y = tan(theta) * (x-a) + b
   [x y]=pol2cart(theta,r);
   x=x+point(1)*dxpix;
   y=y+point(2)*dxpix;


   i=ceil(x(k)/dxpix);
   if (i==0); i=1 ;end;
   j=ceil(y(k)/dxpix);
   vals(k)=I(i,j);
```

```
figure(1), plot(i, j, 'Color', clr(i,:))    % plot line
figure(2), plot(vals, 'Color', clr(i,:))    % plot profile
end
r=r';

data=ones(76,1);
for theta=0:pi/10:pi/3
   [r,vals]=gradient(0);  % Theta=0
   data=cat(2,data,vals);
end
data(:,1)=[];
mn=mean(data,2);
sdev=std(data,1); %Standard deviaton
```